The development of low generation cyclic-cored metallodendrimers for potential application in anti-cancer therapy

By

Jaques Buys

Thesis presented in partial fulfilment of the requirements for the degree

Master of Science in Chemistry at the University of Stellenbosch

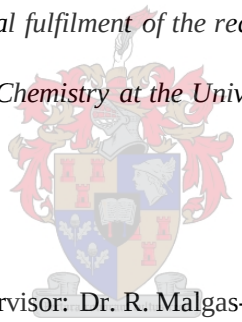

Supervisor: Dr. R. Malgas-Enus

Co-supervisor: Prof. S. F. Mapolie

Faculty of Science

Department of Chemistry and Polymer Science

December 2017

DECLARATION

By submitting this thesis/dissertation electronically, I declare that the entirety of the work contained therein is my own, original work, that I am the sole author thereof (save to the extent explicitly otherwise stated), that reproduction and publication thereof by Stellenbosch University will not infringe any third party rights and that I have not previously in its entirety or in part submitted it for obtaining any qualification.

_____

Jaques Buys

December 2017

ACKNOWLEDGEMENTS

To my supervisor, Dr. Rehana Malgas-Enus. Thank you for keeping up with me until the end. I imagine there were times that you meticulously planned my demise, but instead continued to patiently guide me with valuable suggestions that made this project what it is today. Dr. M, as one of your first students, I applaud the manner in which you handled me. You know how many times you had to convince me to look for the light in the obscurities. Thank you!

To my co-supervisor, Prof. Mapolie, thank you for guidance throughout my studies.

Writing this thesis would literally not have been possible to if it was not for my friends and fellow students. Elaine and Josh, how many times did you listen to me complain? How many smokes did we share? How many nights did we stay up? Thanks for being awesome friends.

To the RME-Nano research group, Jez, Tsepiso and Gerbrandt, thank you for making the office a safe zone. Whatever happened in there stayed in there.

A big thanks to all the students from the inorganic building that either helped, assisted or fix my experimental endeavors. Thanks to Dr. Jaco Brand and Elsa Malherbe for their assistance with NMR spectroscopy as well as the Central Analytical Facility for their services.

A special thanks to the staff and technical assistants of the Inorganic Building for their assistance and motivation during the course of my studies.

The financial assistance from NECSA towards this research is hereby acknowledged.

Lastly, I would like to thank my family for your patience, support, encouragement, Uber services and money.

ABSTRACT

The high mortality rate of cancer worldwide was the impetus for this research project. Our aim was to synthesize suitable radiopharmaceuticals that could potentially act as anti-cancer imaging agents. This entails the synthesis of novel cyclic-cored dendrimers as well as their functionalization at the peripheries, in order to promote selective interaction with hydroxyapatite (HAp), which is a common target for bone cancer imaging agents. These dendritic ligands should also be able to act as a scaffold for "cold" radiopharmaceutical analogues.

Dendrimers exhibit different physicochemical behavior based on their constituents, thus 1,4,8,11-tetraazacyclotetradecane (cyclam) and 1,4,7-triazacyclononane (TACN) were chosen as core molecules to alter the overall topology of the macromolecule. Several attempts describing the synthesis of cyclam-cored poly(amidoamine) (PAMAM) dendrimers, TACN-cored PAMAM dendrimers as well as cyclam-cored polypropylenimine (PPI) and cyclam-cored benzyl amine (BA) dendrimers is reported. During the PAMAM dendrimer (**D1** - **D6**) synthesis some complications during the amidation step prohibited us from acquiring higher generation dendrimers, thus the alternative PPI and BA branched dendrimers (**D7** - **D10**) were chosen in order to compare the effect of the various dendrimers employed. The latter goes via a nitrile intermediate followed by reduction to afford primary amine terminated dendrimers, but complete nitrile reduction eluded us.

Generation 1 cyclam-cored PAMAM dendrimers (**D2**) was identified as a viable candidate to functionalize with either phosphonic acid or salicylaldimine chelators. The phosphonic acid analogue (**L1**) was obtained via an Irani-Moedritzer reaction and using similar reaction conditions a set of model ligands based on propyl amine (**ML1** - **ML2**) and commercial diaminobutane (DAB) PPI dendrimer (**L2**) was synthesized for comparison with the multinuclear derivative. The ligands were usually hygroscopic in nature and under the employed reaction conditions the internal amide of PAMAM showed some evidence of hydrolysis. Two gallium (III) complexes (**C1** and **MC1**) was isolated from **L1** and **ML1**. Alternatively, the analogous salicylaldimine ligand (**L3**) was synthesized via a Schiff base condensation reaction. The relative simplistic ligand was used to isolate two gallium (III) complexes (**C4a** and **C4b**) as well as a copper (II) complex

(**C5**). These compounds were characterized by a range of analytical techniques (FT IR, UV Vis and NMR spectroscopy, mass spectrometry and elemental analysis).

The salicylaldimine analogue (**L3**) as well as the gallium (**C4a** and **C4b**) and copper (**C5**) derivatives were subjected to preliminary DNA binding studies via UV vis spectroscopy titration experiments. **L3** and **C4b** exhibited hyperchromism suggestive of groove binding interaction with DNA. On the other hand, **C5** displayed a hypochromic effect implying intercalation as the mode of binding with DNA. Surprisingly **C4a** showed varying hyper- and hypochromic effect insinuating various binding modes contribute as it interacts with DNA. The DNA binding studies preliminarily indicate that these compounds interact with the DNA structure, meaning it has good potential as anti-cancer agents.

OPSOMMING

Die hoë sterftesyfer van kanker wêreldwyd, was die dryfkrag agter hierdie navorsingsprojek. Ons doel was om geskikte radiofarmaseutiese molekules te sintetiseer wat moontlik as anti-kanker beeldings-agente kan optree. Dit behels die sintese van nuwe sikliese-kern dendrimere asook die funksionalisering van hul oppervlak groepe om selektiewe interaksie met hidroksieapatiet (HAp) te bevorder, wat 'n algemene teiken vir beeldings-agente vir beenkanker is. Hierdie dendritiese ligande moet ook as 'n steier vir "koue" radiofarmaseutiese analoë kan funksioneer.

Dendrimere vertoon verskillende fisiese en chemiese gedrag gebaseer op hul bestandele, dus was 1,4,8,11-tetrasasiklotetradekaan (siklam) en 1,4,7-triazasiklononaan (TACN) gekies as kernmolekules om die algehele topologie van die makromolekule te verander. Verskeie sintetiese pogings wat die gebruik van siklam-kern poliamidoamien (PAMAM) dendrimere, TACN-kern PAMAM-dendrimere asook siklam-kern polipropyleenimien (PPI) en siklam-kern bensielamien (BA) dendrimere, word aangemeld. Tydens die syntese van die PAMAM dendrimere (**D1** - **D6**) het sommige komplikasies tydens die amidasiestap ons verbied om hoër generasie dendrimere te isoleer, dus is die alternatiewe PPI- en BA-vertakte dendrimerers (**D7** - **D10**) gekies om die verskillende dendrimere te vergelyk. Laasgenoemde gaan via 'n nitriel intermediêr, gevolg deur reduksie wat dendrimere met primêre amien groepe op die periferie bied, maar volledige nitril reduksie het ons ontwyk.

Generasie 1 siklam-kern PAMAM-dendrimere (**D2**) is as 'n geldige kandidaat geïdentifiseer om te funksionaliseer met fosfonsuur of salisielaldimien. Die fosfonsuur analoog (**L1**) is verkry via 'n Irani-Moedritzer reaksie. Deur soortgelyke reaksietoestande toe te pas, was 'n stel model ligande gebaseer op propielamien (**ML1**-**ML2**) en kommersiële diaminobutaan (DAB) PPI-dendrimer (**L2**) gesintetiseer vir vergelyking met **L1**. Die ligande was gewoonlik higroskopies van aard en onder die reaksietoestande het die interne amied van PAMAM bewyse van hidrolise getoon. Twee galium (III) komplekse (**C1** en **MC1**) is van **L1** en **ML1** geïsoleer. Die salisielaldimien-analoog (**L3**) was gesintetiseer via 'n Schiff-basis kondensasie reaksie. Die ligand was gebruik om twee galium (III) komplekse (**C4a** en **C4b**), sowel as 'n

koper (II) kompleks (**C5**) te isoleer. Die bogenoemde molekules was gekaraktiseer deur 'n verskeidenheid analitiese tegnieke (FT IR, UV Vis en NMR spektroskopie, massaspektrometrie en elementêre analiese).

Die salisielaldimien analoog (**L3**) sowel as die galium (**C4a** en **C4b**) en koper (**C5**) afgeleides was onderworpe aan voorlopige DNA bindings studies via UV/Vis spektroskopie titrasie eksperimente. **L3** en **C4b** het hiperchromie vertoon wat dui op groef bindende interaksie met DNA. Aan die ander kant het **C5** 'n hipochromiese effek vertoon wat interkalasie impliseer as die manier van bind met DNA. Verbasend genoeg toon **C4a** wisselende hiper- en hipochromiese effekte, wat insinueer dat daar verskillende bindingswyses bydra tot die interaksie met DNA. Die DNA bindende studies dui voorlopig aan dat hierdie molekules met DNA bind, en dat dit goeie potensiaal as anti-kanker agente het.

The development of low generation cyclic-cored metallodendrimers for potential application in anti-cancer therapy.

DECLARATION	**i**
ACKNOWLEDGEMENS	**ii**
ABSTRACT	**iii**
OPSOMMING	**v**
TABLE OF CONTENTS	**vii**
LIST OF FIGURES	**xi**
LIST OF SCHEMES	**xiv**
LIST OF TABLES	**xv**
LIST OF ABBREVIATIONS	**xvi**

TABLE OF CONTENTS

CHAPTER 1: Dendrimers as targeted Radiopharmaceuticals for Cancer Diagnosis

1.1	Introduction	1
1.1.1	Targeted Cancer Treatment	3
1.1.1.1	Bone Structure	3
1.1.1.2	Tumor Growth and Microenvironment	4
1.1.1.3	General Targeting Strategies	6
1.1.2	Targeted Radiopharmaceuticals	9
1.1.2.1	Properties of Common Radionuclides	10
1.1.2.2	Importance of the Chelating Molecule	15
1.1.2.3	Special focus on dendritic Biomolecules	19
1.1.2.4	Influence of the Linker Molecule	24
1.1.3	Project rational and Objectives	26
1.1.4	References	28

CHAPTER 2: Synthesis and Characterization of Cyclic cored PAMAM, PPI and BA Dendritic Ligands

2.1	Introduction	36
2.1.1	Conventional Approaches to Dendrimer Synthesis	37
2.1.1.1	Divergent Synthesis	38
2.1.1.2	Convergent Synthesis	39
2.1.2	Macrocycles as dendrimer cores	40
2.2	Results and Discussion	42
2.2.1	Synthesis of Cyclam and TACN cored PAMAM dendrimers	43
2.2.2	Synthesis of Cyclic cored PPI & BA dendrimers	55
2.3	Conclusion	60
2.4	Experimental Section	61
2.4.1	Synthesis of G0.5 cyclam-cored PAMAM dendrimer (**D1**)	61
2.4.2	Synthesis of G1 cyclam-cored PAMAM dendrimer (**D2**)	62
2.4.3	Synthesis of G1.5 cyclam-cored PAMAM dendrimer (**D3**)	62
2.4.4	Synthesis of G2 cyclam-cored PAMAM dendrimer (**D4**)	63
2.4.5	Synthesis of trimethyl 3,3',3''-(1,4,7-triazonane-1,4,7-triyl)tripropanoate (**D5**)	63
2.4.6	Synthesis of 3,3',3''-(1,4,7-triazonane-1,4,7-triyl)tris(N-(2-aminoethyl) propanamide) (**D6**)	64

2.4.7	Synthesis of 3,3',3",3"'-(1,4,8,11-tetraazacyclotetradecane-1,4,8,11-tetrayl) tetrapropanenitrile (**D7**)	64
2.4.8	Attempted Synthesis of 3,3',3",3"'-(1,4,8,11-tetraazacyclotetradecane-1,4,8,11-tetrayl)tetrakis(propan-1-amine) (**D8**)	65
2.4.9	Synthesis of 4,4',4",4"'-((1,4,8,11-tetraazacyclotetradecane-1,4,8,11-tetrayl)tetrakis (methylene))tetrabenzonitrile (**D9**)	65
2.4.10	Attempted Synthesis of (((1,4,8,11-tetraazacyclotetradecane-1,4,8,11-tetrayl)tetrakis (methylene))tetrakis(benzene-4,1-diyl))tetramethanamine (**D10**)	66
2.5	References	67
CHAPTER 3:	**Synthesis and Characterization of Dendritic Cu (II) and Ga (III) complexes**	
3.1	Introduction	69
3.2	α–Aminophosphoryl compounds	70
3.3	Typical synthetic routes to α–Aminophosphoryl compounds	71
3.3.1	Michaelis – Arbuzov Rearrangement	71
3.3.2	Michaelis–Becker reaction	72
3.3.3	Kabachnik-Fields reaction	72
3.3.4	Irani-Moedritzer reaction	73
3.4	Results and discussion	74
3.4.1	Synthesis and characterization of phosphonic acid modified Cyclam cored PAMAM (**L1**) and the subsequent multinuclear Ga (III) complex (**C1**)	75
3.4.2	Synthesis and characterization of phosphonic acid model ligands and complexes	81
3.4.2.1	Synthesis and characterization of model ligand 2 (**ML2**)	81
3.4.2.2	Synthesis and characterization of model ligand 1 (**ML1**) and model complex 1 (**MC1**)	84
3.4.3	Synthesis and characterization of DAB-PPI ligand (**L2**)	86
3.4.4	Synthesis of salicylaldimine modified Cyclam core PAMAM dendrimers	88
3.4.4.1	Infrared Spectroscopy and UV-Vis	90
3.4.4.2	Nuclear Magnetic Resonance	92
3.4.4.3	ESI-MS and EA	92
3.5	Conclusion	95
3.6	Experimental Section	96
3.6.1	Synthesis of phosphonic acid modified cyclam-cored PAMAM (**L1**)	96
3.6.2	Synthesis of Gallium (III) phosphonic acid modified cyclam-cored PAMAM (**C1**)	97

3.6.3	Synthesis of Model Ligand 2 (**ML2**)	97
3.6.3.1	Synthesis of dimethyl 3,3'-(propylazanediyl)dipropanoate (**ML2a**)	97
3.6.3.2	Synthesis of 3,3'-(propylazanediyl)bis(N-(2-aminoethyl)propanamide) (**ML2b**)	98
3.6.3.3	Synthesis of **ML2**	98
3.6.4	Synthesis of ((propylazanediyl)bis(methylene))diphosphonic acid (**ML1**)	99
3.6.5	Synthesis of gallium ((propylazanediyl)bis(methylene))bis(hydrogen phosphonate) chloride (**MC1**)	99
3.6.6	Synthesis of **L2**	100
3.6.7	Synthesis of **L3**	100
3.6.8	Synthesis of **C4a**	101
3.6.9	Synthesis of **C4b**	101
3.6.10	Synthesis of **C5**	101
3.7	References	103
CHAPTER 4: DNA Binding studies		
4.1	Introduction	106
4.2	DNA Structure	106
4.3	Mode of DNA binding	106
4.3.1	Covalent Binding	107
4.3.2	Non-Covalent Binding	109
4.3.2.1	Intercalation	109
4.3.2.2	Groove binding	112
4.3.2.3	Electrostatic binding	113
4.4	Results and Discussion	114
4.4.1	DNA binding studies	114
4.4.1.1	Electronic absorption titration	115
4.5	Conclusion	120
4.6	Experimental Section	122
4.7	References	123
CHAPTER 5: Conclusions and Future work		
5.1	References	130

LIST OF FIGURES

CHAPTER 1

Figure 1.1: Angiogenesis: Formation of new blood vessels with sufficient nutrients to sustain the rapid tumor growth 5

Figure 1.2: General tumor microenvironment 6

Figure 1.3: Targeting strategies 7

Figure 1.4: Four building blocks of TDDS 10

Figure 1.5: Terbium-cm09 complexes: black - folic acid as targeting agent; blue - albumin-binding entity to prolong blood circulation time; red - terbium radioisotope stably coordinated by a DOTA chelator 13

Figure 1.6: Macrocyclic N_3O_3 chelators (NOTAMBP and NO2APBP) 15

Figure 1.7: (a) aminophosphonic acid (b) amino carboxylic acid 15

Figure 1.8: Structures of four dipicolinic acid (dpa) ligands 17

Figure 1.9: Phosphorhydrazone dendrimer having azabisphosphonic acid (ABP) salt terminal groups 17

Figure 1.10: General structure of Schiff base (R = amino moiety, R' = Carbonyl moiety) 18

Figure 1.11: (A) 4-chloro-2–((4-oxo-4H-chromen-3yl) methylene amino) benzoic acid and its corresponding Cu(II) complex (B) N_2O_2 Schiff base ligand, N,N-bis (2-ethoxysalicylidene)-1,2-diaminopropane and curcumin Ga(III) complex 19

Figure 1.12: Common nanoparticles used for Targeted Drug Delivery System 20

Figure 1.13: Dendrimer Topography 21

Figure 1.14: The effect that dendrimer generation has on physical properties and how it influences the biomedical potential 22

Figure 1.15: G6 PAMAM dendrimer configuration upon decreasing pH (left to right) 23

Figure 1.16: Photo-switchable azobenzene modified PPI dendrimers hosting eosin 24

Figure 1.17: Cationic, Anionic, Neutral and Cleavable linker molecules 25

Figure 1.18: Trimeric TRAP-bisphosphonate conjugates TRAP$(MDP)_3$ and TRAP$(PDP)_3$ 26

CHAPTER 2

Figure 2.1: General summary of all dendritic target compounds 36

Figure 2.2: Graphical representation of divergent and convergent synthesis 37

Figure 2.3: Possible side reactions during PAMAM synthesis: (a) ester hydrolysis leading to a dead branch (b) retro-Micheal addition leading to a missing branch (c) intramolecular cyclization, (d) intermolecular cyclization 38

Figure 2.4: Convergent approach; showing possible restriction of "core coupling reaction" due to bulky dendrons 39

Figure 2.5:	The Chelate effect	41
Figure 2.6:	Possible inter/ intramolecular crosslinking during **D2** synthesis	45
Figure 2.7:	Top spectra: ^{1}H NMR of **D1**; bottom spectra: ^{1}H NMR of **D2**	46
Figure 2.8:	ESI-MS spectra of **D2**	46
Figure 2.9:	Possible fragmentation pattern of **D2**	47
Figure 2.10:	FT-IR spectra of **D1 - D4**	51
Figure 2.11:	Top: ^{1}H NMR of isolated precipitate; Bottom: ^{13}C NMR of isolated precipitate	49
Figure 2.12:	Amidation reaction of **D4** showing possible side products formed	52
Figure 2.13:	FT-IR spectra of **D7** – **D10**	59
CHAPTER 3		
Figure 3.1:	General structure of target Ligands	69
Figure 3.2:	α–Amino phosphonic acids	70
Figure 3.3:	(2) Phosphoric acid (3) Phosphonic acid (4) Phosphonates	71
Figure 3.4:	Michaelis – Arbuzov Rearrangement	72
Figure 3.5:	Michaelis–Becker reaction (10 & 11: R_2/R_3 = alkyl, 12: Phosphinates: R_2/R_3 = alkyl derivative; Phosphonates: R_2/R_3 = alkoxy derivative)	72
Figure 3.6:	Kabachnik-Fields Reaction	73
Figure 3.7:	Irani-Moedritzer reaction	74
Figure 3.8:	(a) bis(phosphonomethyl)amino-terminated poly(ethylene glycol), (b) bis(phosphonic acid)amino-terminated polymers	74
Figure 3.9:	Water-soluble polymer functionalized with methylene phosphonate groups (PEI-MP)	75
Figure 3.10:	FT-IR of Dendrimer (**D2** – Blue), Phosphonic acid derivative (**L1** – Red), Gallium complex (**C1** – Green)	80
Figure 3.11:	Positive mode ESI MS fragment of C1	80
Figure 3.12:	FT-IR of **ML2a** – Blue; **ML2b** – Red; **ML2** – Purple	82
Figure 3.13:	Possible hydrolysis products	83
Figure 3.14:	NMR spectra of **ML1**: Top - ^{1}H NMR; Middle - ^{13}C NMR; Bottom - ^{31}P NMR	85
Figure 3.15:	FT-IR of (a) **L3**; (b) **C4a**; (c) **C4b**; (d) **C5**	90
Figure 3.16:	UV-Vis of **L3** and **C4a**, **C4b** and **C5**	91
Figure 3.17:	Numbering corresponding to **D2** and **L3**	92
Figure 3.18:	ESI MS of **C4b**	93
Figure 3.19:	Plausible fragmentation pathway for **C4b**	94
Figure 3.20:	ESI MS of **C5**	94

CHAPTER 4

Figure 4.1:	General Structural features of DNA	107
Figure 4.2:	Common covalent anticancer drugs (All IC_{50} values in µM): (1) cisplatin, (2) Carboplatin, (3) Oxaliplatin, (4 - 6) N,N,O-tridentate platinum complexes and (7) G0-PAMAM– py4–[$CuCl_2$]	108
Figure 4.3:	Mixed Cu(II) 2,6-bis(benzimidazol-2-yl) pyridine complexes (9, 10) (a) UV-Vis spectroscopy titration experiments (b) Fluorescence spectroscopy titration experiments (c) Fluorescence spectroscopy competitive titration experiments	111
Figure 4.4:	Threading intercalation: Circular dichroism of [Cu(Cur)(DIP)]Cl_2 (11) indicating intercalation as the predominant mode of binding	111
Figure 4.5:	Circular Dichroism: Cu(Cur)(H_2O)Cl (12) and [$Cu(Cur)_2$] (13)	112
Figure 4.6:	macrocyclic tetraaza diacetyl curcumin Cu(II) complex (14)	113
Figure 4.7:	Dizinc(II) complexes 1–3, derived from 1,2-bis(1H-benzimidazol-2-yl)ethane-1,2-diol	114
Figure 4.8:	Non-covalent DNA binding modes. From left to right; intercalation, groove binding and electrostatic binding	115
Figure 4.9:	UV-Vis titrations of **L3** interacting with increasing concentration SS-DNA	117
Figure 4.10:	UV-Vis titrations of **C4b** interacting with increasing concentration SS-DNA	118
Figure 4.11:	UV-Vis titrations of **C5** interacting with increasing concentration SS-DNA	118
Figure 4.12:	UV-Vis titrations of **C4a** interacting with increasing concentration SS-DNA	119
Figure 4.13:	UV-Vis titrations of **C4a** interacting with increasing concentration SS-DNA	120

CHAPTER 5

Figure 1:	Suggested convergent approach – Dendron growth followed by click chemistry to incorporate cyclic core	128
Figure 2:	Acid- & Base catalysed hydrolysis of phosphonate esters	129

LIST OF SCHEMES

CHAPTER 2

Reaction Scheme 2.1:	Microwave-assisted synthesis of **D1**	43
Reaction Scheme 2.2:	Conventional synthesis of **D2**	44
Reaction Scheme 2.3:	Conventional synthesis of **D3**	48
Reaction Scheme 2.4:	Attempted Synthesis of **D4**	49
Reaction Scheme 2.5:	Microwave-assisted synthesis of **D5**	53
Reaction Scheme 2.6:	Attempted synthesis of **D6**	53
Reaction Scheme 2.7:	Microwave-assisted synthesis of **D7**	56
Reaction Scheme 2.8:	Attempted synthesis of **D8**	57
Reaction Scheme 2.9:	Synthesis of **D9**	58
Reaction Scheme 2.10:	Attempted synthesis of **D10**	58

CHAPTER 3

Reaction Scheme 3.1:	Synthesis of **L1**	76
Reaction Scheme 3.2:	Synthesis of **C1**	79
Reaction Scheme 3.3:	Synthesis of **ML2**	82
Reaction Scheme 3.4:	Synthesis of **MC1**	84
Reaction Scheme 3.5:	Synthesis of **L2**	86
Reaction Scheme 3.6:	Synthesis of **L3**, **C4a**, **C4b** and **C5**	89

LIST OF TABLES

CHAPTER 1

Table 1.1: Properties of common Radionuclides, EC = electron capture 12

CHAPTER 2

Table 2.1: FT-IR data pertaining to dendrimer synthesis 54

Table 2.2: ^{1}H NMR spectral data of dendrimers **D1**–**D6** 55

Table 2.3: ^{13}C NMR spectral data of dendrimers **D1**–**D6** 55

CHAPTER 3

Table 3.1: FT-IR of Phosphonic acid chelators 87

Table 3.2: FT-IR and UV-Vis of **L3**, **C4a**, **C4b** and **C5** 92

LIST OF ABBREVIATIONS

AFM	atomic force microscopy
ABP	azabisphosphonic acid
A549	non-small cell lung cancer
BA	Benzyl amine
BMUs	Basic multicellular units
BP	Bisphosphonates
Cat K	Cathepsin K
Cur	Curcumin
CD	circular dichroism
CSF-1	Colony-stimulating factor 1
Cyclam	1,4,8,11-tetraazacyclotetradecane
Cyclen	1,4,7,10-tetraazacyclododecane
CT DNA	calf thymus DNA
DAB	Diaminobutane
DOTA	1,4,7,10-tetraazacyclododecane-1,4,7,10-tetraacetic acid
DIP	4,7-diphenyl-1,10-phenanthroline
dpa	dipicolinic acid
EA	elemental analysis
EDA	Ethylenediamine
eosin Y	2’,4’,5’,7’-tetrabromofluorescein dianion
ESI-MS	Electrospray ionization mass spectrometry
EPR	enhanced permeability effect
FT-IR	Fourier-transform infrared
G	Generation
HAp	Hydroxyapatite
HSBA	4-hydrazinosulfonyl benzoic acid
HepG-2	hepatocellular carcinoma
HPLC	high-performance liquid chromatography
HCT-116	colorectal cancer
LET	Linear energy transfer
PAMAM	Poly(amidoamine)
PPI	Polypropylenimine

LIST OF ABBREVIATIONS

PET	Positron emission tomography
PTH	Parathyroid hormone
RANKL	Receptor activator of NF-KB ligand
TACN	1,4,7-Triazacyclononane
MS	mass spectrometry
MCP-1	Monocyte chemoattractant protein-1
MMP	matrix metalloproteinases
MCF-7	breast cancer
mAb	monoclonal antibodies
MS	mass spectrometry
MLCT	metal to ligand charge transfer
NMR	nuclear magnetic resonance
NOTA	1,4,7-triazacyclononane-1,4,7- triacetic acid
NK	natural killer
PEG	poly(ethylene glycol)
SPECT	single positron emission computed tomography
SEC	size exclusion chromatography
TDDS	Targeted drug delivery system
T_m	melting temperature
TLC	thin layer chromatography
TETA	1,4,8,11- tetraazacyclotetradecane-1,4,8,11-tetraacetic acid
UV–Vis	Ultraviolet-Visible
WHO	World Health Organization

1 Dendrimers as targeted Radiopharmaceuticals for Cancer Diagnosis

1.1 Introduction

The earliest written description of cancer dates back to approximately 3000 BC in which the Edwin Smith papyrus describes a case of breast cancer that was incurable. The Ebers papyrus dates back to 1500 BC and contains records of skin, uterus, stomach and rectum cancers.[1] The Greek physician, Hippocrates (460 – 370 BC), discarded the superstitious belief surrounding cancer and postulated that cancer was caused by an imbalance of body secretions (blood, mucus, bile). The growth of cancer reminded Hippocrates of a crab and he used the words 'carcinos' and 'carcinoma' to describe tumors, which refer to crab in Greek. Aulus Celsus (25 BC-AD 50) translated these Greek words to Latin from which the term cancer originated and has been used until the present day. Claudius Galen (130 – 200 AD) proposed that black bile caused incurable cancer, whereas yellow bile was the cause for curable cancer. He used the term 'oncos' to describe tumors, thus the study and specialization of cancer are referred to as oncology.[2] Religious restrictions severely hampered the advancement of medical knowledge and more than 1000 years passed before Galen's theory was rejected. Only once scientists performed autopsies where they able to disprove the existence of black bile. During the 16th century, Paracelsus (1493 – 1541) studied tumors of several mine workers and correlated cancer to chemical exposure of the work environment.[2] He was first to administer chemicals (mercury, lead, sulfur, iron, zinc, copper, arsenic, iodine, and potassium) for the treatment of cancer, however this cost him his life after his challengers beat him to death in Salzburg, Austria.[3] Percival Pott (1714 – 1788) noted the correlation between chimney sweeps and cancer of the scrotum due to chronic exposure to soot.[4] During the 18th century Giovanni Morgagni steered oncology in a more scientific direction by relating patient's illness to pathological findings while performing biopsies. However it was not until the 19th century, with the assistance of the microscope, that Rudolf Virchow (1821 – 1902) propelled the field of oncology to the micro-level by relating microscopic pathology to illness. He claimed that cancer was a disease of cells, while David Hansemann (1790 – 1864) proposed that tumor cells have some abnormal chromatin content.[2] Early 20th century saw Theodore Boveri (1862 – 1915) present his

theory of cancer based on the abnormalities of chromosomes.[5] The work Boveri did is considered the cornerstone of modern molecular approaches to cancer. Shortly after this transition of understanding to a molecular scale, Ellerman and Bang[6] as well as Peyton Rous[7] reported on independent research relating to tumor viruses in chickens. Ellerman and Bang reported on inducing leukemia in healthy chickens in 1908, but it was only until Peyton Rous was able to isolate a section of a sarcoma present in the breast muscles of hens in 1910 that the first RNA tumor virus was discovered. He received a Nobel Prize for his work in 1968. In 1915 Katsusaburo Yamagiwa and Koichi Ichikawa[8] were able to prove that cancer can be induced using coal tar on rabbit skin, a similar effect to what tobacco is responsible for. However it was not until James Watson and Francis Crick discovered the exact structure of DNA, for which they received a Nobel prize in 1962,[9,2] that a shift to molecular level was truly possible. All cellular function is dictated by DNA and once the code was interpreted, modern techniques to answer complex chemical and biological questions became a possibility.

Today cancer is regarded as the leading cause of death worldwide. According to the World Health Organization (WHO), the disease is responsible for 8.2 million deaths and 14.1 million new cases were reported in 2012.[10] This high mortality rate justify the need to further scientific and technological advancement that address the issues concerning cancer. The “magic bullet” concept postulated by Paul Ehrlich in the early 1900’s laid the cornerstone for modern day target-selective research. Targeted drug delivery is based on the selective interaction between a biomolecule and a specific moiety present at the target site. Research has developed to the extent that conventional treatment methods (surgery, chemo- and radiotherapy) in combination with innovative modalities, provide a realistic approach to addressing the challenges faced today. Recent developments address the interdependence between the targeting moiety, the carrier and the drug. Continuing along this thought, this review intends to cover literature pertaining to the use of dendrimer macromolecules as scaffolds for radionuclide used as diagnostic imaging modules for bone cancer.

1.1.1 Targeted Cancer Treatment

Ongoing research devoted to the complex origin and intricate nature of cancer has identified several aspects that aid in selective drug intervention. Conventional chemotherapeutic drugs have shown promise, but their efficacy are governed by pharmacokinetic- (how the body allows the drug molecule to move into, through- and out of the body) and pharmacodynamic (the effect the drug molecule has on the body and how it interacts with tumor cells) profiles. Generally, low drug solubility, unselective accumulation and premature clearance, hamper chemotherapeutics. More recently, the ability that the disease possesses to develop its own offense via various resistance mechanisms,[11] as well as the unique responses illustrated by different patients, has warranted urgent attention. In order to develop a targeted drug delivery system (TDDS), it is important to understand the biological path that the intended system has to pass through to reach its target site.

1.1.1.1 Bone Structure

The bone matrix acts as the supporting structure of our body and consists of 69 % inorganic, of which 99 % is hydroxyapatite (HAp), and 22 % organic components of which 90 % is collagen.[12] The specific shape, size, and structural integrity are constantly regulated via bone modeling and -remodeling processes. Bone modeling is the process involved in forming bone from cartilage. During bone modeling, the formation and resorption of bone occur independently at separate environments and governs the morphology and mass acquired during growth. Bone remodeling can be thought of as the maintenance process during which old bone is continuously removed and replaced by new bone. Bone remodeling maintains the structural quality and regulates the mineral metastasis (calcium and phosphate).[12]

Two important cells that participate in bone remodeling are osteoclasts and osteoblasts. The osteoclasts cells are responsible for breaking down the bone tissue, whereas osteoblasts cell specialize in forming new bone. For bone remodeling, these two types of cells interact and are synchronized to work in unison as basic multicellular units (BMUs). Several proteins have been identified to be involved during the five-step remodeling process that can cause an imbalance between bone forming and bone resorbing. One such

example is the parathyroid hormone (PTH) which maintains calcium homeostasis and induces osteoblast to express monocyte chemo-attractant protein-1 (MCP-1), colony-stimulating factor 1 (CSF-1) and receptor activator of NF-KB ligand (RANKL). These promote osteoclast formation, which during the resorption phase, release HCl and cathepsin K (Cat K) that dissolves the organic matrix. The matrix debris is removed by tissue macrophages, known as osteomacs, residing in periosteum and endosteum. These osteomacs work in tandem with the mesenchymal bone-lining cells that possess the ability to deposit the fibrous protein constituent of bone (collagenous matrix). The coupling signal that initiates the transition from bone resorption to bone formation was initially thought to be stored in the bone matrix itself and other hypotheses were that the osteoclasts store the signals. Although it is unknown how the formation phase is activated, the process involves the recruitment of osteoblast precursors at the Howship lacunae. Once the osteoblast precursors have developed and are in place, they proceed to synthesize bone matrix known as osteoid. They are also responsible for subsequent mineralization by HAp. The process of bone remodeling concludes once the amount of bone formed is equal to that removed. During the final termination phase, the osteoblast can either form part of the bone-lining cells, undergo apoptosis or become embedded in the matrix and differentiate into osteocytes.

Osteoporosis occurs once the bone resorbing process outweighs the bone forming process, thus creating bone with inadequate strength. Other imbalances in bone turnover include osteosarcoma which describes osteoblastic differentiation due to malignant osteoid and bone metastasis. During the bone remodeling process, there are several properties, especially the environment offered by HAp, that can be exploited to improve diagnosis and treatment of bone cancers and overcome drug delivery challenges.[9]

1.1.1.2 Tumor Growth and Microenvironment

The microenvironment surrounding cancerous cells can be best understood when looking at the tumor growth. Generally, the nature of cell growth can be traced back to oncogenes and tumor suppressor cells.[13] The former acts as activators, whereas the latter is concerned with inhibiting specific processes. Normal cells initially proliferate to encourage growth, but eventually, they serve as regulators that replace

old or damaged cells. Tumor cells proliferate uncontrollably in a disordered fashion. The rapid rate at which tumor cells proliferate allows them to displace normal cells and consume most of the available nutrients. Initially, diffusion of nutrients is sufficient to sustain the growth of tumor cells, but only up to a size limit of ± 2 mm.[3] In order to grow past this limit, they need to acquire new blood vessels. They do so through a process known as angiogenesis whereby new blood vessels form from pre-existing vessels (Figure 1.1).

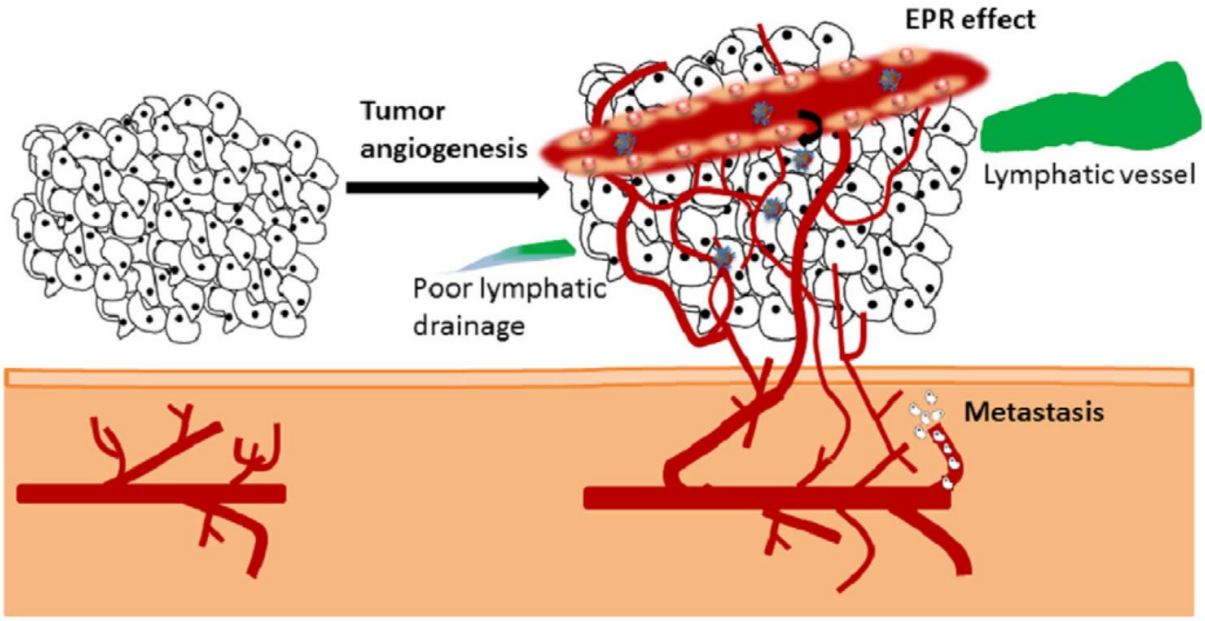

Figure 1.1: Angiogenesis: Formation of new blood vessels with sufficient nutrients to sustain the rapid tumor growth. [14]

The rapid proliferation observed in tumor cells restricts proper vasculature development and is responsible for its disordered and fenestrated nature. The incomplete development of the endothelial (a monolayer that covers vasculature and lymphatic systems) leads to improper basement membranes and leaky endothelium linings with pores ranging from 200 nm-2 µm.[15] The rapid proliferation rate also compromises the development of the lymphatic system which regulates waste in the interstitial space/extracellular space.[16] As a result of the porous aberrant vasculature and lack of circulation, the blood flow and the interstitial fluid pressure fluctuate. Inefficient blood flow promotes the formation of hypoxic and acidic conditions in tumor cells which influence tumor progression, metathesis and the development of multi-drug resistance.[17] Alternative methods to alleviate blood flow restrictions has been investigated.[18]

The disordered/abnormal nature encountered in cancer cells accounts for its non-uniform heterogeneity.[19] The leaky nature increases the interstitial fluid pressure which prohibits convection/diffusion of molecules through the vascular and interstitial spaces.[20]

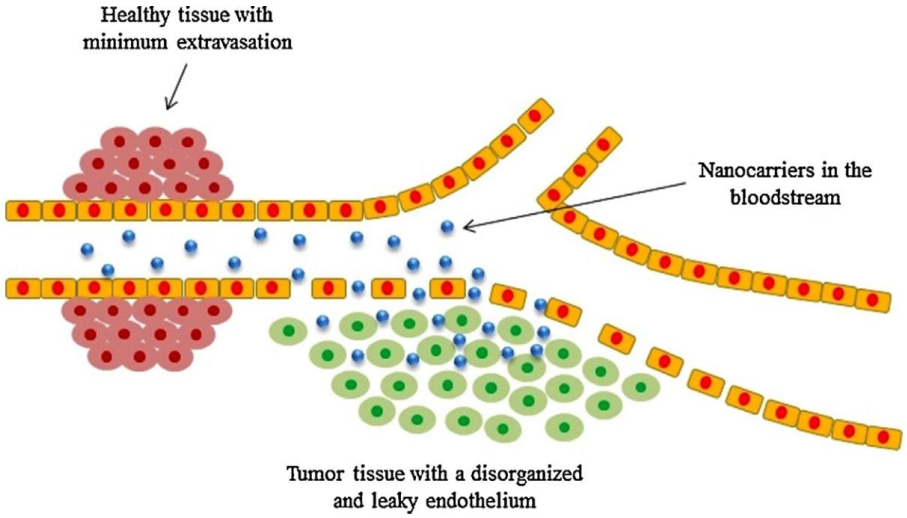

Figure 1.2: General tumor microenvironment. [21]

1.1.1.3 General Targeting Strategies

Several physiological conditions of the microenvironment have been identified as potential targeting strategies. The abnormal vasculature has illustrated different retention profiles based on the phenomenon known as the enhanced permeability effect (EPR).[22] It describes how molecules with discrete physicochemical properties can enter the porous, highly permeable blood vessels available in tumor cells and display extended retention profiles. This enables the selective accumulation of drug molecules, thus addressing the non-specific nature of drug molecules and reducing severe side effects. The idea to alter the pharmacokinetics and biodistribution of a compound by exploiting the pathophysiological characteristics of the tumor vascular is known as *passive targeting*. The strategy does, however, depend on the tumor heterogeneity and the nature of the extracellular matrices, coupled with high interstitial fluid pressure prohibiting diffusion.

Alternatively, the *active targeting* strategy relies on the pharmacodynamics and selectivity of the drug compound. Essentially, the drug is modified to incorporate a modality that ideally shows selective

interaction with overexpressed cancer cells. These drug-conjugates are aimed to improve selective bio-distribution; however if not carefully designed, they can lead to non-specific binding and receptor-mediated endocytosis which can cause an increase in drug toxicity and a decrease in effective drug dosage.[23]

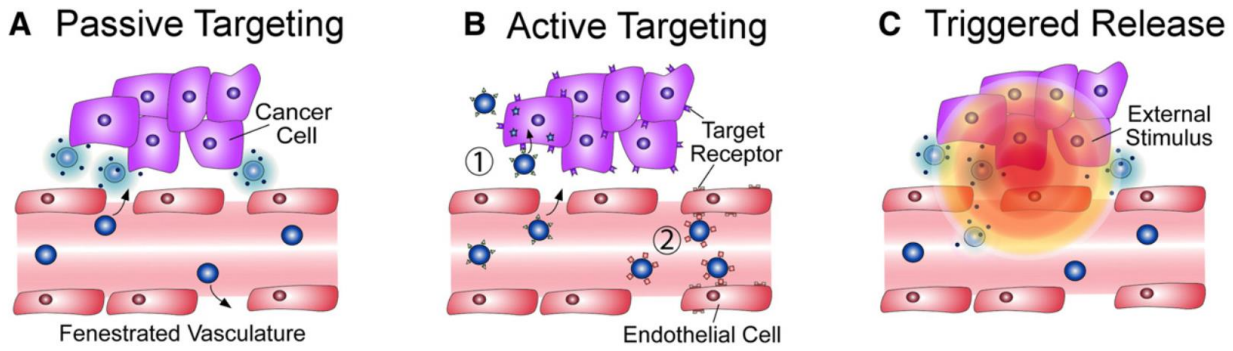

Figure 1.3: Targeting strategies. [24]

Current research tends to combine passive and active targeting strategies and since the late 1970's drug-conjugates capable of responding to subtle stimuli have been investigated.[25] Stimuli-responsive drug delivery goes beyond active and passive targeting, counting on a combination of physical, chemical and/or biological aspects that may ultimately lead to the triggered release of drugs-conjugates. These triggers are categorized as external (temperature, light, ultrasound, magnetic force, electric fields) or internal (pH, redox, enzyme) mediated stimuli.

External stimuli usually rely on some form of physical trigger applied externally. Amongst the most common methods are thermoresponsive systems which rely on a change in temperature to induce some change in the TDDS. Needham *et al.*[26] utilized local hyperthermia (temperature increase) to enhance the permeability of their lipid bilayer to encourage desorption of encapsulated drugs. At elevated temperature the increased vascular permeability allows the desorbed molecule to penetrate deep into the tumor. Light offers a non-invasive, simplistic and biocompatible approach that promises precise control over spatial exposure as a stimuli,[24] but can only be used on regions that can be directly illuminated due to significant light scattering by soft tissue.[27] It is well known that the azobenzene moiety isomerizes in a reversible fashion under irradiation of ultraviolet-visible light,[28] which could aid in the triggered release of

encapsulated drug molecules.[29] Ultrasound destabilizes nanocarriers based on the cavitation phenomenon. Essentially vapor cavities are formed in liquid and once subjected to ultrasound waves disrupts nanocarriers to promote drug release and momentarily increase its permeability. Azagury *et al.*[30] reported on transdermal drug delivery using ultrasound. Magnetic fields and electric fields are alternative external stimuli used to promote controlled drug release. The former can guide paramagnetic nanoparticles to the desired area induce drug release based on a hyperthermic effect and the latter can guide conducting nanoparticles before promoting drug release by electrochemical reduction-oxidation.[27]

Internal stimuli largely rely on the microenvironment surrounding tumor cells and exploit subtle changes to induce drug delivery. The irregular angiogenesis of tumor cells causes a deficit of nutrients and oxygen. This leads to a microenvironment that is slightly more acidic and rich in reducing agents. The difference in pH between healthy cells (~7.4) and the extracellular environment of tumor cells (6.5-7.2) can be utilized as a trigger for drug delivery. The development of nanocarriers that possess ionizable groups or acid sensitive bonds is ideal properties to exploit the acidic microenvironment. Ionizable groups are subject to conformational and solubility changes, whereas acid sensitive bonds can be cleaved to encourage drug delivery.[31] The regulatory glutathione tripeptide responsible for the cellular reductive microenvironment is overexpressed in tumor cells and can be exploited during triggered drug delivery. Wen *et al.*[32] reviews drug carriers with redox sensitive disulfide bond susceptible to cleavage for intracellular drug delivery. Although not as common, enzyme-based stimuli can also be harnessed to improve drug delivery. The design of drug carriers with short peptide sequences as linkers can be cleaved by enzymes such as proteases, phospholipases or glycosidases typically found in the extracellular environment of tumor in order to aid the release of drug molecules.[24]

The complex nature of cancer requires innovative methods to combine targeted delivery with stimuli-responsive systems. However, developing a module that combines the aforementioned targeting strategies is a complex process, especially relating physical and chemical features to specific microenvironment aspects. The term *theranostics* has been used to describe vessels capable of combining diagnostic and

therapeutic strategies which can perform several functions such as multi-stimuli-responsive, multi-targeted delivery and co-delivery of drugs simultaneously in a controlled and targeted manner. Theranostics can monitor the accumulation of nano-medicine compounds at the target site, visualize biodistribution, quantify triggered drug release, and assess therapeutic efficacy. Theranostics strives to shift the frontier of biomedical development to the stage of personalized medicine.

1.1.2 Targeted Radiopharmaceuticals

A carefully designed TDDS can provide protected transport of drugs, enhanced targeting abilities and a manner of control during drug release. The development of nanotherapeutics that increase the bioavailability of hydrophilic drug molecules, bypass biodegrading enzymes, release the cargo at the affected site upon small changes in stimuli and degradation or excretion of the carrier molecule offers immense prospects to improve the efficacy of drug delivery and to limit the side effects of anti-cancer drugs. Given the broad understanding of the tumor microenvironment relating to bone cancer and the knowledge of the possible targeting strategies available, the focus will now shift to the individual components that combine to construct a TDDS, in particular target-specific radiopharmaceutical as radiotherapy has shown promise in cancer diagnosis and therapy.

During the design of a target-specific radiopharmaceutical, it is important to know which isotope to use in line with the intended application (diagnostic or therapeutic). The choice of radioisotope would govern the choice of chelating ligand, usually bifunctional chelators. Ideally, radiopharmaceuticals require a kinetically inert, thermodynamically stable complex to reduce side effects and increase or maintain its efficiency. These ligands are usually coupled to specific biomolecules to alter their solution properties and improve their selectivity. In some cases, a linker molecule in-between the biomolecule and ligand aid in the degradation of the TDDS in order to increase excretion rates (Figure 1.4).

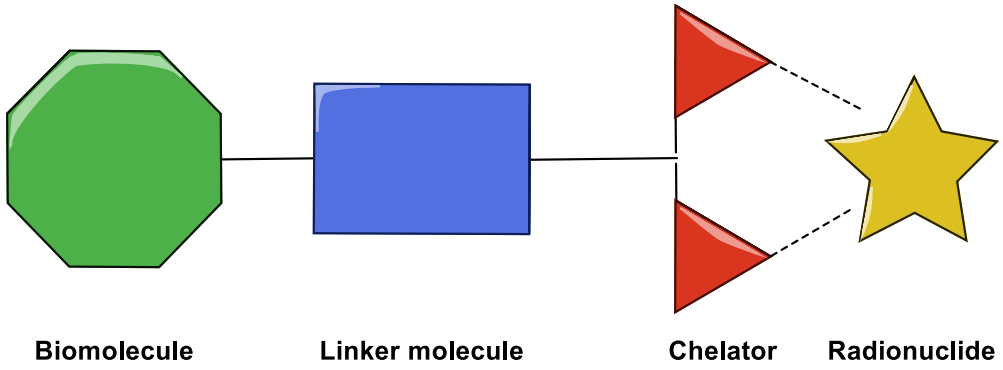

Figure 1.4: Four building blocks of TDDS.

1.1.2.1 Properties of Common Radionuclides

In 1913, George de Harvesy first postulated the "tracer principle", which is the basis of modern day radiopharmaceuticals. The principle essentially entails the use of a radionuclide-conjugate to trace its distribution.[33] Radiotherapy relies on particles which the radioactive isotopes emit as it decays. Radiation therapy can be divided into three categories: external radiation, internal radiation or systemic radiation. External radiation delivers high-energy x-rays; electrons or proton beams from the outside of the body. Internal radiation places radiation sources, temporarily or permanently, within or near the tumor slowly releasing radiation as the source decays. Systemic radiation delivers radionuclide-conjugates known as radiopharmaceuticals through the bloodstream either by ingestion, catheter infusion or intravenous administration.

When considering which isotope to select for the TDDS it is important to know the intended application. For *therapeutic pharmaceuticals* particles that cause ionization through its decay to induce cell death are used. α-, β- and auger-emitting radionuclides emits radiation energy able to destroy or damage DNA directly or indirectly by creating free radicals within the cells that damage the DNA. Linear energy transfer (LET) is the term used to describe the amount of energy an ionizing particle transfers to the material traversed per unit length and is generally expressed in kiloelectronvolts per micrometer (KeV/µm). Typical α-emitters such as Astatine-211 (^{211}At), Bismuth-212 (^{212}Bi), Bismuth-213 (^{213}Bi), Actinium-225 (^{225}Ac), Radium-223 (^{223}Ra), Lead-212 (^{212}Pb), Thorium-227 (^{227}Th), and Terbium-149 (^{149}Tb) eject high energy

with quite short ejection range.[34] Cell death occurs only when α-particles traverse the cell nucleus, thus they are ideal for small tumors. β-emitters such as yttrium-90 (^{90}Y), iodine-131 (^{131}I), lutetium-177 (^{177}Lu), samarium-153 (^{153}Sm), strontium-89 (^{89}Sr), holmium-166 (^{166}Ho), rhenium-186 (^{186}Re), rhenium-188 (^{188}Re), copper-67 (^{67}Cu), promethium-149 (^{149}Pm), gold-199 (^{199}Au) and rhodium-105 (^{105}Rh) have lower LET and longer radiation ranges relative to α-emitters.[34] They can damage or kill cells by indirect damage known as the "crossfire effect". β-emitters can overcome treatment resistance and are mostly used for large tumors. Auger-emitters such as bromine-77 (^{77}Br), indium-111 (^{111}In), iodine-123 (^{123}I), and iodine-125 (^{125}I) are low in energy with short range which arise during the decay of the radioisotope.[35] During the decay, vacancies formed in the inner shell due to electron capture or internal conversion is rapidly filled by electrons undergoing relaxation in from higher energy shells. These transitions emit a characteristic Auger.[36]

For *diagnostic pharmaceuticals*, the radionuclide should be either a gamma- (^{67}Ga, ^{99m}Tc, ^{111}In, ^{177}Lu) or positron (^{68}Ga, ^{64}Cu, ^{44}Sc, ^{86}Y, ^{89}Zr) emitter. The purpose of diagnostic radiopharmaceuticals is to provide an accurate molecular morphological description of the target location, but also provide an ideal opportunity to evaluate several biological functions such as bio-distribution and excretion rates.[37] Diagnostic radiopharmaceuticals utilize radionuclides that decay to release photons with high enough energy to penetrate the body and be detected externally but low enough to be collimated by a camera. Diagnostic radiopharmaceuticals require a radionuclide that decays solely by photon emission as any release of additional particles would administer undesired extra dose to the patient. The most common imaging modality used in diagnostic radiopharmacy to assess the molecular morphology is single positron emission computed tomography (SPECT). This method requires a gamma-emitting isotope. Positron emission tomography (PET) is another common imaging modality that requires positron-emitting isotopes.[33]

Properties such as half-life, type of radiation energy and presence or lack of other particulate radiation emissions determines the suitability of a radionuclide for a specific application. (Table 1.1) below summarizes the properties of some common radionuclide.

Table 1.1: Properties of common Radionuclides, EC = electron capture. [38,39]

Nuclide	$t_{1/2}$ (h)	Decay mode	*E* (keV)	Nuclide	$t_{1/2}$ (h)	Decay mode	*E* (keV)
^{60}Cu	0.4	β^+ (93%) EC (7%)	β^+ 3920, 3000, 2000	^{212}Pb	10.6	β^- (100%)	α 570
^{61}Cu	3.3	β^+ (62%) EC (38%)	β^+ 1220, 1150, 940, 560	^{225}Ac	240	α (100%)	α 5600-5830
^{62}Cu	0.16	β^+ (98%) EC (2%)	β^+ 2910	^{123}I	13.2	γ	γ 159
^{64}Cu	12.7	β^+ (19%) EC (41%) β^- (40%)	β^+ 656	^{131}I	202	γ (81.2%) β	γ 284, 364, 637
^{66}Ga	9.5	β^+ (56%) EC (44%)	β^+ 4150, 935	^{99m}Tc	6.0	γ	γ 140
^{67}Ga	78.2	EC (100%)	γ 93, 184, 300	^{18}F	1.83	Positron	640
^{68}Ga	1.1	β^+ (90%) EC (10%)	β^+ 1880	^{11}C	20.4	Positron	960
^{44}Sc	3.9	β^+ (94%) EC (6%)	γ 1157 β^+ 1474	^{13}N	9.96	Positron	1190
^{47}Sc	80.2	β^- (100%)	γ 159 β^- 441, 600	^{15}O	2.07	Positron	1720
^{111}In	67.2	EC (100%)	γ 245, 172	^{186}Re	89.2	γ β (9.4%)	β 1069
^{177}Lu	159.4	β^- (93%)	γ 122, 208 β^- 177, 385, 498	^{188}Re	17.0	γ β (15.1%)	β 2120
^{86}Y	14.7	β^+ (33%) EC (66%)	β^+ 1221	^{166}Ho	26.9	γ β (6.7%)	β 1853
^{90}Y	64.1	β^- (100%)	β^- 2280	^{89}Sr	52.7 d	B	β 1463
^{89}Zr	78.5	β^+ (23%) EC (77%)	β^+ 897	^{32}P	14.3 d	β	β 1710
^{212}Bi	1.1	α (36%) β^- (64%)	α 6050 β^- 6089	^{221}At	7.2	α	α 5869
^{213}Bi	0.76	α (2.2%) β^- (97.8%)	α 5549 β^- 5869				

The ionization particles ideal for diagnostic and therapeutic purposes usually differ. Thus, the combination of diagnostic and therapeutic radionuclides into a single modality is a relatively new, complex concept. Different radionuclides emitting different ionization usually cause harmful additional radiation. Additionally, different radionuclides react differently with specific chelators which complicate the synthesis of such theranostic molecules.

Müller *et al.* used 4 different isotopes of terbium (^{149}Tb, ^{152}Tb, ^{155}Tb and ^{161}Tb) to form 4 complexes using the same type of ligand, but each for a specific application. ^{152}Tb-cm09 and ^{155}Tb-cm09 are ideal for PET and SPECT diagnosis, respectively. ^{149}Tb-cm09 and ^{161}Tb-cm09 emit α- and β-particles, respectively, which is ideal for therapy. This proof of concept illustrates that it is possible to combine diagnosis and therapy in a single module by using the different isotopes of the same element (Figure 1.5).[40]

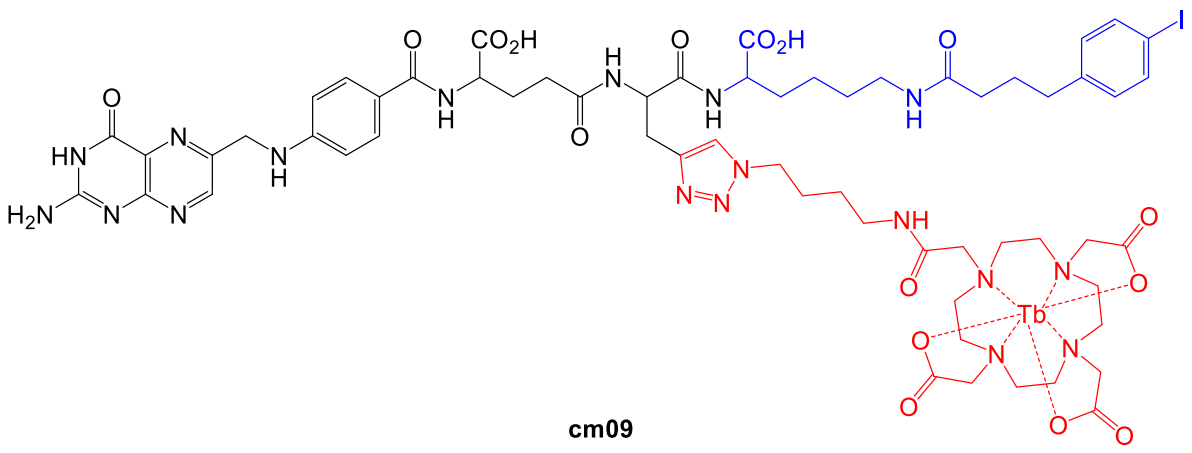

Figure 1.5: Terbium-cm09 complexes: black - folic acid as targeting agent; blue - albumin-binding entity to prolong blood circulation time; red - terbium radioisotope stably coordinated by a DOTA chelator. [40]

Copper has a variety of radioactive isotopes available (^{60}Cu, ^{61}Cu, ^{62}Cu, ^{64}Cu and ^{67}Cu) and display diverse coordination chemistry with soft donor atoms (phosphorous and sulfur). Copper-64 is a unique radioisotope that decays via positron- and β-emission (39 %) useful for diagnostic imaging (PET) and via electron capture decay (43 %) ideal for therapeutic radiopharmacy.[41] The use of macrocyclic ligands for copper labeling generally affords more stable complexes relative to acyclic ligands.[42] Initially, cyclen and cyclam were considered, but it was found that their respective acetic acid analogues 1,4,7,10-

tetraazacyclododecane-1,4,7,10-tetraacetic acid (DOTA) and 1,4,8,11- tetraazacyclotetradecane-1,4,8,11-tetraacetic acid (TETA) showed increased *in-vivo* stability.[43] A further increase in the kinetic stability was achieved by using cross-bridged derivatives of TETA; however, harsh radiolabeling conditions are required for these analogues.[44,45] The use of 1,4,7-triazacyclononane-1,4,7- triacetic acid (NOTA) has recently drawn attention due to its mild radiolabeling conditions and enhanced *in-vivo* stability.[46,47]

One of the most widely used nuclides for imaging is ^{99m}Tc due to its properties and relative ease of preparation. Several examples illustrating the use of stable ^{99m}Tc-phosphonate complexes with high affinity for diseased bones as diagnostic imaging agents for SPECT.[48–51] PET gives higher resolution and sensitivity, thus gallium-68 radioisotope has been probed as an alternative. The most common oxidation state of gallium (III) prefers hard donors such as nitrogen or oxygen donors as a consequence of their high charge density. These metals prefer to form six coordinated complexes due to their small size. These highly charged cations are prone to hydrolysis below pH 4, thus polydentate chelators are necessary for adequate stability during radiolabeling. Amongst the most stable complexes are observed for macrocyclic N_3O_3 donors due to the perfect fit of the metal in the macrocyclic cavity.[52] 1,4,7-triazacyclononane-1,4,7-triacetic acid (NOTA) analogues, ^{68}Ga–NOTAM^{BP} and ^{68}Ga-NO2AP^{BP} were studied by Hermann and co-workers (Figure 1.6). The complexation rates of these ligands were lower than those of NOTA, but almost quantitative labeling was achieved within 10 to 15 minutes. They also observed that during complexation of ^{68}Ga–NOTAM^{BP} the amide group was hydrolytically unstable, thus rendering it unsuitable for radiopharmacy. ^{68}Ga-NO2AP^{BP} have similar pharmacokinetics to that of labeled DOTA-bis(phosphonate) conjugates, commonly used 99mTc-bis(phosphonate) radiopharmaceuticals and [18F]Na; however, it results in a significantly higher accumulation of ^{68}GaNO2AP^{BP} on bone. The superior adsorption kinetics and convenient availability of ^{68}Ga render ^{68}GaNO2AP^{BP} as one of the best leading compounds for the development of bone-targeted PET probes.[53]

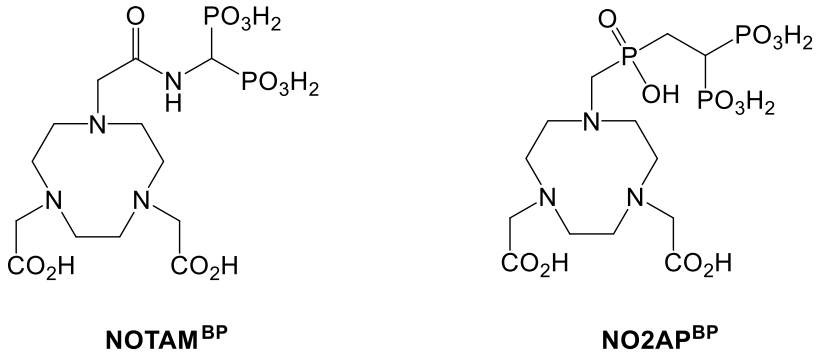

Figure 1.6:Macrocyclic N_3O_3 chelators ($NOTAM^{BP}$ and $NO2AP^{BP}$). [53]

1.1.2.2 Importance of the Chelating Molecule

Incorporating a radionuclide in a TDDS requires a suitable chelator. Ideally the chelator should be able to perform a dual function of binding to the selected radionuclide and have high affinity for the overexpressed target in the tumor. The nature of the complex between the radionuclide and chelator should be kinetically inert and thermodynamically stable under physiological conditions, it should have rapid complexation kinetics and high specificity for the intended radionuclide, it should show high affinity for the intended target and finally the preparation should be simple and cost-effective. However, complexation of a radionuclide has a significant effect on the pharmacokinetics of radiopharmaceuticals.[54]

The use of aminophosphonate chelators are justified by their high affinity for diseased bone and their capability to form stable complexes with an array of metals. Several natural occurring phosphonates have been isolated since the discovery of 2-aminoethanephosphonic acid in 1959 by Horiguchi and Kandatsu.[55] The interest devoted to understanding and exploiting organophosphorus compounds stems from similarities shared with their carboxylic counterpart (Figure 1.7).[56]

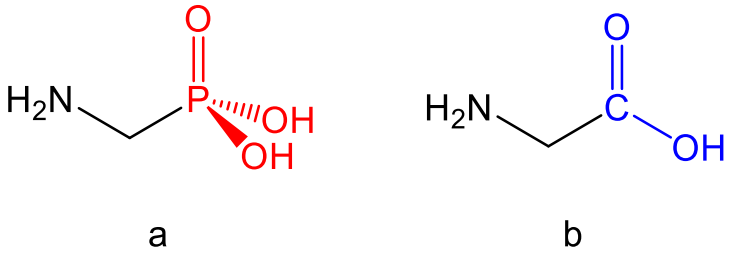

Figure 1.7: (a) aminophosphonic acid (b) amino carboxylic acid

The chelating abilities of phosphonic acids are well known[57] and with the addition of an amine moiety, improved binding abilities have been observed.[58] Several reports can be found in the literature describing the binding interactions that exist between these compounds and alkaline earth-, transition-, and heavy metal ions.[59] These properties have since been exploited in metal extraction[60] and transport,[61] catalysis,[62,63] as well as immobilization of catalysts.[64,65] The ongoing studies regarding the coordination chemistry of organophosphorous compounds have enabled these compounds to act as promising moieties in a variety of fields. These include applications such as corrosion inhibitors[66] and flame retardants[67] or in agriculture as herbicides[68] and pesticides.[69,70] The biological aspects have been proven in their antimicrobial and antifungal properties.[71] However, it was their intriguing medicinal applications that drew our attention. The characteristic N-C-P moiety has shown activity towards several receptors and enzymes as compatible substrates or as enzyme inhibitors,[65,66] antibiotics[74,75] and anticancer agents.[76,77] The rationale for incorporating α–aminophosphonic acid on a dendrimer scaffold is twofold. They are suitable chelators for a range of radionuclides to prevent the nonspecific deposition of the radionuclide in tissues and secondly they exhibit inherent affinity for bone (HAp).

Orvig *et al.* assessed the bone-targeting ability of four dipicolinic acid amine (dpa)-based ligands through solution depletion experiments to determine the influence of the R appendage on bone mineral targeting and binding using HAp as a model for the bone mineral (Figure 1.8). The introduction of the phosphonate moieties (c and d) provided clear evidence that phosphonates possess the ability to bind to HAp with moderate (c) and high (d) strength.[78]

Bisphosphonates (BP) are considered to have the greatest bone-directing capability of any organic moiety to the extent that it becomes incorporated into newly mineralized tissue. This however can cause major side-effects due to its long-term retention within the bone matrix. Mono derivatized phosphonates are considered a viable option for facilitating the inherent bone-targeting ability, without itself impacting bone histology through long-term ligand accumulation.

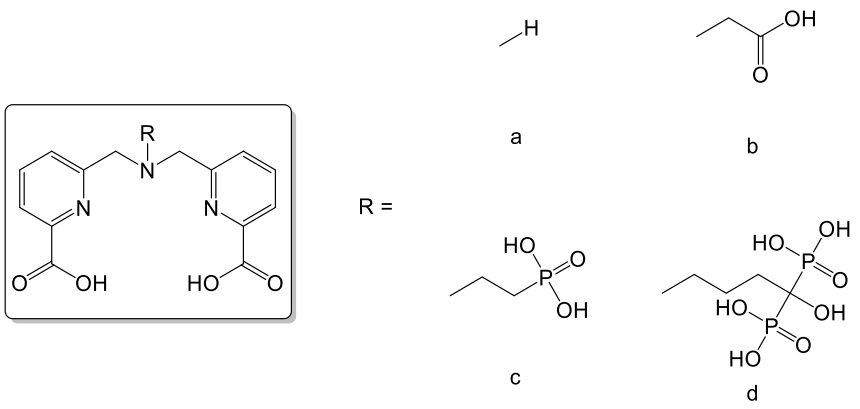

Figure 1.8: Structures of four dipicolinic acid (dpa) ligands. [78]

A phosphorhydrazone dendrimer having azabisphosphonic acid (ABP) salt terminal groups, is known to interact with several biological aspects such as selectively promoting the multiplication of human natural killer (NK) cells.[79] It also interacts with monocytes and induces their activation through an anti-inflammatory pathway. They have been used to treat rheumatoid arthritis by inhibiting the development of inflammatory arthritis preventing cartilage destruction and bone erosion.[80] Their activity can be associated with the symmetrical terminal phosphonic acid salts, the number of terminal functions as well as the type of internal structure.[81]

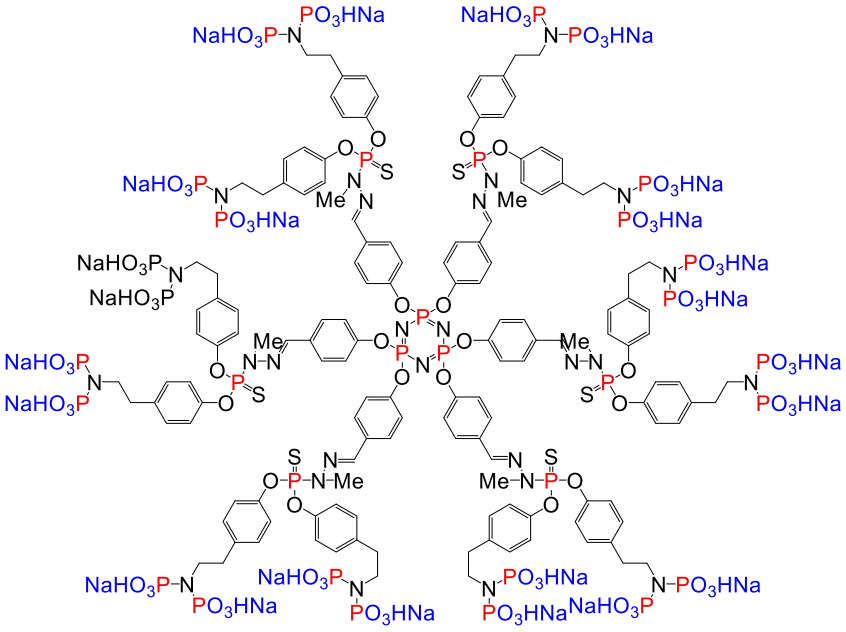

Figure 1.9: Phosphorhydrazone dendrimer having azabisphosphonic acid (ABP) salt terminal groups. [82]

Schiff-base ligands are another interesting set of ligands that has been used in biological applications. The condensation products of primary amines and carbonyl compounds yield an azomethine/imine and was first reported in 1864 by the German chemist Hugo Schiff (Figure 1.10).

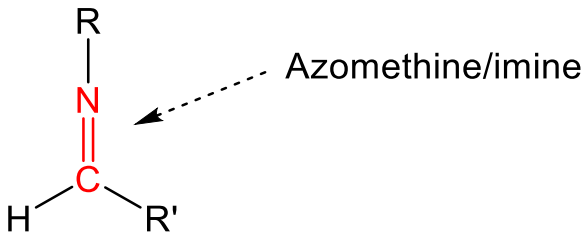

Figure 1.10: General structure of Schiff base (R = amino moiety, R' = Carbonyl moiety).

Otherwise known as Schiff bases, these compounds readily form complexes with most metals and numerous reports of their use in catalysis can be found.[83,84] The diverse complexation and optical properties these ligands exhibit have seen them been used as metal extractants,[85] potentiometric sensors[86], photostabilizers[87] and dyes for solar collectors.[88] Several review articles discussing the biological importance of Schiff bases have regularly appeared in literature. These exemplify the use of Schiff bases in antibacterial,[89] antifungal,[90] antiviral,[91] antimalarial,[92] and antitumor[93] applications. Some representative examples of biological applications of Schiff base complexes are briefly discussed here.

Mendu *et al.* synthesized the Schiff base ligand 4-chloro-2–((4-oxo-4H-chromen-3yl) methylene amino) benzoic acid and its corresponding octahedral metal complexes of the type ML_2 (Figure 1.11A). The complex showed intercalative binding to CT-DNA as determined by UV–Vis and fluorescence spectroscopic titrations as well as viscosity measurements. The nuclease activity of the above metal complexes shows that Cu (II) complex cleave DNA through redox chemistry. The biological activity was evaluated against four bacteria viz. *E.coli*, *B.subtilis*, *pseudomonas* and *Edwardella* and two fungi viz. *penicillium* and *trichoderma*. The complexes were found to be more active than the free ligand.[94] Donnelly *et al.* evaluated a neutral, low molecular weight, lipophilic Ga(III) complex using a tetradentate N_2O_2 Schiff base ligand and the β-diketone curcumin as a bidentate auxilliary ligand to give a six-coordinate complex

(Figure 1.11B). They observed that the complex binds to amyloid-β plaques, which are accociated with Alzheimer's disease and concluded that the complex has potential as a imaging agent for PET.[95]

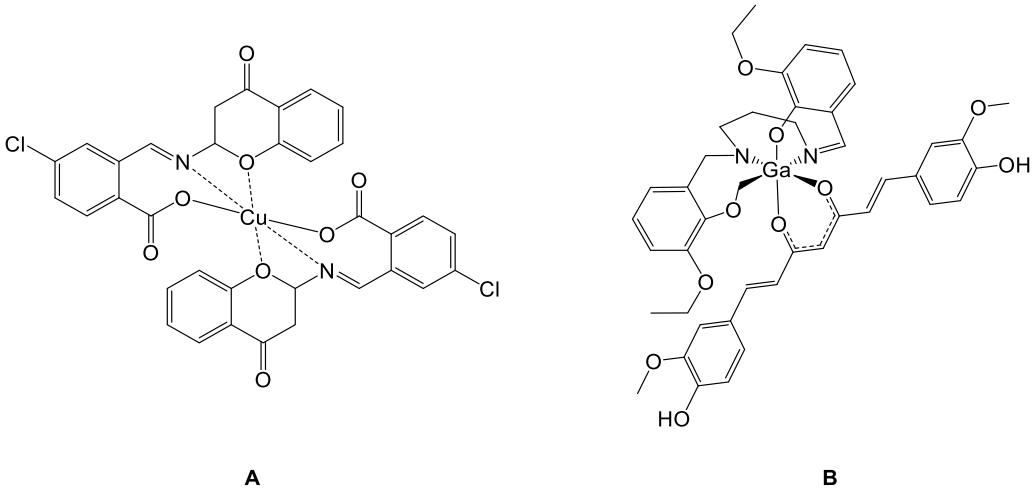

Figure 1.11: (A) 4-chloro-2–((4-oxo-4H-chromen-3yl) methylene amino) benzoic acid and its corresponding Cu(II) complex[94] *(B) N_2O_2 Schiff base ligand, N,N-bis (2-ethoxysalicylidene)-1,2-diaminopropane and curcumin Ga(III) complex.* [95]

1.1.2.3 Special focus on dendritic Biomolecules

There are several types of nanoparticles that possess physicochemical properties that have drawn the attention of researchers. The main physicochemical features of nanocarriers are structure, composition, size, surface properties, porosity, charge, and aggregation behavior. Particle size influences properties such as vascular dynamics, diffusion, adhesion, uptake and clearance mechanisms which play a detrimental role in the efficacy of drug delivery. Similarly, the shape of the particle is known to influence properties such as internalization and selectivity of the particle. Surface characteristics such as charge and hydrophilic or hydrophobic nature influence circulation time and internalization. Figure 1.12 summarizes several nanoparticles used. These include viral nanoparticles, polymer-drug conjugates, metal nanoparticles and polymeric nanoparticles; however, for the purpose of this review, the focus will solely be on dendrimers as biomolecule segments of the nanocarrier vectors.

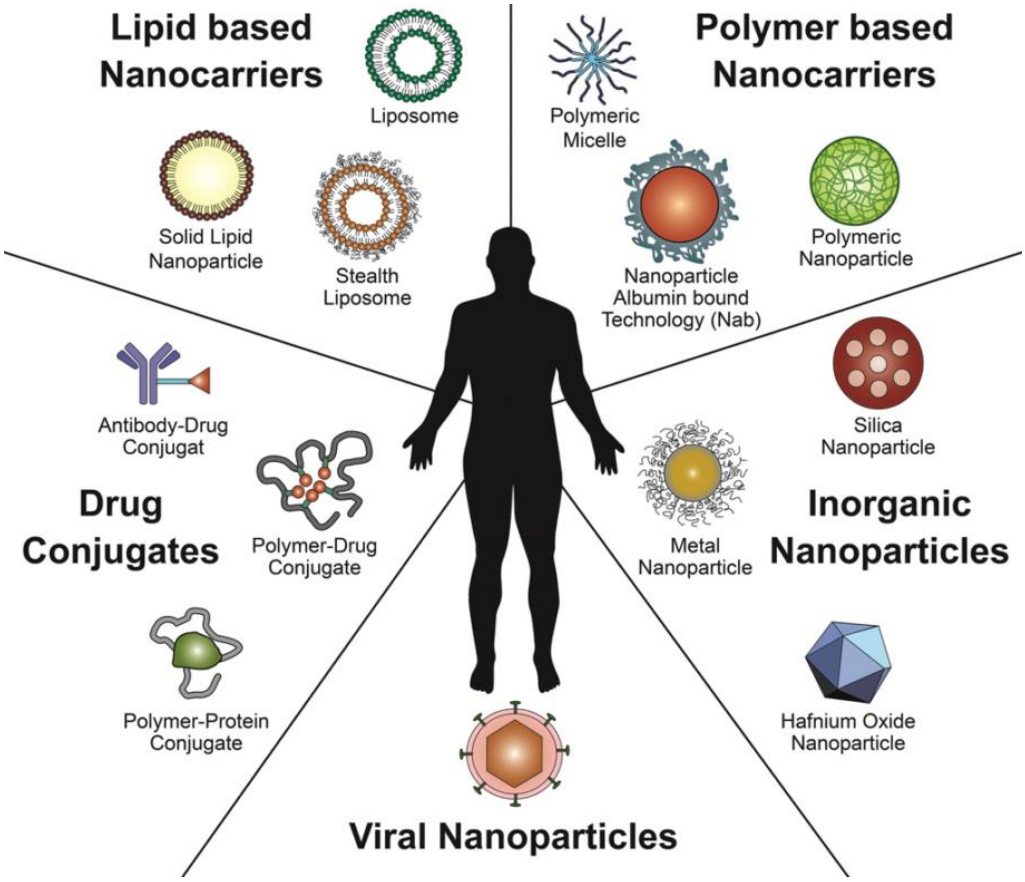

Figure 1.12: Common nanoparticles used for Targeted Drug Delivery System. [24]

Dendrimers currently receive active interest because of their unique chemical and physical properties as well as their wide range of potential applications. Dendrimers are highly branched polymers in the nano-size region with three-dimensional, globular architecture which possess a high number of functional groups on the periphery. The controlled synthesis of dendrimers yields highly reproducible, monodisperse macromolecules that are unparalleled by any linear polymers. From a topological viewpoint dendrimer macromolecules have very specific architecture and contain three distinct domains: (a) The core at the center of the dendrimer, which consists either of a single atom or a molecule having at least two identical functional groups, (b) branches of molecules containing at least one focal point (branching point) and (c) a multivalent surface consisting of a high number of functional groups.[96] The branching points are usually of such a nature that it allows for successive reactions to take place in a successive manner. This allows the

dendrimer molecule to form an ordered series of radially concentric layers if they are all connected to a core molecule. These “layers” are known as generations (G).

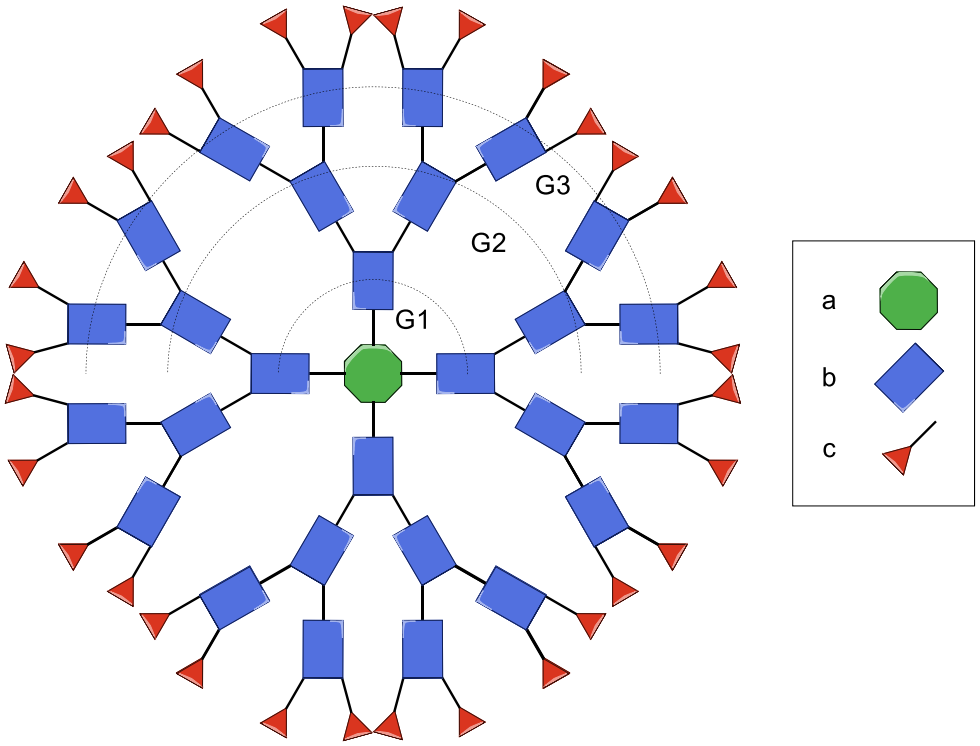

Figure 1.13: Dendrimer Topography.

The stepwise synthesis of dendrimers offers chemists the ideal opportunity to achieve macromolecules of a specific size, which in part influences the shape of the molecule.[97] As the dendrimer generation increases, the functional groups at the periphery increases exponentially and the branches would normally adopt the least sterically hindered conformation. Thus, lower generation dendrimers exhibit linear conformations, whereas higher generation dendrimers adopt a spherical conformation. Further increase of dendrimer generation confines the branches and eventually reaches a point known as “de Gennes dense packing” limit. Dendrimers are typically the same size range of several biological structures and are considered to be biocompatible due to their ability to interact and cross cell membranes as well as their extended circulation time allowing for passive targeting via the EPR effect (Figure 1.14).

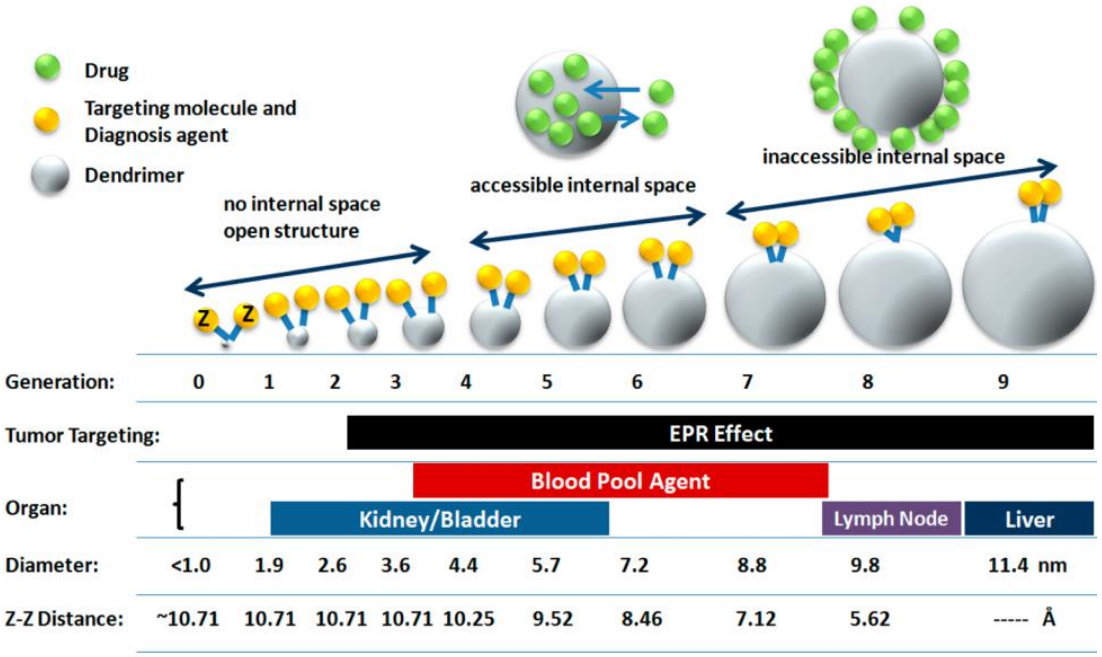

Figure 1.14: The effect that dendrimer generation has on physical properties and how it influences the biomedical potential. [98]

El-Sayed *et al.*[99] investigated the influence of size, molecular weight, molecular geometry and the number of surface amine groups of PAMAM dendrimers (G0 – G4) to comprehend the relationship between these features and their permeability across Caco-2 cell monolayers. They determined that no single variable was responsible, but rather a combination of these parameters had an influence on their permeability and that G0 – G2 were best suited for oral drug delivery.

Previous studies have shown the dendrimer conformation is influenced by several factors. The intramolecular interactions of the multivalent dendrimers are highly dependent on the properties of the bulk solution, i.e. polarity, ionic strength, and pH. Typical PAMAM and PPI dendrimers, possessing amine surface functionalities, adopt extended conformation at low pH due to electrostatic repulsion between protonated tertiary amines which forces the dendritic branches apart. At low pH, the hydrogen bonding between interior protonated tertiary amines and surface primary amines cause the branches to fold back and create a denser interior. Solvent polarity also affects dendrimer conformation. Apolar solvents favor intramolecular interactions; thus back-folding is favored. Polar solvents compete for these intramolecular interactions, thus allowing a more extended conformation (Figure 1.15).[100]

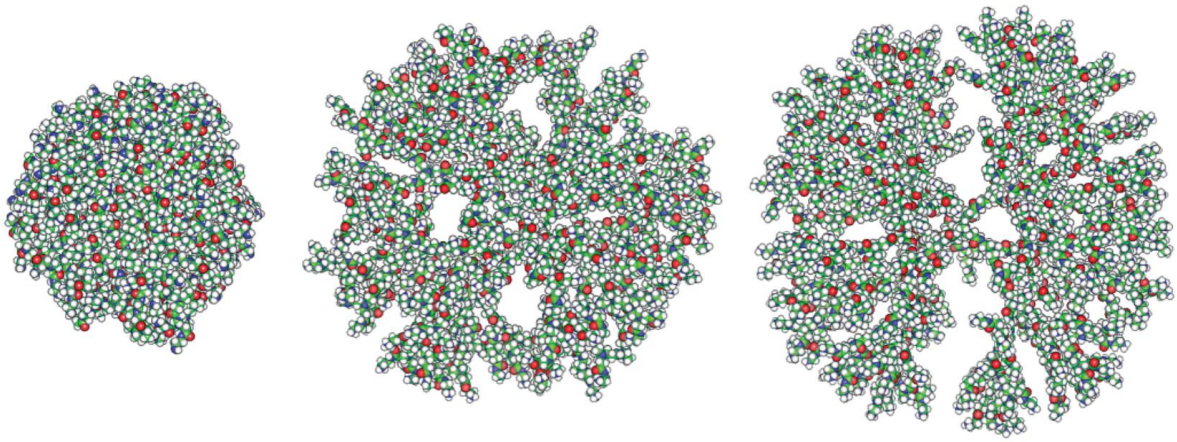

Figure 1.15: G6 PAMAM dendrimer configuration upon decreasing pH (left to right). [101]

The multivalent nature of dendrimers plays a crucial role in the pharmacodynamics and biodistribution profiles. Cationic dendrimers can interact non-specifically with negatively charged cell membranes, which can cause severe side effects. Thus, it is important to modify the cationic periphery and alter their cytotoxicity. Baker *et al.*[102] modified G5 PAMAM dendrimers with folic acid before covalently coupling these acid–targeted dendrimers with methotrexate, radionuclides, and fluorescent dyes. The biodistribution, imaging potential, and antitumor efficacy of these drug delivery systems were evaluated and compared to free drug and non-targeted polymer controls. The targeted polymer-drug conjugate evidently displayed an improved therapeutic index based on a lower toxicity and an increase in drug effectiveness.

Another valuable feature of dendrimers are the voids that exist within higher generation dendrimers. Depending on the size of the repeating subunit, these compartments are able to encapsulate smaller molecules. The multivalent surface of dendrimers aid in shielding the interior from the bulk solution, creating a microenvironment within the dendrimer. This important aspect renders dendrimers ideal for host-guest interaction and encapsulation of guest molecules.[96-103] Vogtle *et al.* demonstrated the host-guest capability of azobenzene modified PPI dendrimers (Figure 1.16). The photochemical and photophysical properties of solutions containing dendrimers and the potential host eosin Y (2',4',5',7'-tetrabromofluorescein dianion) were monitored by fluorescence spectroscopy. The strong fluorescence band of eosin Y decreases in the presence of the dendrimers by a static mechanism which implies the

quenching occurs due to association between the eosin and the dendrimer. The quenching is most likely due to an electron-transfer reaction between the singlet excited state of eosin and the tertiary amine units present along the branches of the dendrimers. [29]

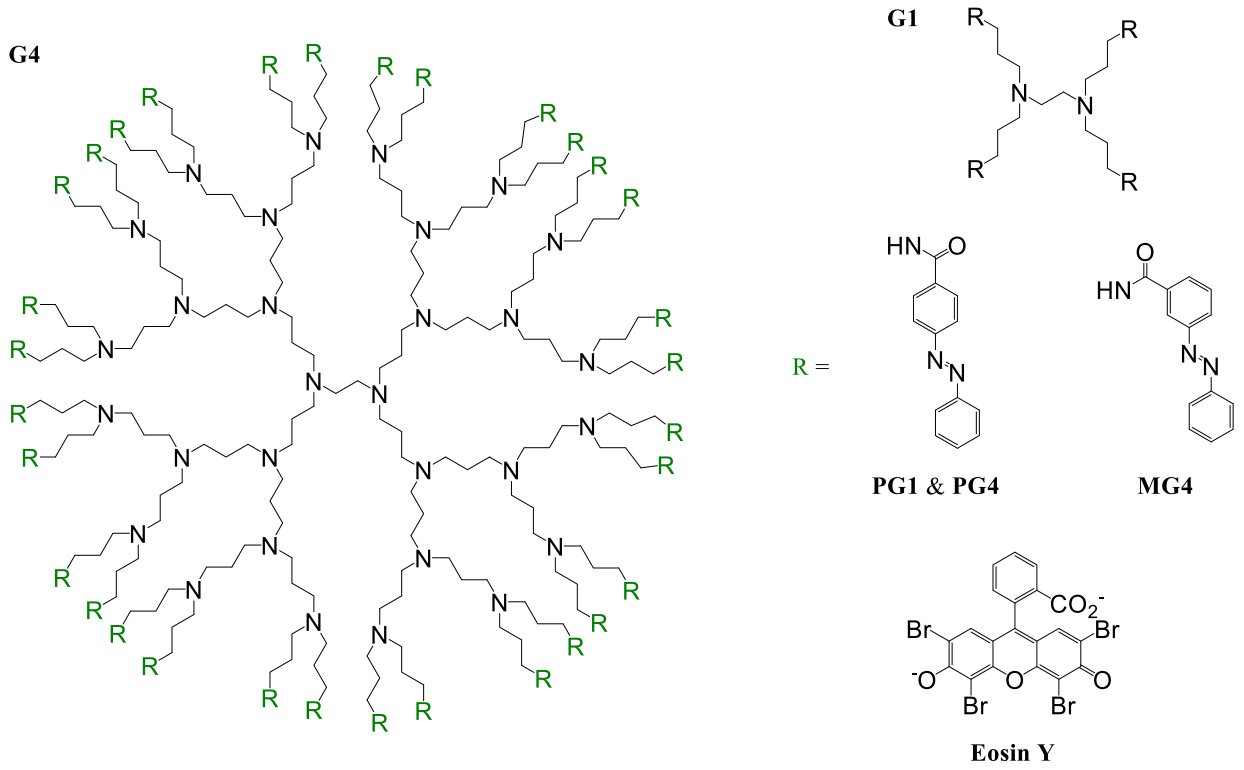

Figure 1.16: Photo-switchable azobenzene modified PPI dendrimers hosting eosin. [29]

1.1.2.4 Influence of the Linker Molecule

The linker molecule connects the drug and biomolecule and its purpose is to alter the pharmacodynamics for improved selectivity and efficacy of radiopharmaceuticals. The linker is responsible for the release profile and excretion kinetics of the drug. Biodegradable linkers offer the opportunity of enzymatic degradation which alter the rate at which the drug is released (high amounts of drug immediately or small amounts over time)[104] and rate of excretion of low molecular weight degradation products (reduce the non-tumor uptake and retention while maintaining a high tumor uptake). Several types of linkers such as cationic, anionic, neutral and metabolically cleavable have been reported before (Figure 1.17).

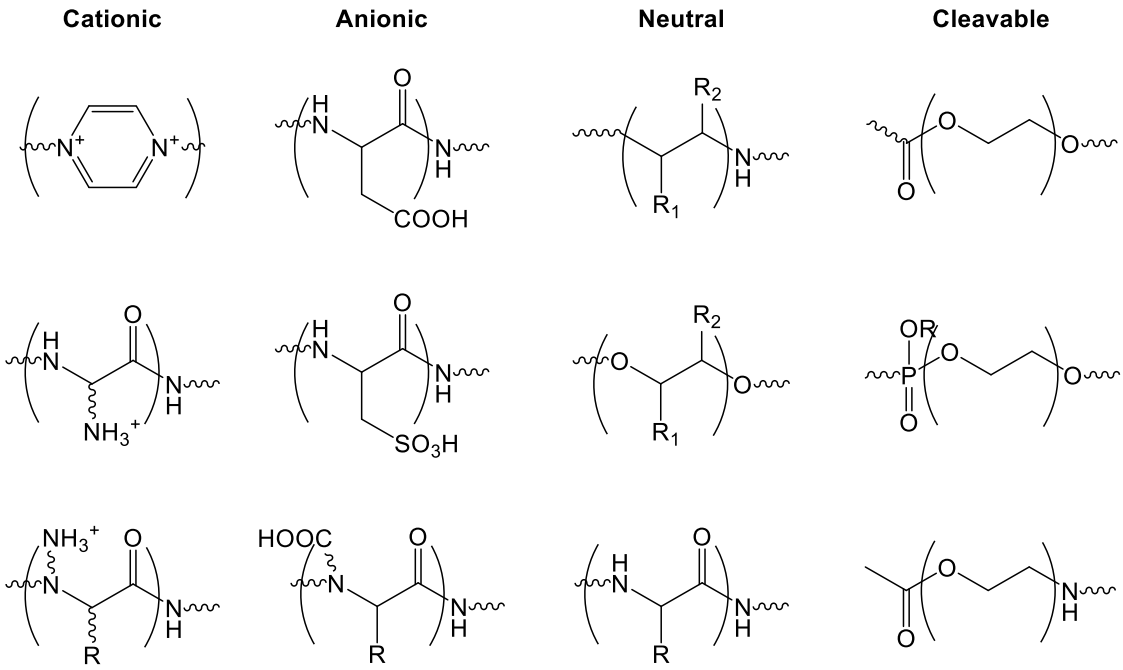

Figure 1.17: Cationic, Anionic, Neutral and Cleavable linker molecules. [52]

Tumors generally exhibit an acidic microenvironment (pH 5.8 – 7.3), thus several pH sensitive linkers have been utilized to achieve selective drug delivery. Amide and hydrozone linkages were used to attach doxorubicin to dendrons and the latter was cleaved at low pH, facilitating drug release.[105] Alternative pH sensitive linkages, Cis-aconityl, were compared to stable succinic linkages and the former exhibited improved drug action.[106] Kaminskas *et al.* evaluated a different pH sensitive linker, 4-hydrazinosulfonyl benzoic acid linker (HSBA), to facilitate release of doxorubicin in the acidic microenvironment of a solid tumour.[107] Bone specific enzymes such as matrix metalloproteinases (MMP) are expressed by osteoclasts and osteoblasts. MMPs degrade collagen, basement membranes and cleave peptide bonds. These enzymes have previously been explored as targets for selective drug release.[108] These linkers are inhibited by tetracycline and derivatives such as doxycycline.[109]

The prospect of using dendrimers as radiopharmaceuticals have received little attention in literature, especially reports of dendritic radiopharmaceuticals that combine all the aspects of a TDDS. Although as early as 1994, Gansow *et al.* reported the use of PAMAM dendrimers coupled with DOTA derivatives as multinuclear scaffolds for ^{90}Y, ^{111}In, ^{212}Bi and Gd (III) metals. They were able to incorporate monoclonal

antibodies (mAb) for tumor-targeted delivery of these nuclides.[110] Another preclinical study conducted by Notni *et al.* evaluated trimeric TRAP-bisphosphonate-conjugates of gallium-68 as potential PET agents. The structure of these conjugates resembles that of dendrimers where the complex forms within the macrocyclic core and is stabilized by the interior phosphonates to form an 'in-cage' complex, leaving the bisphosphonate on the periphery to interact with bone.

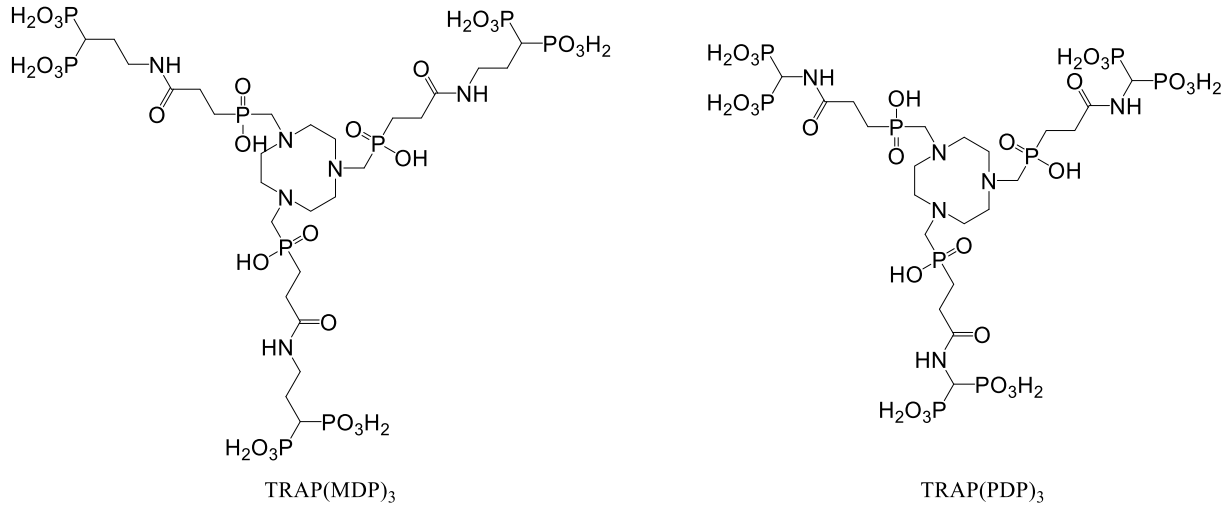

Figure 1.18: Trimeric TRAP-bisphosphonate conjugates TRAP(MDP)$_3$ and TRAP(PDP)$_3$.

More recently, Laznickova *et al.* described coupling a DOTA analogue via a pyridine-N-oxide link to G1 and G4 PAMAM dendrimers. These dendritic conjugates were readily labeled with ^{177}Lu forming complexes which are stable for at least 24 h both in physiological solution and in the presence of 100-fold molar excess of EDTA or DTPA. They concluded that dendrimer radiometal chelate conjugates could serve as a construct to add antibodies in order to obtain markedly high specific activity and minimal loss of their immunoreactivity.[111]

1.1.3 Project rational and Objectives

The aim of this study was to design a targeted drug delivery system (TDDS) that can potentially act as an anti-cancer agent. The size, shape and surface characteristics influence the pharmacodynamics and pharmacokinetic properties of the TDDS. The unique properties of dendrimers (size, shape and multifunctional periphery) advocate its use as a multinuclear scaffold ideal for targeted cancer diagnostic and radiotherapy. With this in mind, generation 1 PAMAM dendrimers based on cyclam (N_4) and TACN (N_3) macrocycles were prepared and characterized for their use as dendritic scaffolds. Their multivalent periphery allows for the incorporation of several chelator molecules able to interact with both radionuclides and target receptors. Thus, these scaffolds were subsequently modified with phosphonic acid as well as salicylaldehyde to yield the respective dendritic ligands. Once these dendritic ligands are obtained they will undergo complexation reactions with gallium and copper to form the “cold” metallodendrimers. Finally, the DNA binding capabilities of all the suitable compounds would be evaluated via UV-Vis spectroscopic titrations.

1.1.4 References

(1) Ebbell, B. *The Papyrus Ebers : the greatest Egyptian medical document*; Levin & Munksgaard: Copenhagen, 1937.

(2) Lonardo, A. Di; Nasi, S.; Pulciani, S. *J. Cancer* **2015**, *6*, 29–39.

(3) Hajdu, S. I. *Cancer* **2011**, *117* (12), 2811–2820.

(4) Hajdu, S. I. *Cancer* **2012**, *118* (4), 1155–1168.

(5) Boveri, T. *Zur Frage der Entstehung maligner Tumoren*; G. Fischer, 1914.

(6) Javier, R. T.; Butel, J. S. *Cancer Res.* **2008**, *68*, 7693–7706.

(7) Rous, P. *J. Exp. Med.* **1911**, *13* (4), 397–411.

(8) Henschen, F. *Gann.* **1968**, *59*, 447–451.

(9) Smith, E. The History of Cancer www.cancer.net/patient/Advocacy and Policy/Treatment_Advances_Timeline.pdf.

(10) World Health Organization; Cancer Research UK. *World Heal. Organ.* **2014**, 4.

(11) Gillet, J.-P.; Gottesman, M. M. *Methods Mol. Biol.* **2010**, *596*, 47–76.

(12) Kini, U.; Nandeesh, B. N. *Radionucl. Hybrid Bone Imaging* **2012**, 29–57.

(13) Blanpain, C. *Nat. Cell Biol.* **2013**, *15* (2), 126–134.

(14) Coelho, S. C.; Pereira, M. C.; Juzeniene, A.; Juzenas, P.; Coelho, M. A. N. *J. Control. Release* **2015**, *213*, 152–167.

(15) MacEwan, S. S. R.; Callahan, D. J. D.; Chilkoti, A. *Nanomedicine UK* **2010**, *5* (5), 793–806.

(16) Nune, S. K.; Gunda, P.; Majeti, B. K.; Thallapally, P. K.; Forrest, M. L. *Adv. Drug Deliv. Rev.* **2011**, *63* (10–11), 876–885.

(17) Zhao, Y.; Alakhova, D. Y.; Kabanov, A. V. *Adv. Drug Deliv. Rev.* **2013**, *65* (13–14), 1763–1783.

(18) Khawar, I. A.; Kim, J. H.; Kuh, H. J. *J. Control. Release* **2015**, *201*, 78–89.

(19) Burrell, R. A; McGranahan, N.; Bartek, J.; Swanton, C. *Nature* **2013**, *501* (7467), 338–345.

(20) Steichen, S. D.; Caldorera-Moore, M.; Peppas, N. A. *Eur. J. Pharm. Sci.* **2013**, *48* (3), 416–427.

(21) Estanqueiro, M.; Amaral, M. H.; Conceição, J.; Sousa Lobo, J. M. *Colloids Surfaces B Biointerfaces* **2015**, *126*, 631–648.

(22) Maeda, H. *Adv. Enzyme Regul.* **2001**, *41*, 189–207.

(23) Chen, W. C.; Zhang, A. X.; Li, S.-D. *Eur. J. Nanomedicine* **2012**, *4* (2), 89–93.

(24) Wicki, A.; Witzigmann, D.; Balasubramanian, V.; Huwyler, J. *J. Control. Release* **2015**, *200*, 138–157.

(25) Yatvin, M. B.; Weinstein, J. N.; Dennis, W. H.; Blumenthal, R. *Science* **1978**, *202* (4374), 1290–1293.

(26) Needham, D.; Anyarambhatla, G.; Kong, G.; Dewhirst, M. W. *Cancer Res.* **2000**, *60* (5), 1197–1201.

(27) Mura, S.; Nicolas, J.; Couvreur, P. *Nat. Mater.* **2013**, *12* (11), 991–1003.

(28) Fomina, N.; Sankaranarayanan, J.; Almutairi, A. *Adv. Drug Deliv. Rev.* **2013**, *18* (9), 1199–1216.

(29) Archut, A.; Azzellini, G. C.; Balzani, V.; Cola, L. De; Vogtle, F. *J. Am. Chem. Soc.* **1998**, *1* (12), 12187–12191.

(30) Azagury, A.; Khoury, L.; Enden, G.; Kost, J. *Adv. Drug Deliv. Rev.* **2014**, *72*, 127–143.

(31) Liu, Y.; Wang, W.; Yang, J.; Zhou, C.; Sun, J. *Asian J. Pharm. Sci.* **2013**, *8* (3), 159–167.

(32) Wen, H.; Li, Y. *Med. Chem.* **2014**, *4* (11), 748–755.

(33) Cutler, C. S.; Hennkens, H. M.; Sisay, N.; Huclier-Markai, S.; Jurisson, S. S. *Chem. Rev.* **2013**, *113* (2), 858–883.

(34) Vértes, A.; Nagy, S.; Klencsár, Z.; Lovas, R.; Rösch, F. In *Handbook of Nuclear Chemistry*; Springer, 2011; pp 2179–2183.

(35) Humm, J. L.; Howell, R. W.; Rao, D. V. *Med. Phys.* **1994**, 12, 1901–1915.

(36) Liko, F.; Hindre, F.; Fernandez-Megia, E. *Biomacromolecules* **2016**, *17* (10), 3103–3114.

(37) Chopra, D. In *Radioisotopes – Applications in Bio-Medical Science*; InTech, 2010; pp 225–248.

(38) Hamoudeh, M.; Kamleh, M. A.; Diab, R.; Fessi, H. *Adv. Drug Deliv. Rev.* **2008**, *60* (12), 1329–1346.

(39) Price, E. W.; Orvig, C. *Chem. Soc. Rev.* **2014**, *43* (1), 260–290.

(40) Müller, C.; Zhernosekov, K.; Köster, U.; Johnston, K.; Dorrer, H.; Hohn, A.; van der Walt, N. T.; Türler, A.; Schibli, R. *J. Nucl. Med.* **2012**, *53* (12), 1951–1959.

(41) Jalilian, A. R.; Osso, J. J. *Iran J. Nucl. Med* **2016**, *25* (1), 1–10.

(42) Abada, S.; Lecointre, A.; Charbonni, J. *Dalton Transactions* **2010**, No. 39, 9055–9062.

(43) Jones-Wilson, T. M.; Deal, K. A.; Anderson, C. J.; Mccarthy, D. W.; Kovacs, Z.; Motekaitis, R. J.; Sherry, A. D.; Martell, A. E.; Welch, M. J. *Nucl. Med. Biol.* **1998**, *25*, 523–530.

(44) Sun, X.; Wuest, M.; Weisman, G. R.; Wong, E. H.; Reed, D. P.; Boswell, C. A.; Motekaitis, R.; Martell, A. E.; Welch, M. J.; Anderson, C. J. *J. Med. Chem.* **2002**, 469–477.

(45) Ferdani, R.; Stigers, D. J.; Fiamengo, A. L.; Wei, L.; Li, B. T. Y.; Golen, J. A.; Rheingold, A. L.; Weisman, G. R.; Wong, H.; Anderson, C. J. *Dalton Transactions* **2012**, *41*, 1938–1950.

(46) Tyr, A.; Nedrow, J. R.; White, A. G.; Modi, J.; Nguyen, K.; Chang, A. J.; Anderson, C. J. *Mol Imaging* **2014**, 1–25.

(47) Wu, N.; Kang, C. S.; Sin, I.; Ren, S.; Lui, D.; Ruthengael, V. C.; Lewis, M. R.; Chong, H.-S. *J. Biol. Inorg. Chem.* **2016**, 21 (2), 177–184.

(48) Panwar, P.; Singh, S.; Kumar, N.; Rawat, H.; Mishra, A. K. *Bioorg. Med. Chem.* **2007**, *15* (2), 1138–1145.

(49) Motaleb, M. a.; Sakr, T. M. *J. Label. Compd. Radiopharm.* **2011**, *54* (9), 597–601.

(50) Bordoloi, J. K.; Berry, D.; Khan, I. U.; Sunassee, K.; de Rosales, R. T. M.; Shanahan, C.; Blower, P. J. *Dalton Transactions* **2015**, *44* (11), 4963–4975.

(51) Ogawa, K.; Mukai, T.; Inoue, Y.; Ono, M.; Saji, H. *J. Nucl. Med.* **2006**, *47* (12), 2042–2047.

(52) Liu, S. *Adv. Drug Deliv. Rev.* **2008**, *60* (12), 1347–1370.

(53) Holub, J.; Meckel, M.; Kubíček, V.; Rösch, F.; Hermann, P. *Contrast Media Mol. Imaging* **2015**, *10* (2), 122–134.

(54) Bartholomä, M. D. *Inorganica Chim. Acta* **2012**, *389*, 36–51.

(55) Horiguchi, M.; Kandatsu, M. *Nature* **1959**, *184* (12), 901–902.

(56) Huang, J.; Chen, R. *Heteroat. Chem.* **2000**, *11* (7), 480–492.

(57) Constantino, F.; Ienco, A.; Taddei, M. In *Tailored Organic-Inorganic Materials*; Wiley, 2015; p 480.

(58) Naydenova, E. D.; Todorov, P. T.; Troev, K. D. *Amino Acids* **2010**, *38* (1), 23–30.

(59) Kukhar, V. P.; Romanenko, V. D. *Chemistry of Aminophosphonic Acids and Phosphonopeptides*; Wiley, 2010; Vol. 2.

(60) Yin, P.; Tian, Y.; Wang, Z.; Qu, R.; Liu, X.; Xu, Q.; Tang, Q. *Mater. Chem. Phys.* **2011**, *129* (2), 168–175.

(61) Cherkasov, R. A.; Garifzyanov, A. R.; Talan, A. S.; Davletshin, R. R.; Kurnosova, N. V. *Russ. J. Gen. Chem.* **2009**, *79* (9), 1835–1849.

(62) Cortes-Clerget, M.; Gager, O.; Monteil, M.; Pirat, J.-L.; Migianu-Griffoni, E.; Deschamp, J.; Lecouvey, M. *Adv. Synth. Catal.* **2016**, *358* (1), 34–40.

(63) Bálint, E.; Fazekas, E.; Pongrácz, P.; Kollár, L.; Drahos, L.; Holczbauer, T.; Czugler, M.; Keglevich, G. *J. Organomet. Chem.* **2012**, *717*, 75–82.

(64) Kim, H. J.; Seo, J.; Rose, M. J. *ACS Appl. Mater. Interfaces* **2016**, *8* (2), 1061–1066.

(65) Mutin, P. H.; Guerrero, G.; Vioux, A. *J. Mater. Chem.* **2005**, *15* (35–36), 3761–3768.

(66) Xyla, A. G.; Mikroyannidis, J.; Koutsoukos, P. G. *J. Colloid lnterface Sci.* **1992**, *153* (2), 537–551.

(67) Veen, I. Van Der; Boer, J. De; van der Veen, I.; de Boer, J. *Chemosphere* **2012**, *88* (10), 1119–1153.

(68) Eash, D. T.; Bushway, R. J. *J. Chromatogr. A* **2000**, *880* (1–2), 281–294.

(69) Collins, D. A. *J. Stored Prod. Res.* **2006**, *42* (4), 395–426.

(70) Singh, B. K.; Walker, A. *FEMS Microbiol. Rev.* **2006**, *30* (3), 428–471.

(71) Abdelkader, H.; Salah, C.; Nadjib, C. *Int. J. Sci. Eng. Res.* **2015**, *6* (8), 1622–1627.

(72) Colovic, M. B.; Krstic, D. Z.; Lazarevic-Pasti, T. D.; Bondzic, A. M.; Vasic, V. M. *Curr. Neuropharmacol.* **2013**, *11* (3), 315–335.

(73) Worek, F.; Thiermann, H.; Szinicz, L.; Eyer, P. *Biochem. Pharmacol.* **2004**, *68* (11), 2237–2248.

(74) Shaunak, S. *Biochem. Biophys. Res. Commun.* **2015**, *468* (3), 435–441.

(75) Winnicka, K.; Wroblewska, M.; Wieczorek, P.; Sacha, P. T.; Tryniszewska, E. A. *Molecules* **2013**, *18* (7), 8607–8617.

(76) Fisher, N.; Hilton-Bolt, T.; Edwards, M. G.; Haxton, K. J.; McKenzie, M.; Allin, S. M.; Richardson,

A. *ACS Med. Chem. Lett.* **2014**, *5* (1), 34–39.

(77) Venkatramaiah, N.; Pereira, P. M. R.; Almeida Paz, F. A.; Ribeiro, C. A. F.; Fernandes, R.; Tome, J. P. C. *Chem. Comm.* **2015**, *51* (85), 15550–15553.

(78) Weekes, D. M.; Ramogida, C. F.; Jaraquemada-pela, M. D. G.; Patrick, B. O.; Apte, C.; Kostelnik, T. I.; Cawthray, J. F.; Murphy, L.; Orvig, C. *Inorg. Chem.* **2016**, *55* (24), 12544–12558.

(79) Griffe, L.; Poupot, M.; Marchand, P.; Maraval, A.; Turrin, C.-O.; Rolland, O.; Metivier, P.; Bacquet, G.; Fournie, J.-J.; Caminade, A.-M.; Poupot, R.; Griffe, L.; Poupot, M.; Marchand, P.; Maraval, A.; Turrin, C.-O.; Rolland, O.; Métivier, P.; Bacquet, G.; Fournié, J.-J.; Caminade, A.-M.; Poupot, R.; Majoral, J.-P. *Angew. Chemie-Int. Ed.* **2007**, *46*, 2523–2526.

(80) Hayder, M.; Poupot, M.; Baron, M.; Nigon, D.; Turrin, C.-O.; Caminade, A.-M.; Majoral, J.-P.; Eisenberg, R. a; Fournié, J.-J.; Cantagrel, A.; Poupot, R.; Davignon, J.-L. *Sci. Transl. Med.* **2011**, *3* (81), 81–35.

(81) Caminade, A.-M.; Fruchon, S.; Turrin, C.-O.; Poupot, M.; Ouali, A.; Maraval, A.; Garzoni, M.; Maly, M.; Furer, V.; Kovalenko, V.; Majoral, J.-P.; Pavan, G. M.; Poupot, R. *Nat. Comm.* **2015**, *6*, 7722.

(82) Caminade, A.-M. *Chem. Soc. Rev.* **2016**, *45*, 5174–5186.

(83) Gupta, K. C.; Sutar, A. K. *Coord. Chem. Rev.* **2008**, *252* (12), 1420–1450.

(84) Cozzi, P. G. *Chem. Soc. Rev.* **2004**, *33* (7), 410–421.

(85) Zoubi, W. Al; Kandil, F.; Chebani, M. K. *Arab. J. Chem.* **2016**, *9* (4), 526–531.

(86) Bandi, K. R.; Singh, A. K.; Upadhyay, A. *Electrochim. Acta* **2013**, *105*, 654–664.

(87) Yousif, E.; Al-Amiery, A. A.; Kadihum, A.; Kadhum, A. A. H.; Mohamad, A. B. *Molecules* **2015**, *20* (11), 19886–19899.

(88) Zhang, X.; Zhu, Y.; Wu, X.; He, H.; Wang, G.; Li, Q. *Chem. Rev.* **2014**, *114* (24), 12330–12396.

(89) Da Silva, C. M.; Da Silva, D. L.; Modolo, L. V.; Alves, R. B.; De Resende, M. A.; Martins, C. V. B.; De Fátima, Â. *J. Adv. Res.* **2011**, *2* (1), 1–8.

(90) Dharmaraj, N. *Transistion Met. Chem.* **2001**, *26*, 105–109.

(91) Kumar, K. S.; Ganguly, S.; Veerasamy, R.; De Clercq, E. *Eur. J. Med. Chem.* **2010**, *45* (11), 5474–5479.

(92) Sharma, M.; Chauhan, K.; Srivastava, R. K.; Singh, S. V.; Srivastava, K.; Saxena, J. K.; Puri, S. K.; Chauhan, P. M. S. *Chem. Biol. Drug Des.* **2014**, *84* (2), 175–181.

(93) Moustafa, S. A.; Ali, M. M.; El-Rashedy, A. A. *Beni-Suef Univ. J. Basic Appl. Sci.* **2016**, 1–12.

(94) Mendu, P.; Kumari, C. G.; Ragi, R. *J. Fluoresc.* **2015**, *25* (2), 369–378.

(95) Lange, J. L.; Hayne, D. J.; Roselt, P.; McLean, C. A.; White, J. M.; Donnelly, P. S. *J. Inorg. Biochem.* **2016**, *162*, 274–279.

(96) Kesharwani, P.; Jain, K.; Jain, N. K. *Prog. Polym. Sci.* **2014**, *39* (2), 268–307.

(97) Venkataraman, S.; Hedrick, J. L.; Ong, Z. Y.; Yang, C.; Ee, P. L. R.; Hammond, P. T.; Yang, Y. Y. *Adv. Drug Deliv. Rev.* **2011**, *63* (15), 1228–1246.

(98) Lo, S.-T.; Kumar, A.; Hsieh, J.-T.; Sun, X. *Mol Pharm* **2013**, *10* (3), 793–812.

(99) El-Sayed, M.; Ginski, M.; Rhodes, C.; Ghandehari, H. *J. Control. Release* **2002**, *81* (3), 355–365.

(100) Svenson, S.; Tomalia, D. A. *Adv. Drug Deliv. Rev.* **2005**, *57*, 2106–2129.

(101) Lee, I.; Athey, B. D.; Wetzel, A. W.; Meixner, W.; Baker, J. R. *Macromolecules* **2002**, *35* (11), 4510–4520.

(102) Kukowska-Latallo, J. F. J.; Candido, K. K. A.; Cao, Z.; Nigavekar, S. S.; Majoros, I. J.; Thomas, T.

P.; Balogh, L. P.; Khan, M. K.; Baker, J. R. *Cancer Res.* **2005**, *65* (12), 5317–5324.

(103) Gupta, V.; Nayak, S. *J. Appl. Pharm. Sci.* **2015**, *5* (3), 117–122.

(104) Low, S. A.; Kopeček, J. *Adv. Drug Deliv. Rev.* **2012**, *64* (12), 1189–1204.

(105) Lee, C. C.; Gillies, E. R.; Fox, M. E.; Guillaudeu, S. J.; Fréchet, J. M. J.; Dy, E. E.; Szoka, F. C. *Proc. Natl. Acad. Sci.* **2006**, *103* (45), 16649–16654.

(106) Zhu, S.; Hong, M.; Tang, G.; Qian, L.; Lin, J.; Jiang, Y.; Pei, Y. *Biomaterials* **2010**, *31* (6), 1360–1371.

(107) Kaminskas, L. M.; Kelly, B. D.; McLeod, V. M.; Sberna, G.; Owen, D. J.; Boyd, B. J.; Porter, C. J. H. *J. Control. Release* **2011**, *152* (2), 241–248.

(108) Kaminskas, L. M.; Kelly, B. D.; McLeod, V. M.; Sberna, G.; Boyd, B. J.; Owen, D. J.; Porter, C. J. H. *Mol. Pharm.* **2011**, *8* (2), 338–349.

(109) Smith, G. N.; Mickler, E. A.; Hasty, K. A.; Brandt, K. D. *Arthritis Rheum.* **1999**, *42* (6), 1140–1146.

(110) Wu, C.; Gansow, G. A.; Section, C. *Bioorg. Med. Chem. Lett.* **1994**, *4* (3), 449–454.

(111) Laznickova, A.; Biricova, V.; Laznicek, M.; Hermann, P. *Appl. Radiat. Isot.* **2014**, *84*, 70–77.

2 Synthesis and Characterization of Cyclic cored PAMAM, PPI and BA Dendritic Ligands

2.1 Introduction

In this chapter an introduction pertaining to the synthesis of dendrimers is discussed, highlighting the advantages and disadvantages of the divergent and convergent synthetic approaches. Thereafter, a brief summary of heteronuclear macrocycles and the properties it potentially adds to dendrimers when incorporated into the dendritic framework provide the rationale for investigating macrocyclic-cored dendrimers. The subsequent experimental section conveys our results for the synthesis of generation 1 cyclam-cored poly(amidoamine) (PAMAM) dendrimers via a two-step process. The first, a Micheal addition, was attained following a microwave-assisted method before the subsequent amidation step yielded the full generation dendrimer. The attempts made to obtain generation 2 cyclam-cored PAMAM and generation 1 TACN-cored PAMAM dendrimers following the aforementioned two-step method, are also discussed. The last section deals with attempts made to achieve higher generation dendrimers via an alternative nitrile reduction method, where the attempted synthesis of generation 1 cyclam-cored polypropylamine (PPI) and benzyl amine (BA) dendrimers is discussed (Figure 2.1).

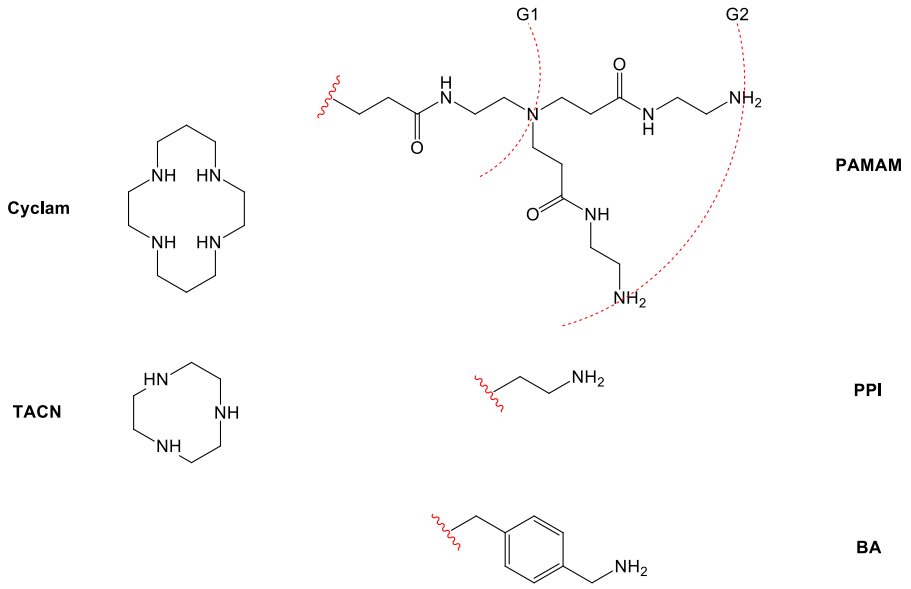

Figure 2.1: General summary of all dendritic target compounds.

2.1.1 Conventional Approaches to Dendrimer Synthesis

Dendrimers are defined as highly branched polymers or macromolecules that are three dimensional, globular, and monodisperse in nature. The first successful attempt to design and create dendrimer molecules was reported by Vögtle and co-workers[1] in 1978 who used the term "cascade molecules" to describe their compounds. After the first report, several years passed before Tomalia *et al.*[2] reported on independent research done by their group at the DOW Chemical Company. In 1984, they coined the term "dendrimer" to describe in detail their divergent synthesis of poly (amidoamine) (PAMAM) dendrimers. Soon thereafter Newkome *et al.*[3] described the synthesis of arborols. The first report on an alternative synthetic approach viz. convergent dendrimer synthesis was published by Frechet[4] in 1990, in which the synthesis of poly-benzylether dendrimers with low polydispersity was reported. There are several reports in literature pertaining to methods for dendrimer synthesis such as: (i) hypercores and branched monomers, (ii) double exponential, (iii) lego chemistry and (iv) click chemistry.[5] Generally all the strategies available for dendrimer synthesis can be grouped into two categories; namely divergent- and convergent synthesis.

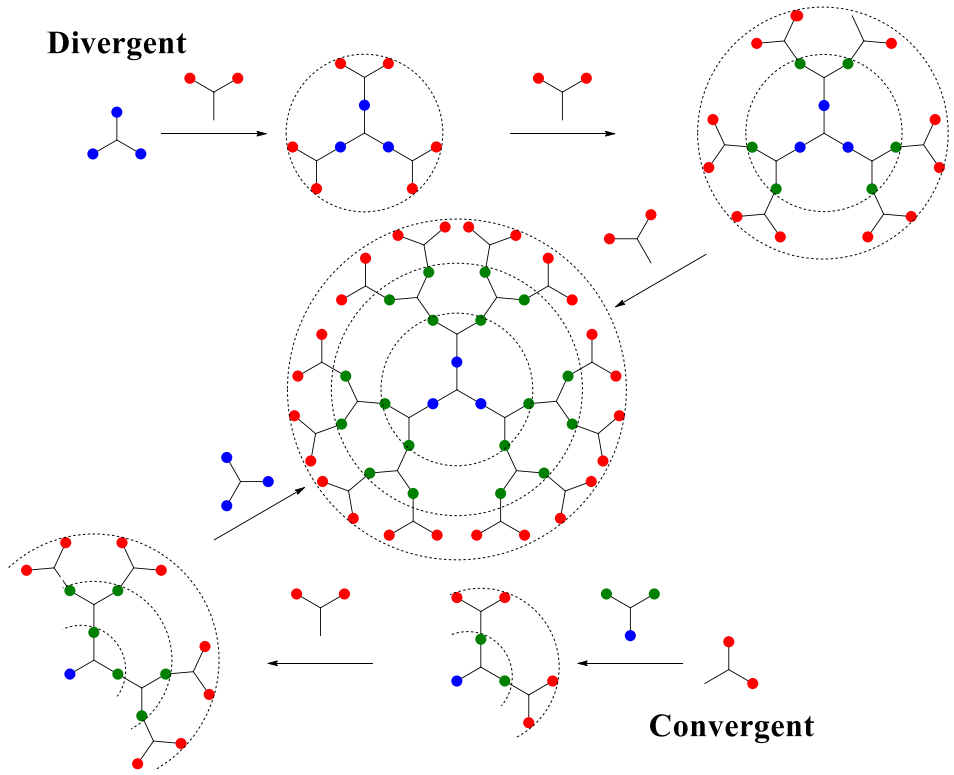

Figure 2.2: Graphical representation of divergent and convergent synthesis.

2.1.1.1 Divergent Synthesis

The divergent approach, which was independently introduced by Vögtle *et al.*[1] and Tomalia *et al.*[2], follows a stepwise construction of dendrimers starting from a multifunctional core molecule and building outwards towards the periphery. This can be achieved by the coupling of branching monomers or the deprotection/ transformation of the branching monomer end group, to create another reactive group capable of coupling a subsequent branching monomer. The divergent synthetic approach offers the ability to achieve high generation dendrimers with surface functionalities that can easily be transformed to alter the dendrimers properties. The divergent approach is the ideal method for commercial scale dendrimer synthesis.[5] There are however some drawbacks worth noting. The rapid increase in the number of end groups combined with the increase in molecular weight results in slower reaction kinetics, which often hampers the synthesis of higher generation dendrimers. Also, as the dendrimer generation increases, it becomes increasingly difficult to separate the desired products from any by-products due to their molecular similarities.[6] PAMAM dendrimers have been used to identify possible imperfections encountered during dendrimer synthesis namely (a) ester hydrolysis leading to a dead branch, (b) retro-Michael addition leading to a missing branch (c) intramolecular cyclization, and (d) intermolecular cyclization.[7]

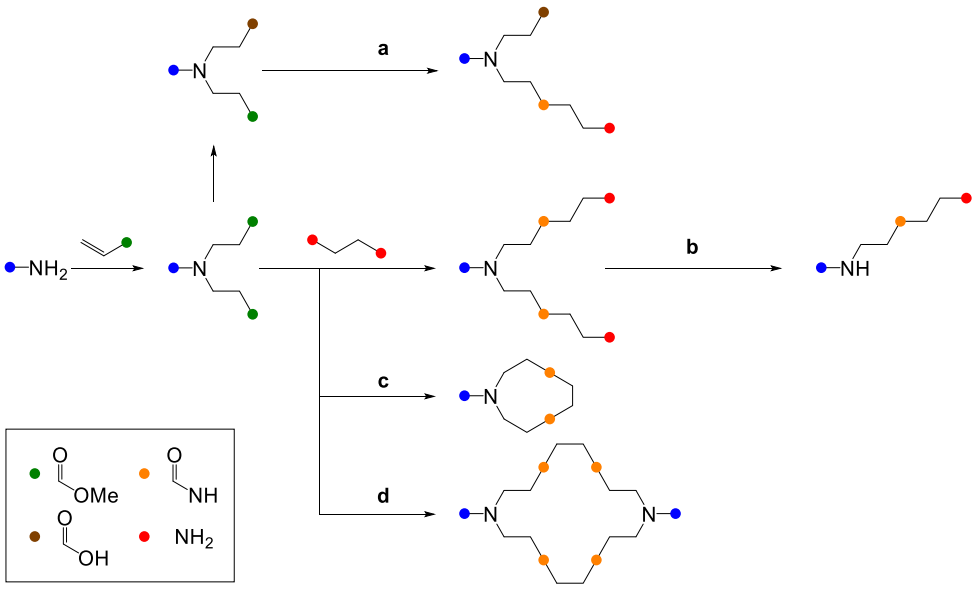

Figure 2.3: Possible side reactions during PAMAM synthesis: (a) ester hydrolysis leading to a dead branch (b) retro-Micheal addition leading to a missing branch (c) intramolecular cyclization, (d) intermolecular cyclization.

2.1.1.2 Convergent Synthesis

Segment coupling strategies were used for peptide synthesis to overcome the low reactivity of the stepwise divergent synthesis of large oligopeptides.[8] Fréchet *et al.*[4] applied the convergent approach to obtain dendrimers, where the dendrimer is synthesized from the peripheral groups inwards towards the core. Essentially two branching monomers are coupled to create a dendritic segment called a dendron. The subsequent coupling of these dendrons lead to a higher generation dendrimer. Once the desired generation is achieved, the dendrons are bound to a suitable core molecule to create the dendrimer. During the dendron propagation process, the number of reactive sites are kept at a minimum, thus the reaction rates generally remains constant and higher yields are obtained relative to the divergent approach. The convergent approach is also superior when comparing the product purity obtainable, due to the molecular differences between the dendrons and the dendrimers which facilitates easy separation and thus high purity dendrimers.[6] The convergent approach does come with some limitations. In order to obtain higher generations, the amount of coupling reactions during dendron synthesis increase exponentially, thus the consecutive dendrons become more bulky. These bulky dendrons can possibly restrict the subsequent "core coupling reaction". This may lead to situations where entire branches are missing (Figure 2.4).[7]

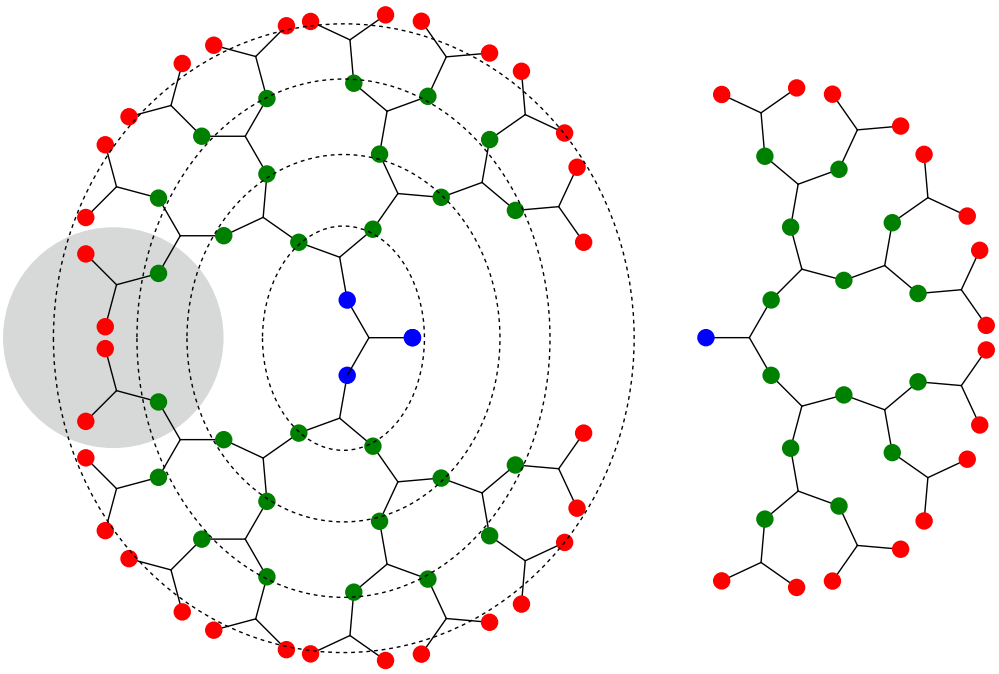

Figure 2.4: Convergent approach; showing possible restriction of "core coupling reaction" due to bulky dendrons.

2.1.2 Macrocycles as dendrimer cores

The step-wise synthesis of dendrimers provide chemists with the control to carefully design dendritic macromolecules. Thus, keeping the intended function in mind, dendrimers can be specifically tailored by incorporating chemical moieties at predetermined sites that contribute specific properties derived from the constituent moieties. One such example is the incorporation of macrocycles into the dendritic structure. These dendrimer-macrocycle conjugates can be categorized into a range of architectures according to the position of the macrocycle. These include dendrimers synthesized with macrocycles at its periphery, a macrocycle at its core, macrocycles at both its periphery and core, macrocycles attached to the interlayer of the dendrimer[9] as well as macrocycles attached to each layer of the dendrimer.[10]

A heteronuclear macrocycle is defined as a cyclic macromolecule containing three or more donor atoms and a ring size of at least nine atoms.[11] Macrocycles containing oxygen donor groups, are known as crown ethers, whereas, those containing nitrogen donor groups, are known as azamacrocycles. The interest shown towards macrocycles was initiated by Pederson, who in the 1960's synthesized a library of polyethers and demonstrated their enhanced complexing ability with a range of alkali and alkali earth metals.[12] Binding constants generally increase as the number of donor atoms per ligand molecule increases. For example, bidentate (two donor atoms per ligand molecule) ligands show improved coordination stability relative to monodentate ligands, as a result of the chelate effect. The rationalization behind the so called chelate effect is twofold. Primarily the substitution of two monodentate ligands by a single bidentate ligand, increase the amount of species in the system. The system becomes more disordered, thus from a thermodynamic point of view, an increase in entropy occurs (Figure 2.5a). Additionally, as soon as the first donor atom of a bidentate ligand coordinate to a metal ion, the second donor atom is restricted to move in close proximity of the metal. The probability of the second donor atom binding to the metal is much greater compared to a monodentate ligand randomly dispersed in solution (Figure 2.5b).

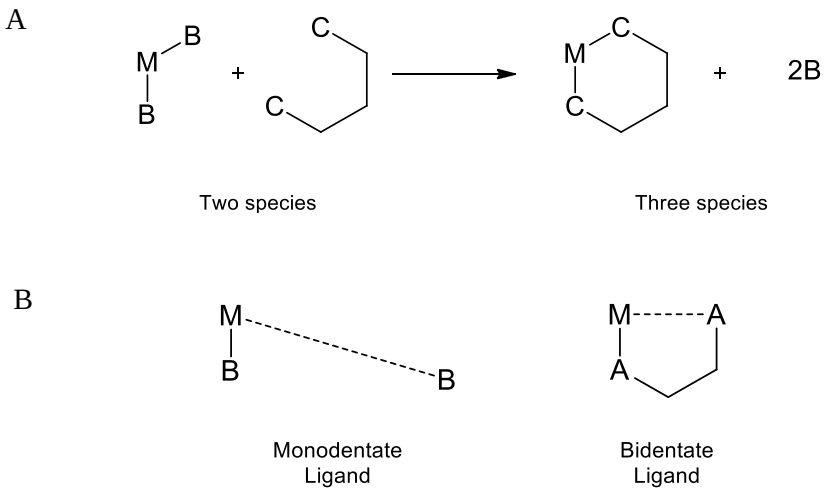

Figure 2.5: The Chelate effect.

In the case of a macrocyclic ligand, all the donor atoms are connected forming a ring structure, which enhances the coordination stability further. This is known as the macrocyclic effect which is a combination of several properties such as the electronics of the donor atoms[13], the molecular geometry, bond length between metal and donor atom, as well as the number and flexibility of the connections between the donor atoms. The conformational attributes of macrocycles ensure their donor atoms are pre-organized. Typically, a macrocycle already resides in the preferred conformation it would adopt upon complexation, thus limited conformational changes are required. Furthermore, the close proximity of the donor atoms in a macrocycle leads to electrostatic repulsion; however, upon complexation the repulsion is lost.

When combining both types of macromolecules (dendrimers and macrocycles), an expected increase in the level of pre-organization is observed which might induce synergistic effects affording interesting properties, different from those produced by the separated entities.[14] The first dendritic compound containing macrocycles in its architecture was reported by Nagasaki and co-workers[15] and concerned a dendrimer bearing azacrown ether macrocycles as constituents of each branch. Dendrimers with macrocycles at its core are known to adopt a unique shape based on the nature of the macrocycle. The chosen macrocycle therefore plays a cooperative role in the dendritic effect observed. The ‘dendritic effect’ is a collective term widely used to describe the unusual physico-chemical properties,

patterns or trends observed for dendrimers as their generations grow. These properties may either be maximised (i.e. a positive effect) or minimized (i.e. negative effect) within a dendrimer series.[16]

2.2 Results and Discussion

The divergent synthesis of PAMAM type dendrimers entails a two-step process. The first step is the Michael addition reaction between methyl acrylate and a suitable amine, followed by an amidation step with ethylenediamine (EDA). The conventional method describes carrying out the Michael addition reaction at room temperature for 3 days followed by the amidation reaction for a further 5 days in the dark.[17] In a bid to develop a method that is not as time consuming as the conventional method, we report herein a method exploiting the advantages of microwave radiation. The advantages of microwave assisted reactions (thermally driven reaction) stems from their mode of energy transfer. Conventional methods rely on conductive heating which is dependent on the thermal conductivity of various materials. Microwave assisted methods induce a rapidly changing electric field directly to the reactants. Any polar or ionic species attempts to orientate itself with the changing field which results in a transfer of energy via dipole rotation or ionic conduction. This method of heating in microwave assisted reactions is more efficient and circumvents the thermal conductivity of materials. Also, the electromagnetic energy of a microwave (300 – 300 000 MHz) affect the molecular rotation of molecules and not the molecular structure. This is due to the low energy of microwave photons (0.037 kcal/mole) relative to the energy required to cleave molecular bonds (80 – 120 kcal/mol).

Following a microwave assisted method, the first step (Micheal addition reaction) could be completed in less than an hour compared to the conventional 3 days. Unfortunately, all attempts to complete the subsequent amidation step via a microwave-assisted method did not yield the desired full generation dendrimers with sufficient purity, hence the conventional method was employed for this step. Furthermore, the cyclam and TACN cored PAMAM dendrimers were characterized via Fourier-transform infrared spectroscopy (FT-IR), proton and carbon nuclear magnetic resonance (^{1}H NMR and ^{13}C NMR) and where possible with mass spectrometry (MS) and elemental analysis (EA).

2.2.1 Synthesis of Cyclam and TACN cored PAMAM dendrimers

The synthesis of G0.5 cyclam-cored PAMAM dendrimer (**D1**) was attempted via the conventional as well as the microwave assisted method. The conventional method, albeit with a low yield of 40 %, was successful. However, employing a microwave assisted method the reaction was completed in significantly less time and higher yields (99 % yield). Reaction Scheme 2.1 depicts the microwave assisted method followed.

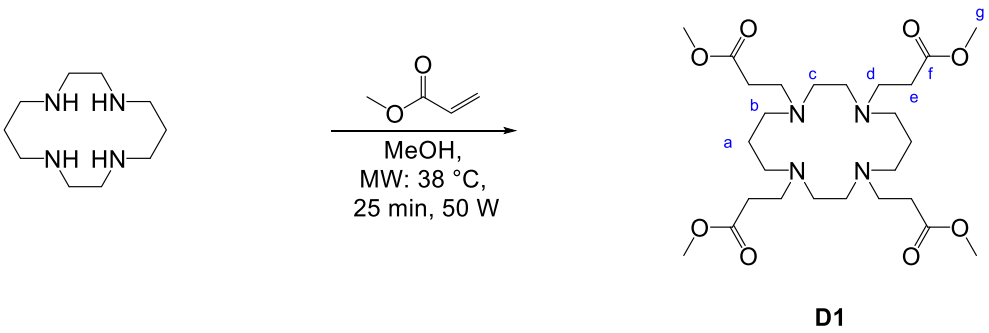

D1

Reaction Scheme 2.1: Microwave-assisted synthesis of D1.

The microwave assisted method previously developed by our group[18] was modified where instead of 15 minutes the reaction was stirred for 25 minutes with only 50 W of radiation compared to 300 W. Thus, the Michael addition was done with 2.5 mole equivalent methyl acrylate per reactive site in the microwave reactor at a controlled temperature of 38 °C with 50 W radiation for 25 minutes. Removal of the solvent and excess methyl acrylate under reduced pressure produced a light yellow/transparent oil. The oil was purified by adding cold hexane and vigorously scratching the oil with a spatula, while submerged in an ice-acetone bath. At this cold temperature, the oil became a white solid after a couple of minutes of trituration. **D1** was isolated via filtration as a white, air stable solid in almost quantitative yield.

The FT-IR spectrum (Figure 2.10: **D1**) displayed a band at 1731 cm^{-1} corresponding to the carbonyl stretch $\nu_{C=O}$. No trace of the ν_{N-H} stretch present in the cyclam starting reagent was observed. In the ^{1}H NMR spectrum, the methoxy protons (Reaction Scheme 2.1: ***g***) was observed as a singlet at 3.64 ppm integrating for a total of 12 protons. The ^{13}C NMR spectrum displayed the carbonyl carbon (Reaction Scheme 2.1: ***f***) at 173.33 ppm. These results correspond with the expected and reported data for **D1**.

The subsequent amidation of **D1** with EDA was attempted via a conventional as well as a microwave-assisted method.[19] The preliminary reactions via the microwave assisted method indicated the presence of several products in the crude material. The FT-IR spectrum showed the carbonyl stretch shift to lower wave numbers as expected, which indicated that all the ester functionalities had reacted. However, in the proton NMR spectrum not only the expected peaks for the product, but various other peaks were observed which are possibly due to inter/ intramolecular crosslinking via the amine functionalities of the EDA and ester functionalities of the dendrimer (Figure 2.6). Several attempts were made to purify the mixture, but attempts on separating the crude products using extraction techniques and based on solvent polarity was unsuccessful. Thus, for the synthesis of G1 cyclam-cored PAMAM dendrimer (**D2**) only the conventional method as described by a literature procedure[17] was pursued further. The conventional method followed is depicted in Reaction Scheme 2.2.

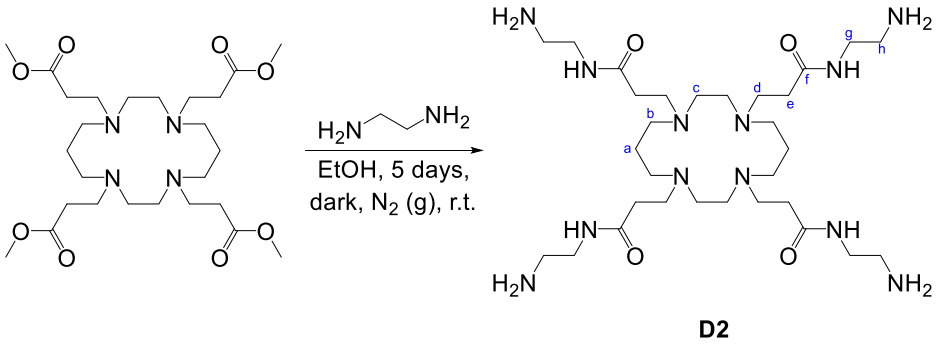

Reaction Scheme 2.2: Conventional synthesis of D2.

The procedure involves adding a large excess EDA as a dilute solution in dry ethanol to **D1** and stirring the sealed reaction mixture at room temperature in the dark for 5 days. Performing the reaction in the dark using a dilute reaction mixture was required to prohibit any inter/ intramolecular crosslinking (Figure 2.6). Removal of the solvent and excess EDA under reduced pressure produced a viscous yellow oil. Purification entailed dissolving the oil in a minimum amount of methanol before submerging the solution in an ice bath. Following this, diethyl ether was slowly added to the vigorously stirring solution. After approximately an hour, a sticky white precipitate was isolated by siphoning of the mother liquor. This process was repeated 3 times before drying the precipitate under reduced pressure to isolate **D2** as an off-white, hygroscopic solid in almost quantitative yield.

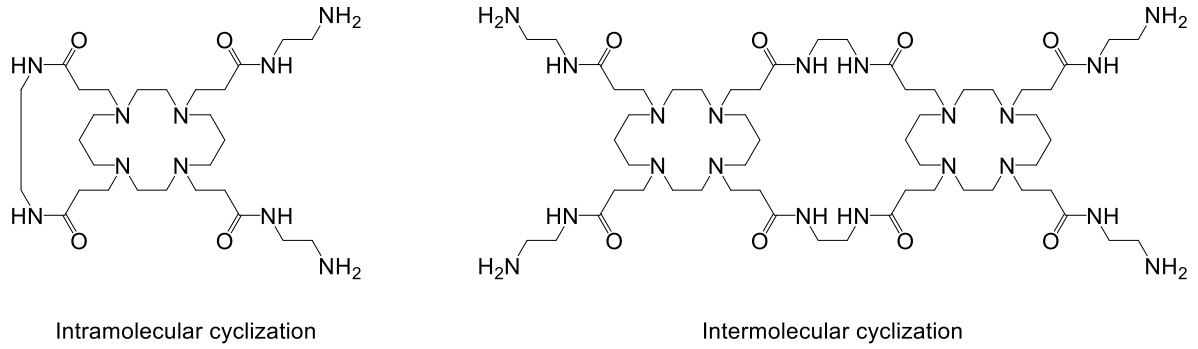

Figure 2.6: Possible inter/ intramolecular crosslinking during D2 synthesis.

The FT-IR spectrum (Figure 2.10: **D2**) displayed a shift of the $\nu_{C=O}$ stretch from 1731 cm^{-1} to 1628 cm^{-1}, which corresponds to the transformation of the ester moiety to an amide. Further characterization by NMR spectroscopy confirmed that the amidation reaction was successful. In the ^{1}H NMR spectrum (Figure 2.7: bottom spectrum) the resonances corresponding to the aliphatic protons (Reaction Scheme 2.2: ***g*** and ***h***) are observed as a doublet of doublets and triplet at 3.28 ppm and 2.81 ppm, respectively. The doublet of doublet stems from the $^{3}J_{H\text{-}NH}$ and $^{3}J_{H\text{-}CH}$ coupling. These resonances are observed at 42.17 ppm (***g***) and 41.66 ppm (***h***) in the ^{13}C NMR spectrum. The resonance of the carbonyl carbon can be seen at 172.87 ppm. The chemical shift for the protons and carbons corresponding to ***d*** and ***e*** in Reaction Scheme 2.2 show no significant shift. These results correspond with the expected and reported data for **D2**.

Additional characterization via elemental analysis indicated that the sample consisted of N: 28.45 %; C: 48.85 %; H: 10.89 %. It should be noted that the sample was hygroscopic and the results suggest that the sample has some ethylenediamine, methanol and water trapped within the dendrimer framework. The calculated values of **D2** with four molecules of ethylenediamine and two molecules each of methanol and water (N: 28.09 %; C: 48.17 %; H: 10.91 %) correspond well with the experimental values. Furthermore, it was possible to identify the molecular ion as well as several fractions from the electrospray ionization mass spectrometry (ESI-MS) results. The spectra obtained indicated the singly charged molecular ion $[M + H]^{+}$ at 657 m/z (Figure 2.8).

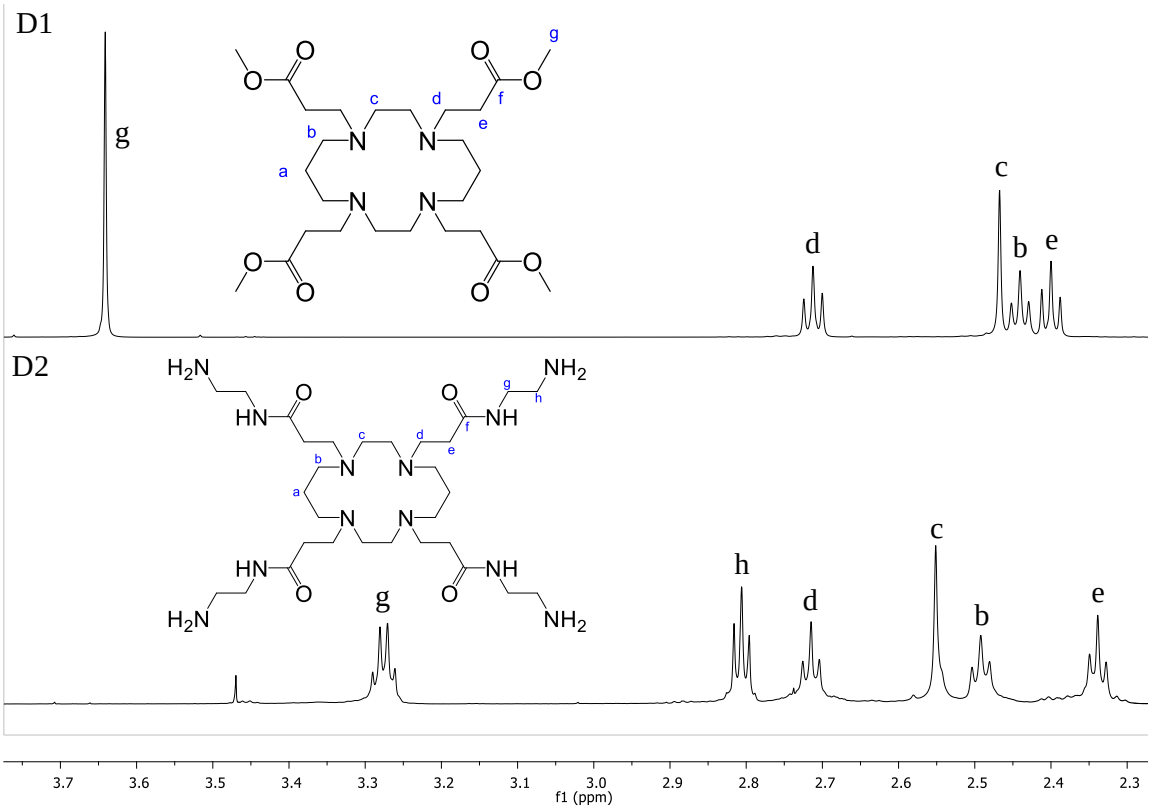

Figure 2.7: Top spectra: ^{1}H NMR of D1; bottom spectra: ^{1}H NMR of D2.

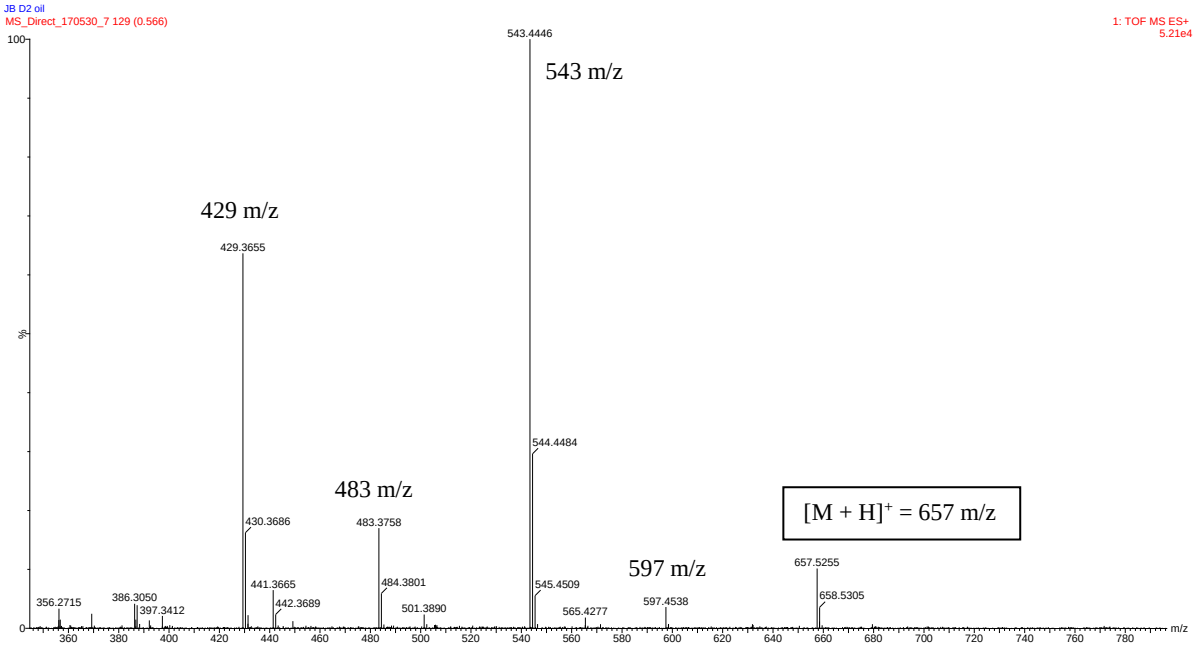

Figure 2.8: ESI-MS spectra of D2.

A plausible fragmentation pathway is depicted in Figure 2.9. The difference from the molecular peak to the peak at 597 m/z corresponds to the ionization of the amide carbon-nitrogen bond (loss of **I**). Further ionization of the carbon-nitrogen bond linking the cyclam and the branches was observed at 543 m/z (loss of **II**). Subsequently, each arm undergoes the same fragmentation as evidenced by the peaks at 483 and 429 m/z which corresponds to the loss of two fragments each of **I** and **II**.

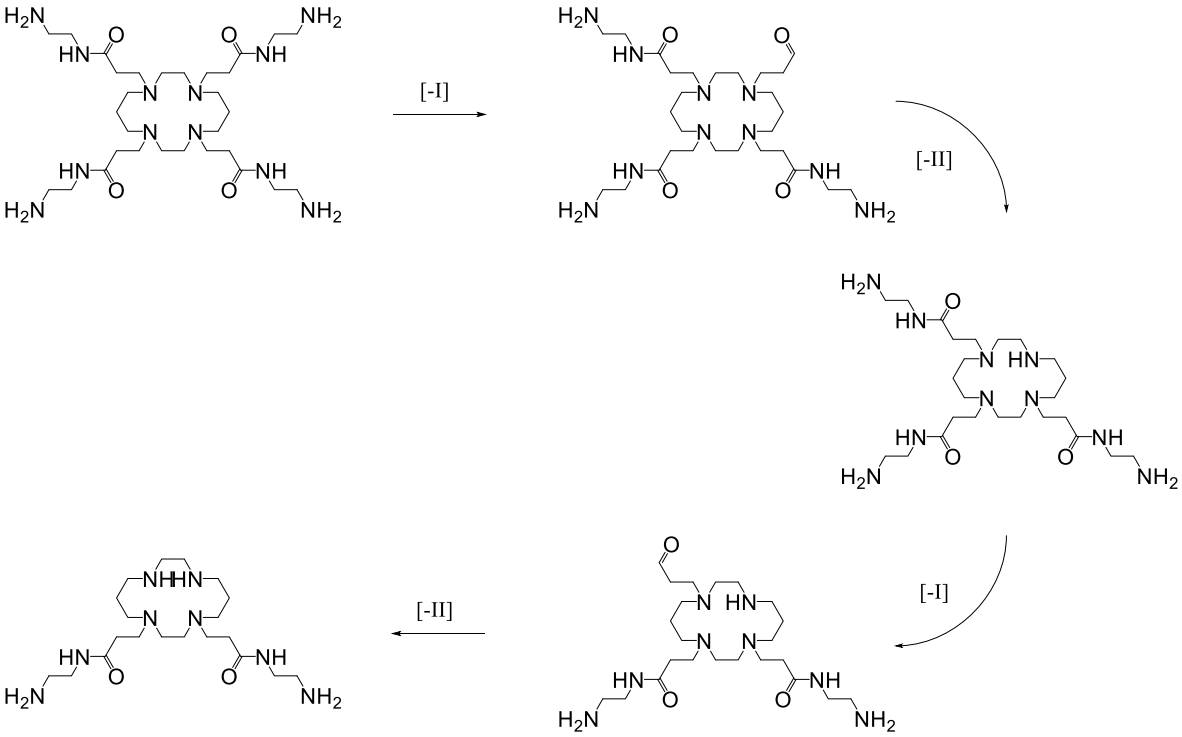

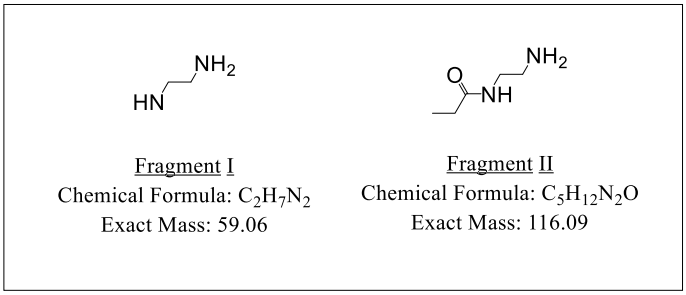

Figure 2.9: Possible fragmentation pattern of D2.

Based on the results above, the synthesis of generation 1 cyclam-cored PAMAM dendrimer was successful. The next step was to attempt the synthesis of generation 2 analogues. Thus, the amine terminated dendrimer **D2** was subsequently subjected to a conventional Michael addition reaction

(Reaction Scheme 2.3) to yield **D3** as a viscous yellow oil in moderate yields. The product was characterized by FT-IR and ^{1}H - and ^{13}C NMR spectroscopy.

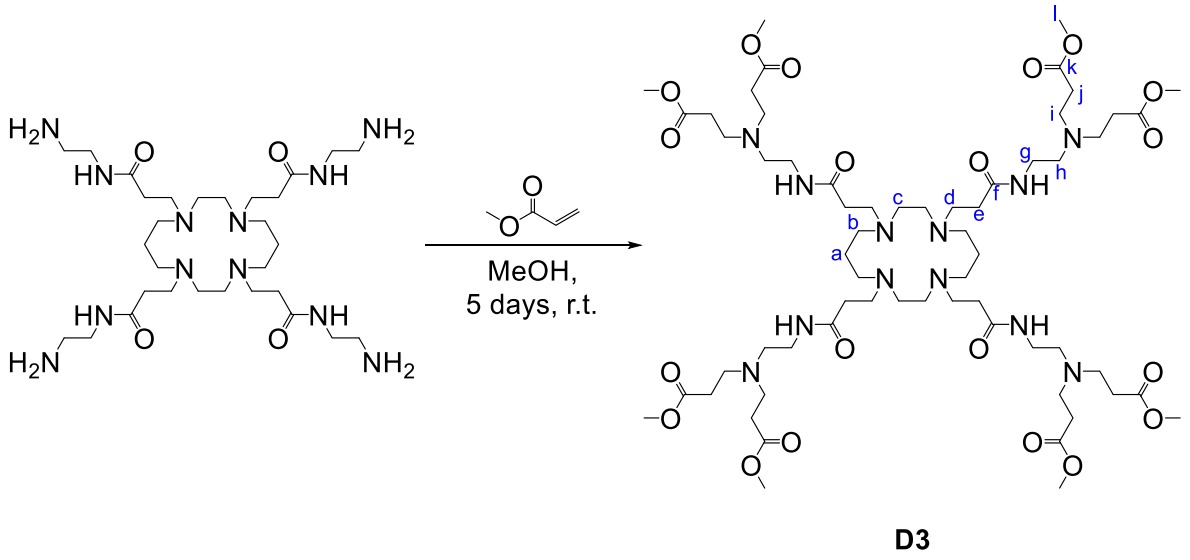

Reaction Scheme 2.3: Conventional synthesis of D3.

The FT-IR spectrum (Figure 2.10: **D3**) shows two $\nu_{C=O}$ bands at 1728 cm^{-1} and 1644 cm^{-1} corresponding to the ester and amide moieties, respectively. The absorption observed at 3308 cm^{-1} is from the secondary amide ν_{N-H} stretch. The ^{1}H NMR spectrum display a triplet resonating at 7.19 ppm corresponding to the amide N-H. The methoxy protons (Reaction Scheme 2.3: ***l***) resonate as a singlet at 3.62 ppm integrating for a total of 24 protons. The protons corresponding to ***d***, ***e***, ***g*** and ***h*** in Reaction Scheme 2.3 are observed at 2.29, 2.49, 2.38 and 2.72 ppm, respectively. In the ^{13}C NMR spectra two carbonyl carbon resonances are seen at 173.00 ppm (Reaction Scheme 2.3: ***k***) and 172.34 ppm (Reaction Scheme 2.3: ***f***) corresponding to the ester and amide moiety. The methoxy carbons (Reaction Scheme 2.3: ***l***) are seen at 49.34 ppm. The characterization data obtained for **D3** corresponded well with the expected data, thus no further characterization was done as **D3** is just an intermediate towards generation 2 cyclam-cored PAMAM dendrimers.

In an attempt to synthesize G2 cyclam-cored PAMAM dendrimer (**D4**), the ester functionalized dendrimer **D3** was subjected to a similar amidation reaction (Reaction Scheme 2.4) followed for the synthesis of **D2**. The method differs from **D2** only in the amount of time it was allowed to stir. After 5 days, a small sample of the reaction mixture was worked up and analyzed via FT-IR which indicated

the presence of unreacted ester moieties still present. This was done several times and after 20 days it was decided to stop the reaction. During the removal of the solvent and EDA, a fine white precipitate was observed in the concentrated solution, which was subsequently isolated via filtration before removing the rest of the solvent and excess EDA to produce a dark yellow viscous oil. The oil was subjected to the same purification procedure described for **D2**.

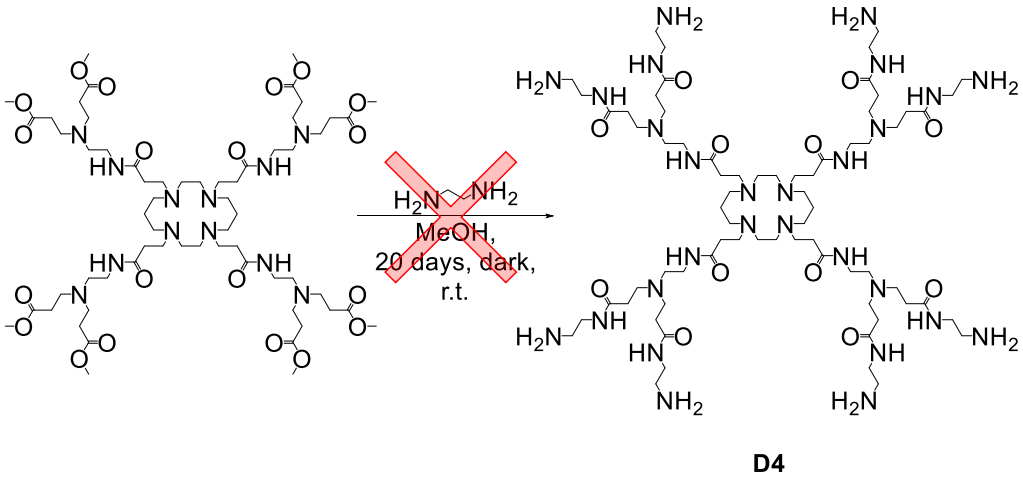

D4

Reaction Scheme 2.4: Attempted Synthesis of D4.

Analysis of the oil via FT-IR (Figure 2.10: **D4**) displayed no more $\nu_{C=O}$ stretch originating from the ester carbonyl of **D3**. The $\nu_{C=O}$ stretch had shifted from 1728 cm^{-1} to 1632 cm^{-1} indicating no ester moiety remained after the reaction. The absorption band at 3259 cm^{-1} represents the amide ν_{N-H} stretch. The ^{1}H NMR spectra of **D4**, obtained in D_2O, show several overlapping peaks in the range of 2.3 – 3.5 ppm, with two distinct triplets at 3.1 ppm and 2.8 ppm which could not accurately be integrated due to the lack of peak resolution. These resonances are most likely caused by a combination of the protons represented by ***g*** and ***l*** for the peaks at 3.2 ppm and a combination of ***h*** and ***m*** for the peaks at 2.8 ppm in Reaction Scheme 2.4. There also seems to be some evidence of methoxy protons resonating around 3.35 ppm. This contradicts the FT-IR results as this would mean that there are still unreacted ester moieties from **D3**. The ^{13}C NMR display more than expected carbonyl carbon resonances in the region of 173 ppm, which supports the evidence that there still remain unreacted ester functionalities. Thus, the crude oil seems to be a combination of several products which could not be separated even after several different attempts to purify and optimize the reaction conditions.

Next, an attempt was made to identify the white precipitate isolated during work-up to clarify what occurred during the reaction. Lopp and co-workers were able to separate a range of side products encountered during the synthesis of G0 – G5 PAMAM dendrimers. They isolated and identified intramolecular cyclization products (Figure 2.3 pathway d) from as early as G1 dendrimer.[20] In an earlier paper they also identified that another source of structural defects occurring with PAMAM is the retro-Michael reaction (Figure 2.3 pathway c). The equilibrium reaction in methanol was evident even at low temperatures (4 – 50 °C). The equilibrium is dependent on temperature, solvent and time.[21]

The FT-IR analysis of the fine white precipitate indicated a sharp ν_{N-H} stretch at 3278 cm^{-1} as well as a $\nu_{C=O}$ stretch at 1670 cm^{-1}. These peaks are expected to appear for the product **D4**. However, further characterization via NMR proved that the white precipitate did not contain any of the peaks corresponding to the cyclam core, nor the PAMAM branches. The ^{1}H NMR spectra (Figure 2.11: Top) of the precipitate showed two triplets and a singlet at 3.31 ppm, 3.07 ppm and 3.00 ppm, respectively. In the ^{13}C NMR spectra (Figure 2.11: Bottom) two resonances appear in the carbonyl region of 160-165 ppm and three peaks in the region of 40 ppm.

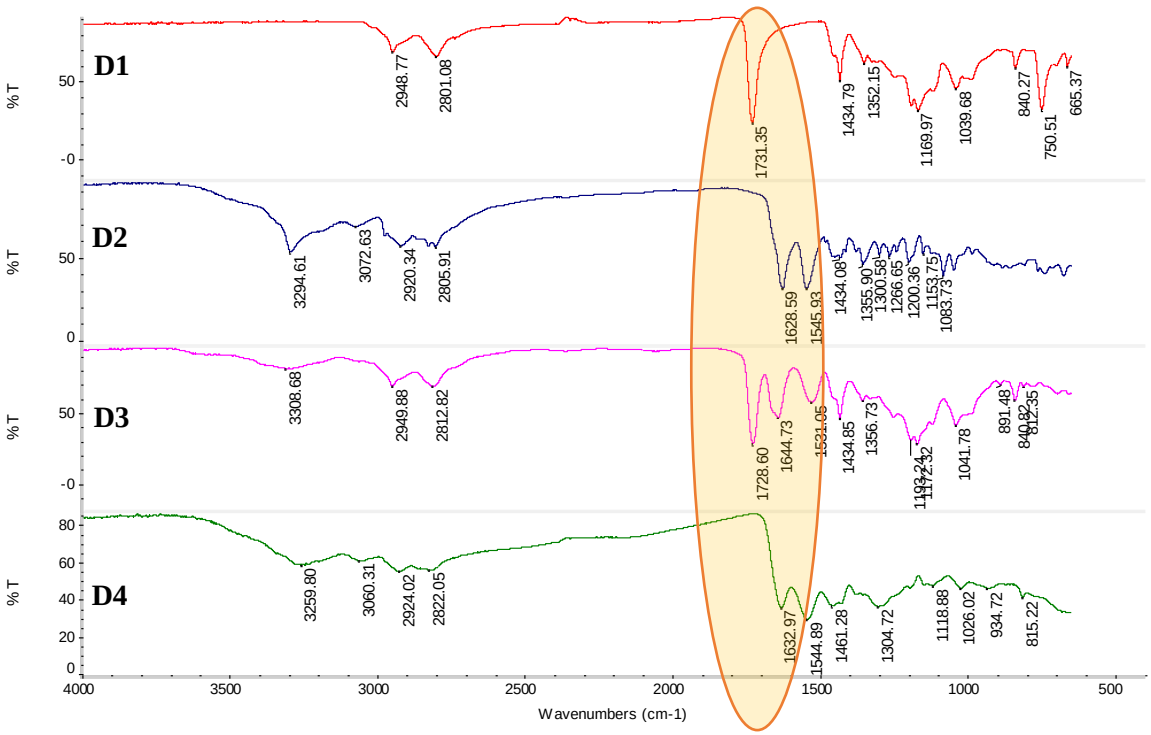

Figure 2.10: FT-IR spectra of D1 - D4.

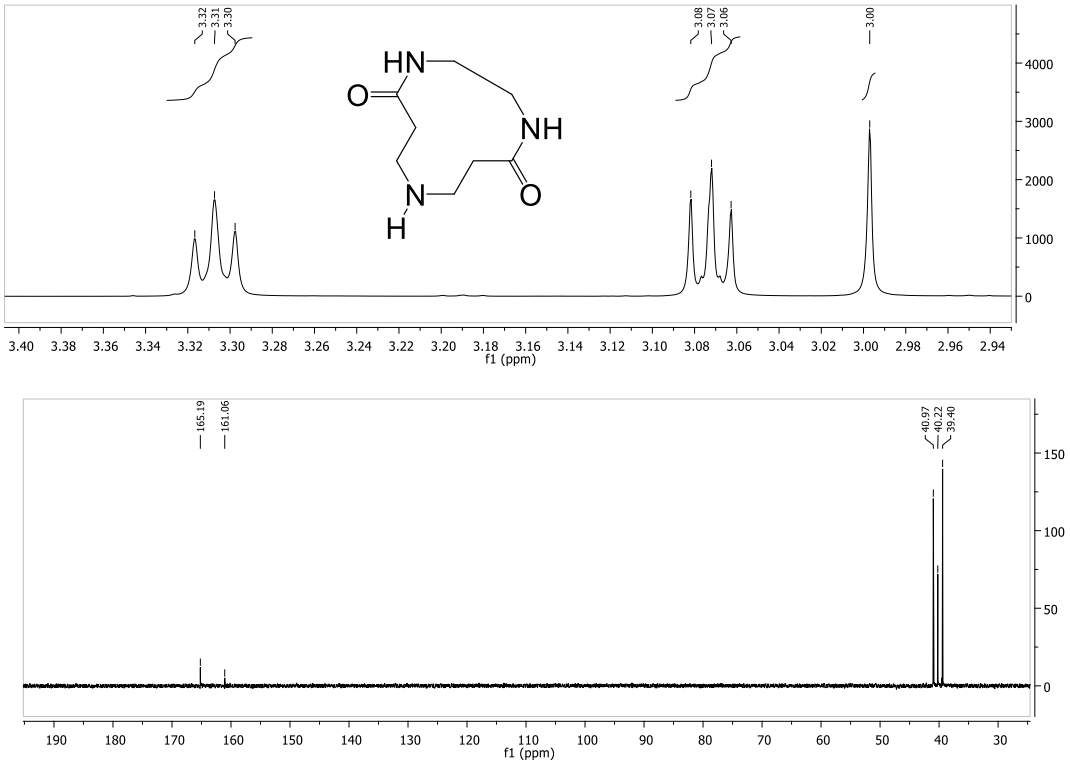

Figure 2.11: Top: ^{1}H NMR of isolated precipitate; Bottom: ^{13}C NMR of isolated precipitate.

The reaction was done in methanol for extended time at room temperature, which varied between 20 – 35 °C, thus according to the findings of Lopp and co-workers it is likely that intramolecular cyclization and retro-Michael addition could occur. The FT-IR and NMR data of the white precipitate suggest evidence of intra-ligand cyclization and corresponds to the proposed structure in Figure 2.12. This species could have formed through a combination of intra-ligand cyclization, hydrolysis and/or retro-Micheal addition; however, neither retro-Michael reaction nor hydrolysis seems plausible to obtain the proposed structure. Further characterization of the precipitate was done by means of microanalysis and ESI MS. In the ESI MS spectra the molecular ion sodium adduct $[M + Na]^{+}$ appeared at 208 m/z and the molecular ion methanol adduct appeared at 218 m/z. However, the elemental analysis results indicated a large difference between the experimental and calculated values based on the proposed structure (Experimental: N: 39.045 %; C: 39.278 %; H: 8.632 %, Calculated: N: 22.69 %; C: 51.88 %; H: 8.16 %). The difference could not be accounted for even with the addition of several combinations of solvent molecules/reagents used during the synthesis. Based on these results the synthesis of **D4** was unsuccessful due to the formation of several side products. Therefore, obtaining

higher generation PAMAM dendrimers is not feasible following this method due to the irreproducibility of the amidation reaction yielding impure crude products that requires tedious purification procedures if at all possible.

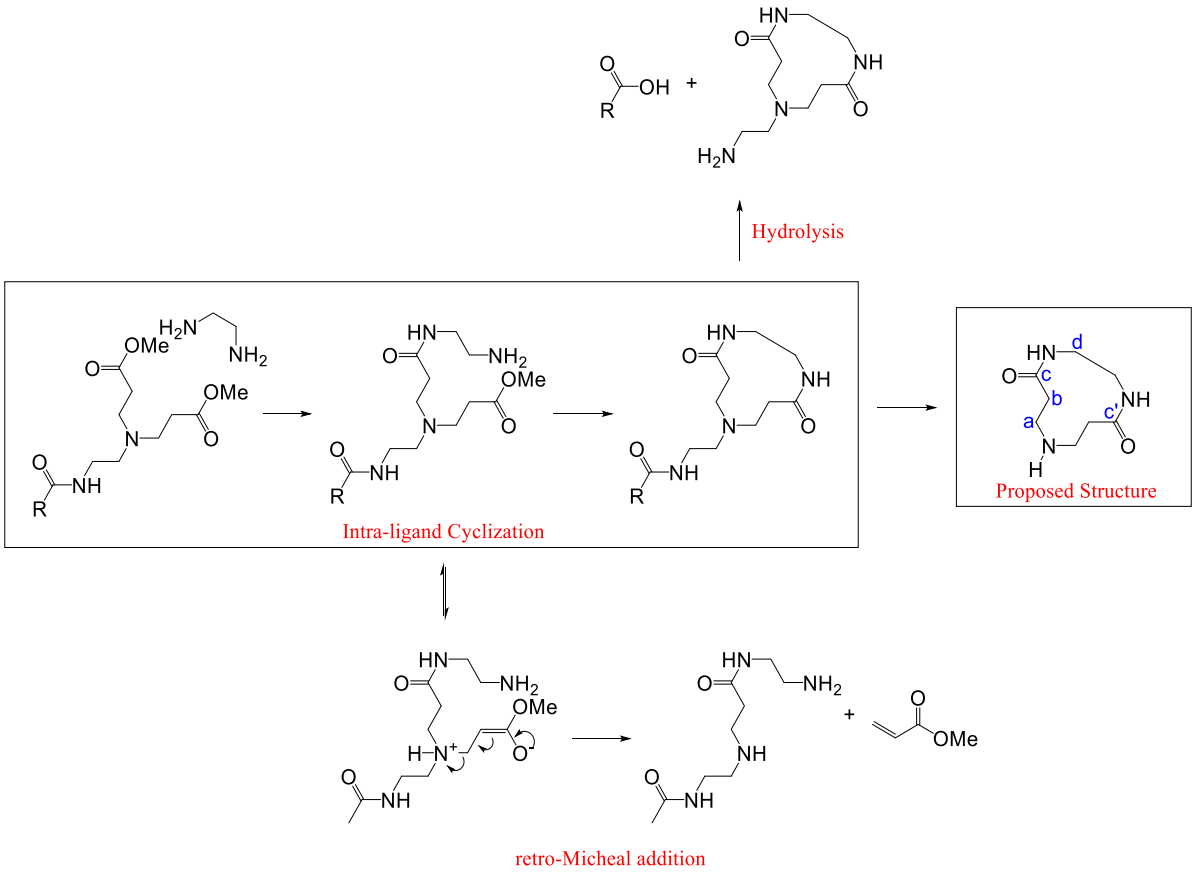

Figure 2.12: Amidation reaction of D4 showing possible side products formed.

In order to obtain higher generation cyclic cored dendrimers other alternatives were pursued. By changing the core molecule, the steric interaction experienced between the dendrimer branches could be altered (Figure 2.4). Thus, 1,4,7-triazacyclononane (TACN) was selected as a viable cyclic core as it only allows 3 branches to grow from its core thereby reducing the steric interaction that may cause hindrance further along the synthesis. Hence, Trimethyl 3,3',3"-(1,4,7-triazonane-1,4,7-triyl)tripropanoate (**D5**) was synthesized according to the microwave-assisted Michael addition reaction discussed above (Reaction Scheme 2.1) and isolated as a white solid (Reaction Scheme 2.5).

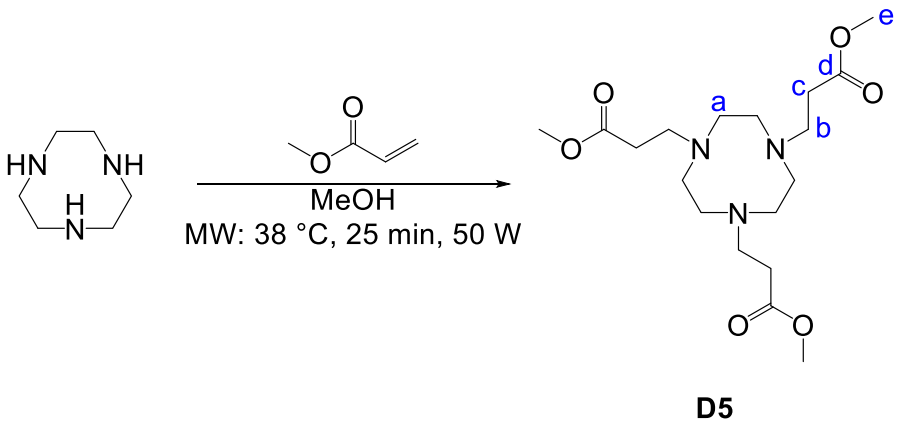

D5

Reaction Scheme 2.5: Microwave-assisted synthesis of D5.

The FT-IR spectrum shows a sharp ester $\nu_{C=O}$ peak at 1731 cm^{-1}. In the ^{1}H NMR spectrum the methoxy protons are expected to resonate in the region of 3.6 - 3.8 ppm and a singlet at 3.65 ppm integrating for a total of 9 protons is assigned to these protons. The ^{13}C NMR spectrum displays the signal for the carbonyl carbon resonating at 173.4 ppm as expected. No further characterization was deemed necessary to continue to synthesize the G1 TACN-cored PAMAM dendrimer.

The tri-ester functionalized TACN dendrimer (**D5**) was subjected to the same amidation procedure previously discussed (Reaction Scheme 2.2) in an attempt to obtain **D6** (Reaction Scheme 2.6).

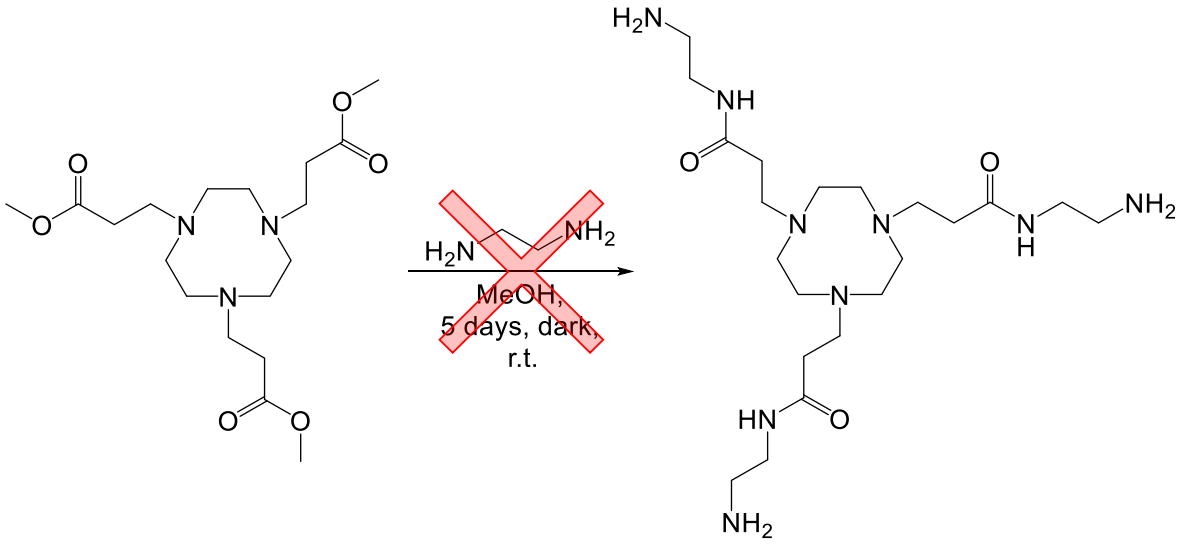

D6

Reaction Scheme 2.6: Attempted synthesis of D6.

The FT-IR spectrum displays a shift in the $\nu_{C=O}$ stretch from 1731 cm^{-1} to 1642 cm^{-1} corresponding to amide carbonyl. The ν_{N-H} band is also observed at 3269 cm^{-1}. In the case of **D6**, the ^{1}H NMR spectrum showed no trace of the signal or the methoxy protons of **D5**. The spectrum displayed several overlapping peaks in the range of 2.4 – 3.4 ppm and as with **D4**, these signals could possibly be due to species in which dendrimer units are cross-linked.

In summary, obtaining higher generation cyclic cored PAMAM dendrimers via the method followed above proved to be cumbersome. The Michael addition proceeded with no trouble and the reaction time was reduced from 3 days to 30 minutes with the microwave assisted method. The FT-IR results (summarized in Table 2.1) indicate a strong $\nu_{C=O}$ stretch in the region 1720 -1730 cm^{-1} for the half generation dendrimers (**D1**, **D3**, **D5)** which was assigned to the carbonyl moiety of the ester functional group. Further characterization via NMR (summarized in Table 2.2 and Table 2.3) supported the success of the Michael addition reactions as evident from the methoxy protons and carbonyl carbons in their respective ^{1}H and ^{13}C NMR. The problem with this synthetic procedure occurred during the amidation step. The FT-IR results of the full generation dendrimers (**D2**, **D4**, **D6)** showed the disappearance of the ester $\nu_{C=O}$ stretch accompanied by the appearance of an amide $\nu_{C=O}$ stretch at lower wavenumbers (1640 cm^{-1}) and a strong ν_{N-H} stretch at 3250 – 3300 cm^{-1}. These results seem promising, but upon further characterization via NMR some impurities/defects were observed, especially with the higher generation dendrimer.

Table 2.1: FT-IR data pertaining to dendrimer synthesis.

Compound	FT-IR (cm^{-1})[d]		
	$\nu(C=O)^{e}$	$\nu(C=O)^{f}$	$\nu(N-H)_{stretch}$
D1[a]	1731	-	-
D2[b]	-	1628	3294
D3[c]	1728	1644	3308
D4[b]	-	1632	3259
D5[a]	1731	-	-
D6[b]	-	1642	3269

Reaction conditions: [a]Mw: 25 min, 38 °C, 50 W; [b]MeOH, r.t. 5 days, dark; [c]MeOH, r.t. 5 days; [d]Recorded as neat spectra on a ZnSe crystal, employing an ATR accessory; [e]Ester; [f]Amide.

Table 2.2: ^{1}H NMR spectral data of dendrimers D1–D6.

Compound	-C(O)OCH$_3$	-C(O)-NH-C**H**$_2$-CH$_2$-NH$_2$	-C(O)-NH-C**H**$_2$-CH$_2$-NH$_2$
D1[a]	3.64 (s, 12H)	-	-
D2[a]	-	3.28 (dd, *J* = 11.7, 5.8 Hz, 8H)	2.81 (t, *J* = 6.0 Hz, 8H)
D3[a]	3.62 (s, 24H)	3.23 (dd, 8H)	2.68 (t, 8H)
D4[b]	3.35 (s)	3.27 (t)	2.81 (t)
D5[a]	3.65 (s, 9H)	-	-
D6[b]	-	3.28 (m)	2.79 (m)

[a]Spectra run in $CDCl_3$ at 25 °C; [b]Spectra run in D_2O at 25 °C. Chemical shifts reported as δ ppm values, referenced relative to residual solvent peak.

Table 2.3: ^{13}C NMR spectral data of dendrimers D1–D6.

Compound	^{13}C NMR (ppm)				
	-C(O)O**C**H$_3$	-**C**(O)OCH$_3$	**C**(O)NH-	**C**H$_2$-CH$_2$-NH$_2$	CH$_2$-**C**H$_2$-NH$_2$
D1[a]	50.61	173.33	-	-	-
D2[a]	-	-	177.75	44.17	42.36
D3[a]	49.34	173.00	172.34	37.21	-
D4[b]	-	-	-	-	-
D5[a]	55.65	173.41	-	-	-
D6[b]	-	173.32	172.74	-	-

[a]Spectra run in $CDCl_3$ at 25 °C; [b]Spectra run in D_2O at 25 °C. Chemical shifts reported as δ ppm values, referenced relative to residual solvent peak.

2.2.2 Synthesis of Cyclic cored PPI and BA dendrimers

Not cowering from the problem at hand, another alternative towards obtaining higher generation cyclic cored dendrimers was attempted. In this case, the use of different branching units were chosen to circumvent the issues occurring during the amidation step of PAMAM branches. Acrylonitrile and 4-bromomethyl benzonitrile were identified as viable Michael acceptors to obtain half generation dendrimers. These dendrimers possessed a nitrile moiety on their peripheries that could subsequently be reduced to yield polypropylenimine (PPI) and benzyl amine (BA) dendrimers. The following section deals with the synthesis of cyclam-cored PPI and BA dendrimers and their characterization via Fourier-transform infrared spectroscopy (FT-IR), proton and carbon nuclear magnetic resonance spectroscopy (^{1}H NMR and ^{13}C NMR) and where possible with mass spectrometry (MS) and elemental analysis (EA).

The synthesis of 3,3',3",3"'-(1,4,8,11-tetraazacyclotetradecane-1,4,8,11-tetrayl)tetrapropanenitrile (**D7)** was previously reported by Wainright.[22] The first step is the Michael addition reaction between cyclam and acrylonitrile, which was done via two methods. The first being a reaction done at room temperature for 24 hours and the second a microwave-assisted reaction as shown above (Reaction Scheme 2.1). In both methods, the product was isolated as a white crystalline precipitate in moderate to high yields (≈ 80 % yield). The numbering used for the following discussion is depicted in Reaction Scheme 2.7.

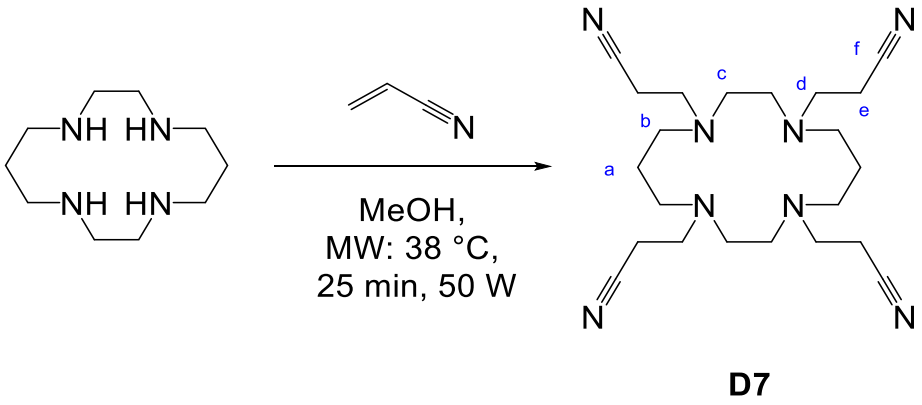

Reaction Scheme 2.7: Microwave-assisted synthesis of D7.

The FT-IR spectrum (Figure 2.13: **D7**) displayed no ν_{N-H} stretch originating from cyclam and a sharp ν_{CN} at 2243 cm^{-1}. The ^{1}H NMR spectra showed two triplets resonating at 2.57 and 2.75 ppm corresponding to the aliphatic protons ***e*** and ***d***, respectively. The corresponding signals were also observed in the ^{13}C NMR spectrum at 51.40 ppm (***d***) and 16.51 ppm (***e***). The resonance corresponding to the nitrile carbon (***f***) was observed at 119.36 ppm. These observations confirm that the microwave-assisted Michael addition was successful.

The subsequent reduction step has previously been attempted by our group. The use of $LiAlH_4$ and $NaBH_4$ as reducing agents yield a mixture of products. The use of Raney-Nickel and KBH_4 also showed only partial reduction.[23] In order to acquire 3,3',3",3"'-(1,4,8,11-tetraazacyclotetradecane-1,4,8,11-tetrayl)tetrakis(propan-1-amine) (**D8)**, a modified procedure previously reported by Wainright[24,25] was followed (Reaction Scheme 2.8).

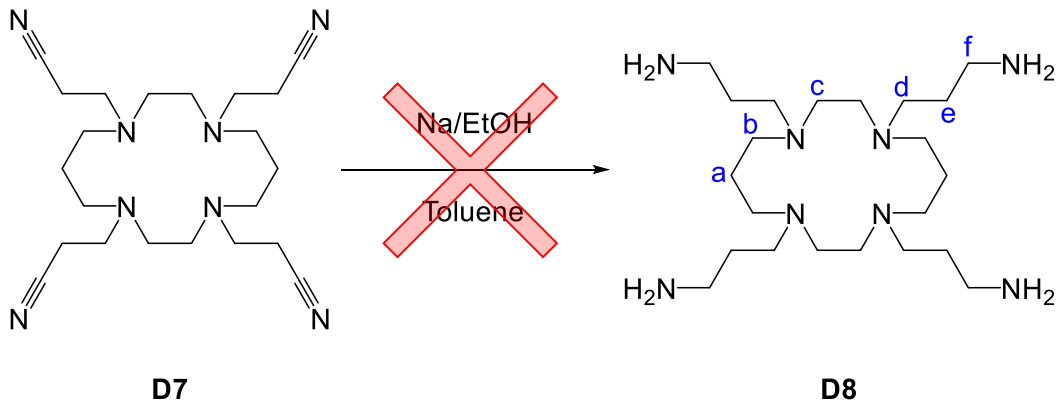

D7 **D8**

Reaction Scheme 2.8: Attempted synthesis of D8.

D7 was refluxed in toluene with solid sodium metal suspended in the light-yellow solution. After 20 hours, dry ethanol was slowly added which resulted in the formation of H_2 gas bubbling through the solution. The ethanol was added in a manner to sustain more or less a constant source of H_2. After approximately 3 hours all the sodium had dissolved and no more H_2 was released. The reaction mixture was refluxed an additional 24 hours. The warm reaction mixture was allowed to cool, upon which the sodium ethoxide quickly crystalized from the solution. An attempt to isolate the product via filtration yielded extremely low yields even after extensive rinsing with toluene. An alternative isolation method was attempted by adding a small amount of water (to dissolve the sodium ethoxide) and quickly separating the aqueous and organic phase. Removal of the solvent yielded a yellow/brown residue.

The FT-IR spectrum (Figure 2.13: **D8**) concluded that, although no nitrile was present as evident by the absence of the ν_{CN} at 2243 cm^{-1}, a broad stretch in the region of 3294 cm^{-1} and several undefined bands around 1634 cm^{-1} indicate a mixture of amine and imine products were present. In the ^1H NMR spectrum several undefined overlapping peaks were observed and the peak of interest, the aliphatic protons (***f***) which should resonate in the region of 3.6 ppm, could not be identified. Several resonances were observed in the range of 7.0 -7.5 ppm, which substantiate the observations made in the FT-IR spectrum, that a mixture of amine and imine products were present. Unfortunately, after several purification attempts the mixture of products was deemed inseparable.

The synthesis of 4,4',4",4'"-((1,4,8,11-tetraazacyclotetradecane-1,4,8,11-tetrayl)tetrakis (methylene))tetrabenzonitrile **(D9)** has previously been reported by Comba.[26] The first step is the

nucleophilic addition reaction between cyclam and 4-bromomethyl benzonitrile in a biphasic reaction. The product was extracted with chloroform before purification via recrystallization yielded the product as a white crystalline precipitate in moderate to high yields (≈ 80 % yield).

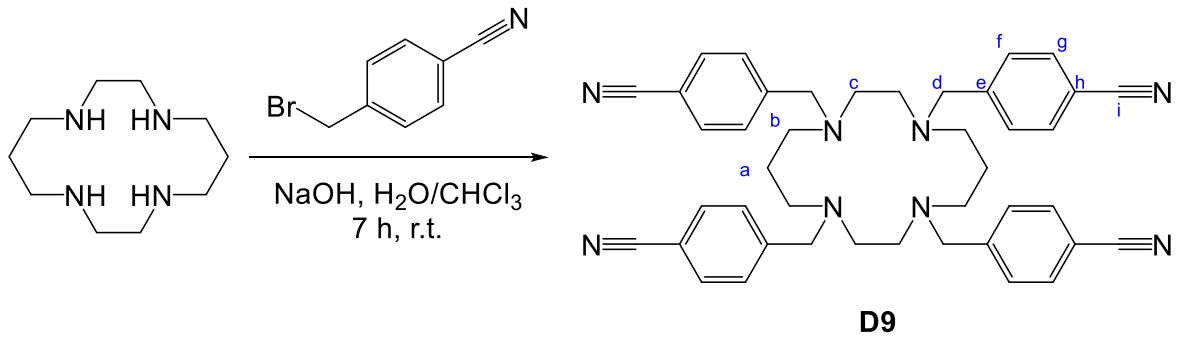

Reaction Scheme 2.9: Synthesis of D9.

The FT-IR spectrum (Figure 2.13: **D9**) displayed the absence of the ν_{N-H} stretch originating from cyclam while a sharp ν_{CN} stretch is now observed at 2223 cm^{-1}. The ^{1}H NMR spectrum showed a singlet resonating at 3.42 ppm integrating to 8 protons which correlate to the methylene protons (***d***) attached to the carbon in between the core and the benzene ring. These resonances were observed at 58.81 ppm (***d***) in the ^{13}C NMR. The resonance corresponding to the aromatic carbons appear in the range of 145 – 110 ppm (***e-h***) and the nitrile carbon was observed at 118.97 ppm (***i***).

The sodium/ethanol and the Raney Ni reduction followed for **D8** were also applied to **D9** in an attempt to acquire (((1,4,8,11-tetraazacyclotetradecane-1,4,8,11-tetrayl)tetrakis(methylene))tetrakis (benzene-4,1-diyl))tetramethanamine **(D10)**.

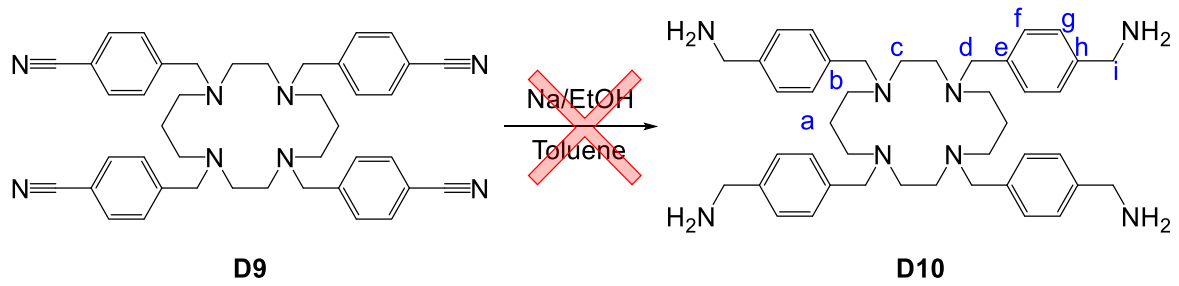

Reaction Scheme 2.10: Attempted synthesis of D10

The FT-IR spectra (Figure 2.13: **D10**) concluded the same results as observed before. **D10** showed no ν_{CN} at 2223.88 cm^{-1} and broad stretches in the region of 3302.43 cm^{-1} and 1633.93 cm^{-1}. The ^{1}H NMR spectrum displayed several undefined overlapping peaks. The aromatic protons (***e-f***) were observed in their expected region of 7.0-7.5 ppm; however as with **D8**, the peak between the aromatic ring and the primary amine (***i***) could not be identified. Similar to **D8**, **D10** most likely consisted of a mixture of amine and imine products which was inseparable.

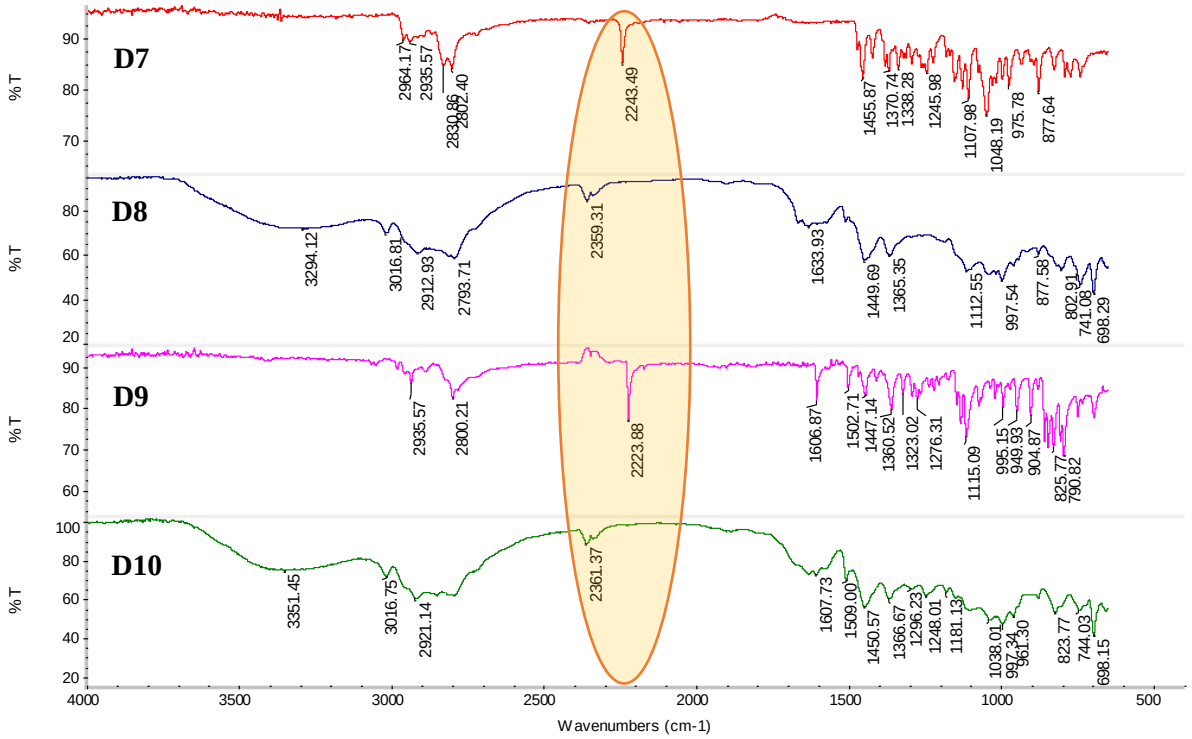

Figure 2.13: FT-IR spectra of D7 – D10.

In summary, the nitrile reduction step for **D8** and **D10** discussed above was not successful. It seems the reduction does occur as there was no sign of the ν_{CN} stretch in their FT-IR spectra coupled with a clear change in the colour of the reaction mixture. However, various spots were observed on thin layer chromatography (TLC) and the NMR results could not be assigned unambiguously. Thus, it is likely that the reduction step was either incomplete or side reactions occurred to yield a mixture of products. Isolating the desired product was not successful via the work-up procedures attempted. It is known that the nitriles can be reduced via catalytic hydrogenation. However, neither the use of 5 % Pd/C or 5 %

Pt/C as a catalyst in methanol at 70 ºC and 20 bar H_2 pressure showed complete reduction even after extended reaction time as previously proved by our group.[23] An attempt to reduce **D7** using Raney-Nickel and sodium hydroxide with 15 bar H_2 at 50 °C for 3 hours has previously been reported[27], but unfortunately proved unsuccessful due to the pressure restriction that we were able to operate at. These catalytic reductions usually require higher pressure (> 50 bar).

2.3 Conclusion

In literature, PAMAM dendrimers are commonly used as scaffolds for various applications; however, most examples use commercially available dendrimers. In our case the aim was to incorporate a macrocycle at the core, which meant synthesizing the dendrimer from scratch. In our hands, half generation cyclam-cored PAMAM dendrimers could be synthesized via a microwave-assisted reaction. This simple method consistently yielded **D1**, **D5** and **D7** in high yields as air stable white solids in less than 1 hour compared to the conventional 3 days. **D9** was obtained as a white solid following a biphasic method and the generation 1.5 cyclam-cored PAMAM dendrimer was obtained as a viscous yellow oil via the conventional method. The attempts at a microwave-assisted method for the amidation reaction were not successful, but full generation cyclam-cored PAMAM dendrimer **D2** could be isolated via the conventional method in variable yields (40-90 % yields). The attempts to obtain higher generation cyclam-cored PAMAM dendrimer, **D4**, were unsuccessful and some evidence of cyclization was observed. Alternatively, using TACN as a core to reduce steric interactions in a bid to obtain higher generation TACN-cored PAMAM dendrimer, **D6**, was also unsuccessful. The PAMAM branches were prone to several side reactions, especially during the amidation step. Thus, an alternative route was envisaged where the Michael acceptor possessed a nitrile moiety which could subsequently be reduced to a primary amine. However, neither the cyclam-cored PPI (**D7**) nor BA (**D9**) dendrimers could be reduced to the corresponding amine derivatives (**D8** and **D10**) and the crude consisted of a mixture of products due to incomplete reduction coupled with side reactions.

2.4 Experimental Section

Solvents were obtained from Merck or Kimix and dried by distilling over the appropriate drying agents. Toluene was dried by distillation over sodium/benzophenone. Methanol was dried by distillation over magnesium turnings and iodine while dichloromethane was dried over phosphorus pentoxide. All reagents were purchased from either Sigma Aldrich or Merck and was used without any further purification.

All Infrared spectra were recorded on a Thermo Nicolet Avatar 330 FT-IR spectrometer with a Smart Performer (Zn/Se) ATR attachment. ^{1}H and ^{13}C nuclear magnetic resonance spectra were recorded using a 300 MHz Varian VNMRS, 400 MHz Varian Unity Inova or 600 MHz Varian Unity Inova NMR instrument using deuterated solvents. Chemical shifts (δ) were recorded using the residual solvent peak or external reference (TMS). All chemical shifts are reported in parts per million and all spectra were obtained at 25 °C. Samples for EA analysis were done on a Perkin-Elmer 2400 Series II CHNS/O Elemental Analyzer at the University of Kwa-Zulu Natal. Mass spectra were recorded on a Waters Synapt G2 spectrometer.

2.4.1 Synthesis of G0.5 cyclam-cored PAMAM dendrimer (D1)

Cyclam (2.9970 g, 14.960 mmol) was dissolved in methanol (15 ml) before adding methyl acrylate (13.5 ml, 150 mmol) to the stirring solution. The reaction mixture was placed in the microwave reactor for 25 minutes at 38 °C controlled temperature with 50 W radiation. Once the reaction was completed the solvent and excess methyl acrylate was removed via rotary evaporator to afford a yellow oil. The oil was submerged in an ice bath before triturating with cold hexane to yield a white precipitate. The solid was filtered and dried under reduced pressure (**D1**: 8.042 g, 99 % yield). FT-IR (cm^{-1}) υ(C=O) = 1731 cm^{-1}. ^{1}H NMR (600 MHz, $CDCl_3$) δ 3.64 (s, 12H, -C(O)O-C**H**$_3$), 2.71 (t, $^{3}J_{H-H}$ = 7.2 Hz, 8H, -N-C**H**$_2$-CH_2-COO-), 2.47 (s, 8H, -N-C**H**$_2$-C**H**$_2$-N-), 2.44 (t, $^{3}J_{H-H}$ = 6.8 Hz, 8H, -N-C**H**$_2$-CH_2-C**H**$_2$-N-), 2.40 (t, $^{3}J_{H-H}$ = 7.2 Hz, 8H, -N-CH_2-C**H**$_2$COO-), 1.53 (p, $^{3}J_{H-H}$ = 6.8 Hz, 4H, -N-CH_2-C**H**$_2$-CH_2-N-). ^{13}C NMR (151 MHz, $CDCl_3$) δ 173.3 (-**C**OO-), 51.6 (-N-**C**H_2-**C**H_2-N-), 51.3 (-N-**C**H_2-CH_2-**C**H_2-N-), 51.3 (-N-**C**H_2-CH_2-COO-), 50.6 (-COO-**C**H_3), 32.4 (-N-CH_2-**C**H_2-COO-), 24.1 ppm (-N-CH_2-**C**H_2-CH_2-N-).

2.4.2 Synthesis of G1 cyclam-cored PAMAM dendrimer (D2)

To a stirring solution of **D1** (6.406 g, 11.76 mmol) in dry methanol (20 ml) ethylenediamine (78.80 ml, 1176 mmol) was added dropwise. The reaction mixture was stirred in the dark at room temperature for 5 days. The solvent and excess ethylenediamine was removed under reduced pressure to yield a yellow oil. The oil was purified by dissolving it in a minimum amount of methanol before transferring the yellow solution to a stirring solution of cold diethyl ether. After 2 hours, the off-white precipitate was isolated by removing the supernatant with a syringe. This purification method was repeated 3 times before drying the resulting product under reduced pressure. (**D2**: 7.714 g, 99 % yield). FT-IR (cm^{-1}) ν(N-H) = 3294 cm^{-1}, ν(C=O) = 1628 cm^{-1}.^{1}H NMR (600 MHz, $CDCl_3$) δ 7.57 (t, *J* = 5.4 Hz, N-H), 3.28 (dd, *J* = 11.7, 5.8 Hz, 8H, -C(O)-NH-C**H**$_2$-CH_2-NH_2), 2.81 (t, *J* = 6.0 Hz, 8H, -C(O)-NH-CH_2-C**H**$_2$-NH_2), 2.71 (t, *J* = 6.5 Hz, 8H, -N-C**H**$_2$-CH_2-COO-), 2.55 (s, 8H, -N-C**H**$_2$-C**H**$_2$-N-), 2.49 (t, *J* = 6.9 Hz, 8H, -N-C**H**$_2$-CH_2-C**H**$_2$-N-), 2.34 (t, *J* = 6.5 Hz, 8H, -N-CH_2-C**H**$_2$-COO-), 1.65 (m, 4H, -N-CH_2-C**H**$_2$-CH_2-N-). ^{13}C NMR (101 MHz, $CDCl_3$) δ 172.8 (**C**=O), 51.1 (-N-**C**H_2-CH_2-**C**H_2-N-), 50.9 (-N-**C**H_2-CH_2-COO-), 50.4 (-N-**C**H_2-**C**H_2-N-), 42.1 (-C(O)-NH-**C**H_2-CH_2-NH_2), 41.6 (-C(O)-NH-CH_2-**C**H_2-NH_2), 33.5 (-N-CH_2-**C**H_2-COO-), 23.9 (-N-CH_2-**C**H_2-CH_2-N-). Elemental analysis Calculated: N, 28.09; C, 48.17; H, 10.91 %; Experimental: N, 28.45; C, 48.85; H, 10.89 %. ESI-MS: $[M + H]^+$ at 657 m/z.

2.4.3 Synthesis of G1.5 cyclam-cored PAMAM dendrimer (D3)

To a stirring solution of **D2** (4.8896 g, 7.4432 mmol) in methanol (30 ml), methyl acrylate (67 ml, 744 mmol) was added before stirring the reaction mixture in the dark for 5 days at room temperature. The solvent and excess methyl acrylate was removed under reduced pressure to obtain a yellow oil and further purified via kugel ruhr. (**D3**: Yellow oil, 8.510 g, 85 % yield). FT-IR (cm^{-1}) $\upsilon(C=O)_{ester}$ = 1728 cm^{-1}, $\upsilon(C=O)_{amide}$ = 1644 cm^{-1}, $\upsilon(N-H)_{stretch}$ = 3308 cm^{-1}. ^{1}H NMR (300 MHz, $CDCl_3$) δ 7.19 (t, *J* = 5.4 Hz, 4H, N-**H**), 3.62 (s, 24H, -C(O)OC**H**$_3$), 3.23 (dd, 8H, -C(O)-NH-C**H**$_2$-CH_2-N-), 2.72 (t, $^3J_{H\text{-}H}$ = 6.7 Hz, 16H, -N-(CH_2-C**H**$_2$-C(O)OMe)$_2$), 2.68 (t, 8H, -C(O)-NH-CH_2-C**H**$_2$-N-), 2.51 (s, 8 H, -N-C**H**$_2$-C**H**$_2$-N-), 2.49 (t, 8H, -N-CH_2-C**H**$_2$-C(O)-NH-), 2.44 (t, 8H, -N-C**H**$_2$-CH_2-C**H**$_2$-N-), 2.38 (t, *J* = 6.7 Hz, 16H, -N-(C**H**$_2$-CH_2-C(O)OMe)$_2$), 2.29 (t, *J* = 7.0 Hz, 8H, -N-C**H**$_2$-CH_2-C(O)-NH-), 1.60 (p, $^3J_{H\text{-}H}$ = 6.8 Hz, 4H, -N-CH_2-C**H**$_2$-CH_2-N-). ^{13}C NMR (101 MHz, $CDCl_3$) δ 173.0 (s, -**C**(O)O-CH_3), 172.3 (s, **C**(O) -

NH), 53.0 (s, -N-**C**H_2-CH_2-**C**H_2-N-), 52.2 (s, -N-**C**H_2-CH_2-C(O)NH-), 51.6 (s, -N-(**C**H_2-CH_2-C(O)O-CH_3)$_2$), 51.5 (s, -N-CH_2-**C**H_2-C(O)NH-), 50.8, 50.2, 49.8 (s, -N-**C**H_2-**C**H_2-N-), 49.3 (s, -C(O)O-**C**H_3), 37.2 (s, -C(O)NH-**C**H_2-CH_2-N-), 33.2, 32.7 (s, -N-(CH_2-**C**H_2-C(O)O-CH_3)$_2$), 32.6 (s, -N-CH_2-**C**H_2-C(O)O-NH-), 24.0 (s, -N-CH_2-**C**H_2-CH_2-N).

2.4.4 Synthesis of G2 cyclam-cored PAMAM dendrimer (D4)

To a stirring solution of **D3** (1.606, 1.194 mmol) in dry methanol (10 ml) ethylenediamine (8.00 ml, 119 mmol) was added dropwise. The reaction mixture was stirred at in the dark at room temperature for 20 days. After 20 days the solution was filtered to isolate fine white precipitate. The solvent of the filtrate and the excess ethylenediamine was removed under reduced pressure to yield a yellow oil. The oil was purified dissolving it in a minimum amount of methanol before transferring the yellow solution to a stirring solution of cold diethyl ether. After 2 hours the off-white precipitate was isolated by removing the supernatant with a syringe. This purification method was repeated 3 times before drying the resulting product under reduced pressure. FT-IR (cm^{-1}) ν(N-H) = 3259 cm^{-1}, ν(C=O) = 1632 cm^{-1}.^{1}H NMR (600 MHz, d_2o) δ 3.67 (q, **EtOH**), 3.27 (t, *J* = 6.3 Hz, 8H, -C(O)-NH-C**H**$_2$-CH_2NH_2), 2.81 (t, *J* = 7.4 Hz, 8H, -C(O)-NH-CH_2-C**H**$_2$-NH_2), 2.76 (s, **EDA**) 2.75 (t, 8H, -N-C**H**$_2$-CH_2-COO-), 2.67 (s, 8H, -N-C**H**$_2$-C**H**$_2$-N-), 2.59 (t, 8H, -N-C**H**$_2$-CH_2-C**H**$_2$-N-), 2.46 (t, *J* = 7.3 Hz, 8H, -N-CH_2-C**H**$_2$-COO-), 1.68 (p, 4H, -N-CH_2-C**H**$_2$-CH_2-N-), 1.20 (t, **EtOH**)

2.4.5 Synthesis of trimethyl 3,3',3''-(1,4,7-triazonane-1,4,7-triyl)tripropanoate (D5)

TACN (0.4229 g, 3.2791 mmol) was dissolved in dry methanol (5 ml) before adding methyl acrylate (2.22 ml, 24.5 mmol) to the stirring solution. The reaction mixture was placed in the microwave reactor for 25 min at a controlled temperature of 38 °C under 50 W radiation. The solvent and excess methyl acrylate was removed under reduced pressure to yield a colourless oil. (**D5**: 1.228 g, 97 % yield). FT-IR (cm^{-1}) ν(C=O) = 1733 cm^{-1}. ^{1}H NMR (600 MHz, $CDCl_3$) δ 3.65 (s, 9H, -C(O)O-C**H**$_3$), 2.81 (t, *J* = 7.2 Hz, 6H, -N-C**H**$_2$-CH_2-C=O), 2.67 (s, 12H, -N-C**H**$_2$-C**H**$_2$-N-), 2.42 ppm (t, *J* = 7.1 Hz, 6H, -N-CH_2-C**H**$_2$-C=O). ^{13}C NMR (151 MHz, $CDCl_3$) δ 173.4 (**C**=O), 55.6 (-N-**C**H_2-**C**H_2-N-), 54.2 (-C(O)O-**C**H_3), 51.6 (-N-**C**H_2-CH_2-C=O), 33.4 (-N-CH_2-**C**H_2-C=O).

2.4.6 Synthesis of 3,3',3''-(1,4,7-triazonane-1,4,7-triyl)tris(N-(2-aminoethyl) propanamide) (D6)

D5 (0.370 g, 0.955 mmol) was dissolved in methanol (5 ml) before adding ethylenediamine (5.8 ml, 84 mmol) to the stirring light yellow solution. The reaction mixture was allowed to stir at room temperature for 5 days in the dark before removing the solvent via rotary evaporator to afford a yellow oil. The oil was further dried on the kugelrogh at 45 °C for 2 hours. The oil was dissolved in methanol and after a week some crystals were observed, isolated and dried for analysis. FT-IR (cm^{-1}) ν(C=O) = 1637 cm^{-1}, ν(N-H stretch) = 3256 cm^{-1}, ν(N-H bend) = 1461 cm^{-1}, ν(C-N) = 1547 cm^{-1}. ^{1}H NMR (600 MHz, d_2o) δ 3.32 (t, *J* = 5.7 Hz, 8H, -N-C**H**$_2$-CH_2-C(O)-O-NH-C**H**$_2$-CH_2-NH_2), 3.08 (t, *J* = 5.7 Hz, 8H, -N-CH_2-C**H**$_2$-C(O)-O-NH-CH_2-C**H**$_2$-NH_2), 2.99 (s, 8H, -N-C**H**$_2$-C**H**$_2$-N-).

2.4.7 Synthesis of 3,3',3'',3'''-(1,4,8,11-tetraazacyclotetradecane-1,4,8,11-tetrayl) tetrapropanenitrile (D7)

Cyclam (0.193 g, 0.963 mmol) was dissolved in methanol (5 ml) before adding acrylonitrile (0.64 ml, 9.6 mmol) to the stirring solution. The reaction mixture was placed in the microwave reactor for 25 minutes at 38 °C controlled temperature with 50 w radiation. The solvent and excess acrylonitrile was removed under reduced pressure. The resulting white precipitate was dissolved in a small amount of warm chloroform before placing the solution in the freezer overnight. The white crystalline precipitate was isolated via filtration and dried under reduced pressure. (**D7**: 0.3298 g, 83 % yield) FT-IR (cm^{-1}) ν_{CN} = 2243 cm^{-1}. ^{1}H NMR (600 MHz, $CDCl_3$) δ 2.75 (t, *J* = 6.7 Hz, 8H, -N-C**H**$_2$-CH_2-CN), 2.62 (s, 8H, -N-C**H**$_2$-C**H**$_2$-N-), 2.57 (t, *J* = 6.7 Hz, 8H, -N-CH_2-C**H**$_2$-CN), 2.44 (t, *J* = 6.7 Hz, 8H, -N-C**H**$_2$-CH_2-C**H**$_2$-N-), 1.63 (p, 4H, -N-CH_2-C**H**$_2$-CH_2-N-). ^{13}C NMR (151 MHz, $CDCl_3$) δ 119.3 (-N-CH_2-CH_2-**C**N), 51.8 (-N-**C**H_2-**C**H_2-N-), 51.4 (-N-**C**H_2-CH_2-CN), 50.3 (-N-**C**H_2-CH_2-**C**H_2-N-), 24.8 (-N-CH_2-**C**H_2-CH_2-N-), 16.5 (-N-CH_2-**C**H_2-CN).

2.4.8 Attempted Synthesis of 3,3',3'',3'''-(1,4,8,11-tetraazacyclotetradecane-1,4,8,11-tetrayl)tetrakis(propan-1-amine) (D8)

To a stirring solution of **D7** (0.6079 g, 1.4737 mmol) in dry toluene (25 ml) small pieces of sodium metal (±10 g) was added and the reaction mixture was stirred under reflux under a nitrogen atmosphere for 20 hours. Thereafter, 50 ml dry ethanol was added during the course of three hours. After an additional 24 hours of stirring under reflux, the solution was allowed to cool to room temperature upon which sodium ethoxide crashed out of solution. Distilled water (30 ml) was added and the mixture was swiftly swirled before separating the organic and aqueous phase via a separating funnel. The organic phase was dried over potassium carbonate, before removing the solvent under reduced pressure to yield a brown oil.

2.4.9 Synthesis of 4,4',4'',4'''-((1,4,8,11-tetraazacyclotetradecane-1,4,8,11-tetrayl)tetrakis (methylene))tetrabenzonitrile (D9)

Cyclam (0.5024 g, 2.5109 mmol) and sodium hydroxide (0.3715 g, 9.2886 mmol) was dissolved in distilled water (80 ml), before adding a solution of 4-bromomethyl benzonitrile (1.9682 g, 10.044 mmol) in chloroform (10 ml). The reaction mixture was vigorously stirred at room temperature for 7 hours. Once completed, the organic phase was separated and dried over $MgSO_4$, before removing the solvent to afford a white precipitate. The precipitate was purified via recrystallization from DCM solution layered with MeOH and placed in the freezer overnight. The resulting precipitate was isolated via filtration and dried under reduced pressure. (**D9**: 1.1895 g 71 % yield). FT-IR (cm^{-1}) ν_{CN} = 2223 cm^{-1}. ^{1}H NMR (600 MHz, $CDCl_3$) δ 7.53 (d, *J* = 8.2 Hz, 8H, Ar-**H**), 7.40 (d, *J* = 8.2 Hz, 8H, Ar-**H**), 3.42 (s, 8H, N-C**H**$_2$-C_6H_4-), 2.57 (s, 8H, -N-C**H**$_2$-C**H**$_2$-N-), 2.46 (t, *J* = 6.9 Hz, 8H, -N-C**H**$_2$-CH_2-C**H**$_2$-N-), 1.74 (m, 4H, -N-CH_2-C**H**$_2$-CH_2-N-). ^{13}C NMR (101 MHz, $CDCl_3$) δ 145.9 (N-CH_2-**Ar**), 132.0 (**Ar**-H), 129.3 (**Ar**-H), 118.9 (Ar-**C**N), 110.8 (**Ar**-CN), 58.8 (N-**C**H_2-C_6H_4-), 51.5 (-N-**C**H_2-**C**H_2-N-), 50.6 (-N-**C**H_2-CH_2-**C**H_2-N-), 24.4 (-N-CH_2-**C**H_2-CH_2-N-).

2.4.10 Attempted Synthesis of (((1,4,8,11-tetraazacyclotetradecane-1,4,8,11-tetrayl)tetrakis (methylene))tetrakis(benzene-4,1-diyl))tetramethanamine D10

To a stirring solution of **D7** (0.6079 g, 1.4751 mmol) in dry toluene (25 ml) small pieces of sodium metal (±10 g) was added and the reaction mixture was stirred at reflux under nitrogen atmosphere for 20 hours. Thereafter, 50 ml dry ethanol was added during the course of three hours. After an additional 24 hours of stirring at reflux the solution was allowed to cool to room temperature upon which sodium ethoxide crashed out of solution. Distilled water (30 ml) was added and the mixture was swiftly swirled before separating the organic and aqueous phase via a separating funnel. The organic phase was dried over potassium carbonate, before removing the solvent under reduced pressure to yield a brown oil.

2.5 References

(1) Buhleier, E.; Wehner, W.; Vogtle, F. *Synthesis.* **1978**, *1978* (2), 155–158.

(2) Tomalia, D. A.; Baker, H.; Dewald, J.; Hall, M.; Kallos, G.; Martin, S.; Roeck, J.; Ryder, J.; Smith, P. *Polym. J.* **1985**, *17* (1), 117–132.

(3) Newkome, G. R.; Yao, Z.; Baker, G. R.; Gupta, V. K. *J. Org. Chem* **1985**, 2003–2004.

(4) Hawker, C. J.; Frechet, J. M. J. *J. Am. Chem. Soc.* **1990**, *112* (21), 7638–7647.

(5) Kesharwani, P.; Jain, K.; Jain, N. K. *Prog. Polym. Sci.* **2014**, *39* (2), 268–307.

(6) Boas, U.; Christensen, J. B.; Heegaard, P. M. H. *J. Mater. Chem.* **2006**, *16* (38), 3785–3798.

(7) Gupta, V.; Nayak, S. *J. Appl. Pharm. Sci.* **2015**, *5* (3), 117–122.

(8) Kaiser, E. T.; Mihara, H.; Laforet, G. A.; Kelly, J. W.; Walters, L.; Findeis, M. A.; Sasaki, T. *Science* **1989**, *243*, 187–192.

(9) van Nostrum, C. F.; Picken, S. J.; Nolte, R. J. M. *Angew. Chem. Int. Ed. Engl.* **1994**, *33* (21), 2173–2175.

(10) Nagasaki, T.; Kimura, O.; Ukon, M.; Arimori, S. *J. Chem. Soc. Perkin Trans.* **1994**, 1–7.

(11) McNaught, A. D.; Wilkinson, A. *IUPAC Compendium of Chemical Terminology*, 2nd ed.; 2014.

(12) Pedersen, C. J. *J. Am. Chem. Soc.* **1967**, *89* (26), 7017–7036.

(13) Martell, A. E.; Hancock, R. D.; Smith, R. M.; Motekaitis, R. J. *Coord. Chem. Rev.* **1996**, *149*, 311–328.

(14) Caminade, A. M.; Wei, Y.; Majoral, J. P. *Comptes Rendus Chim.* **2009**, *12* (1–2), 105–120.

(15) Nagasaki, T.; Ukon, M.; Arimori, S. *J. Chem. Soc.* **1992**, 608–610.

(16) Chow, H.; Leung, C.; Wang, G.; Yang, Y. *C. R. Chim.* **2003**, *6*, 735–745.

(17) Subik, P.; Białońska, A.; Wołowiec, S. *Polyhedron* **2011**, *30* (5), 873–879.

(18) Slazus, E. Dendrimer Encapsulated Gold Nanoparticles as Catalyst Precursors for Oxidative Transformations of Unsaturated Hydrocarbons, M.Sc. thesis Stellenbosch University, 2015.

(19) Ertürk, A. S.; Tülü, M.; Bozdoğan, A. E.; Paralı, T.; Parali, T. *Eur. Polym. J.* **2014**, *52*, 218–226.

(20) Peterson, J.; Allikmaa, V.; Subbi, J.; Pehk, T.; Lopp, M. *Eur. Polym. J.* **2003**, *39*, 33–42.

(21) Peterson, J.; Allikmaa, V.; Lopp, M. *Proc. Est. Acad. Sci. Chem.* **2001**, No. 50, 167–172.

(22) Wainwright, K. P. *J. Chem. Soc. Dalton Transactions* **1980**, *62*, 127–128.

(23) Malgas-Enus, R. The Preparation And Characterization Of Multinuclear Catalysts Based On Novel Dendrimers : Application In The Oligomerization And Polymerization Of Unsaturated Hydrocarbons., Ph.D thesis Stellenbosh University, 2011.

(24) Wainwright, K. P. *J. Chem. Soc. Dalton Transactions* **1983**, 1149–1152.

(25) Jebasingh, B.; Alexander, V. *Synth. Commun.* **2004**, *34* (15), 2843–2848.

(26) Comba, P.; Jurisic, P.; Lampeka, Y. D.; Peters, A.; Prikhod, A. I.; Pritzkow, H. *Inorg. Chim. Acta* **2001**, *324*, 99–107.

(27) Gould, F.; Johnson, G.; Ferris, A. *J. Org. Chem.* **1960**, *25*, 1658–1660.

3 Synthesis and Characterization of Dendritic Cu (II) and Ga (III) complexes

3.1 Introduction

In chapter 3, α–amino phosphonic acids are introduced with special focus on the chemical aspects contributing to their unique properties. It covers the relevant synthetic methods commonly employed to acquire these target ligands and complexes. The attempted modification of generation 1 cyclam-cored poly(amidoamine) PAMAM dendrimer (**D2)** to form a phosphonic acid analogue (**L1**) is described followed by the isolation of multinuclear gallium (III) complex (**C1**). A set of model ligands (**ML1** and **ML2**) as well as a model complex (**MC1**) were synthesized for comparison with the multinuclear derivatives. Commercially available generation 1 diaminobutane poly(propylenimine) DAB-PPI was also modified to obtain the corresponding phosphonic acid analogue (**L2**). In addition, chapter 3 also covers the versatility of Schiff base ligands. The synthesis of a salicylaldimine derivative (**L3**) and the isolation of the corresponding gallium (III) (**C4a** and **C4b**) and copper (II) (**C5**) complexes are reported. These ligands and complexes were selected as prospective multinuclear scaffolds for "cold" analogues of dendritic radiotracers which could potentially be employed for cancer diagnosis.

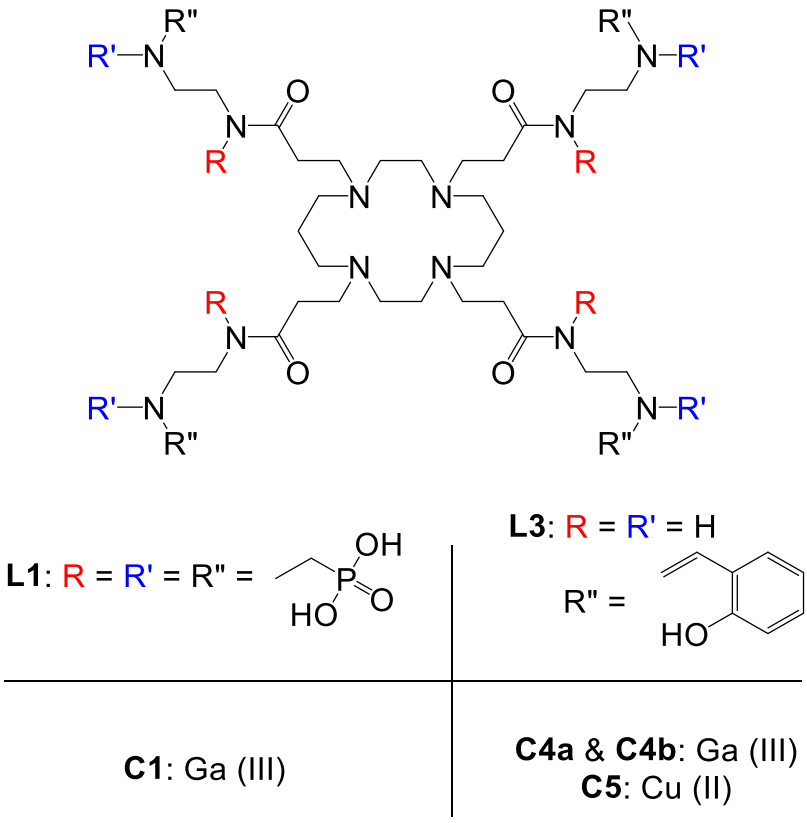

Figure 3.1: General structure of target ligands.

3.2 α–Aminophosphoryl compounds

α–Amino phosphoryl compounds have recently attracted the attention of researchers from a wide array of disciplines. These versatile compounds have proved their worth in several fields as evident from their range of applications (discussed in Chapter 1: Section 1.2.3.1). The impetus to investigate α–amino phosphonic acids (**1**) (depicted in Figure 3.2) stems from the similarities they share with α–amino acids.

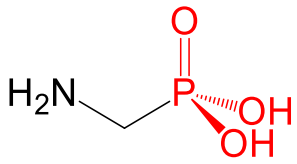

α-Amino phosphonic acid (1)

Figure 3.2: α–Amino phosphonic acids.

Considering that nitrogen and phosphorous are both p-block elements located in the second and third period of group 15, respectively, it is expected that they should behave similarly. However, fundamental differences in their reactivity are observed. The unique electronic configurations of each element determines their size, shape, and acidity[1], all of which are influential in their reactivity.

Phosphorous compounds commonly exist either as trivalent or pentavalent compounds with a range of possible oxidation states (-3 to +5) available, whereas nitrogen can only be regarded as trivalent. The difference in s-d promotional energy of phosphorous (3s → 3d) is less than that of nitrogen (2s → 3d). In other words, the valence electrons of phosphorous occupy higher energy levels in comparison to that of nitrogen. Thus, it is common for phosphorous to access these d orbitals to assist in bonding and facilitate hybridization. Phosphorous often forms multiple bonds between itself and oxygen involving dπ (P) – pπ (O) interactions to form the all-important phosphoryl (P=O) bond.[2] The phosphoryl bond is polarized and the oxygen atom possesses a sterically accessible lone electron pair, however the substituents on the phosphorous atom have the greatest influence on the overall reactivity.

Phosphoric acid (**2**) consists of three P-OH moieties and one phosphoryl (P=O) bond. Alkyl or aryl phosphonic acids (**3**) are considered derivatives of **2** in which case an organic moiety R replaces a hydroxyl moiety. The phosphorous atom is sp^3 hybridized ensuring the PO_3-C moiety adopts a tetrahedral geometry. The two acidic P-OH groups have different pK_a values ($pK_a1 = 0.5 – 3$, $pK_a2 = 5 – 9$).[1] The wide pK_a range of the diprotic acid is due to the extent of electron-withdrawing or electron-donating abilities of the organic

substituent.[3] Phosphonates (**4**) are ester analogues of **2**, in which all three acidic hydroxy moieties are replaced by alkoxy units (OR). With this said, these species require an introduction as they are a common intermediate towards the synthesis of **3** (Figure 3.3).

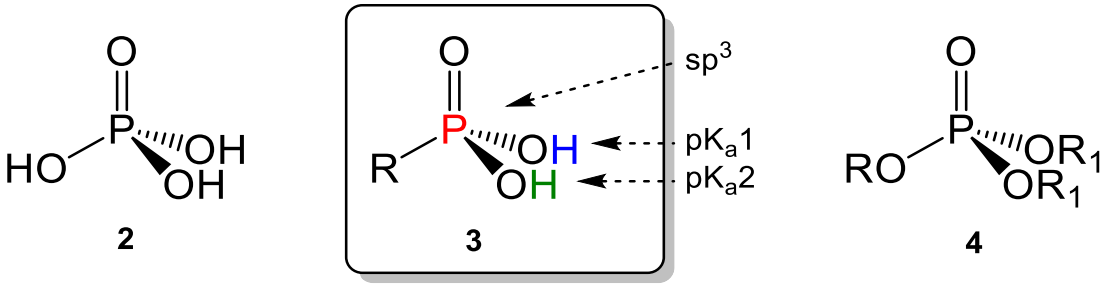

*Figure 3.3: (**2**) Phosphoric acid (**3**) Phosphonic acid (**4**) Phosphonates.*

This following section introduces the chemical relevance of phosphorous compounds and their respective α–aminophosphorous derivatives. The discussion entails a brief overview of various synthetic methods, reaction parameters and purification techniques commonly encountered, with special focus given to the Irani-Moedrizner and Pudovik reactions.

3.3 Typical synthetic routes to α–Aminophosphoryl compounds

Developing a synthetic procedure that affords α–aminophosphonic acid that contain the valuable N-C-P fragment, has been under the spotlight due to their intriguing biological potential. Various avenues have been explored and several review articles showcase the synthetic advancement achieved over the years.[4]

3.3.1 Michaelis – Arbuzov Rearrangement

The most direct route to form a C-P bond is known as the Michaelis–Arbuzov Rearrangement (Figure 3.4) which was first reported by Michaelis[5], and has been thoroughly investigated by Arbuzov.[6,7] The simplest example of this well-known method entails a nucleophilic trialkyl phosphite (**5**) reacting in a S_N2 fashion with an halide (**6**) via an alkoxy phosphonium salt intermediate (**7**) to yield dialkyl alkyl phosphonate (**8**) and the resultant alkyl halide (**9**). The reaction tends to require heating under reflux.

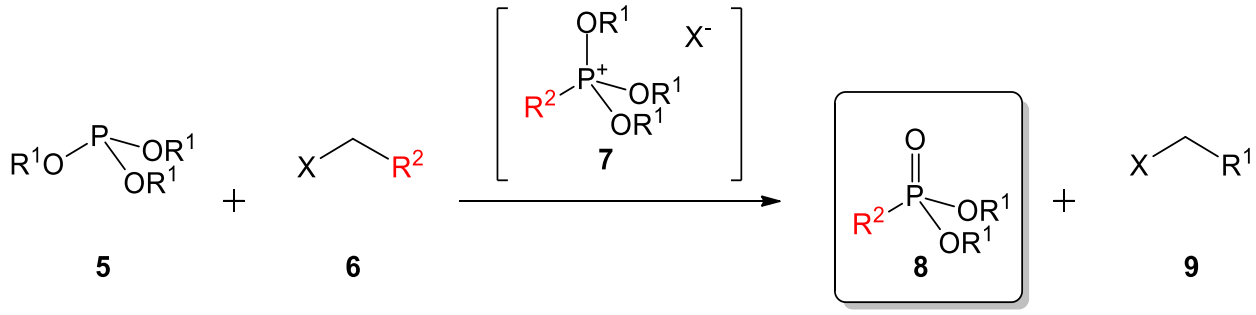

Figure 3.4: Michaelis – Arbuzov Rearrangement.

3.3.2 Michaelis–Becker reaction

Alternatively, the Michaelis–Becker reaction (Figure 3.5) requires less stringent reaction temperatures as compared to the Michaelis–Arbuzov reaction. The reaction involves the nucleophilic substitution between a phosphorous component (**10**), which when treated with a base exists as **11**, and a haloalkane (**7**) to yield phosphinates/phosphonates (**12**). The ambident nature of the nucleophile, coupled with the basicity of the salt, makes it susceptible to side reactions.

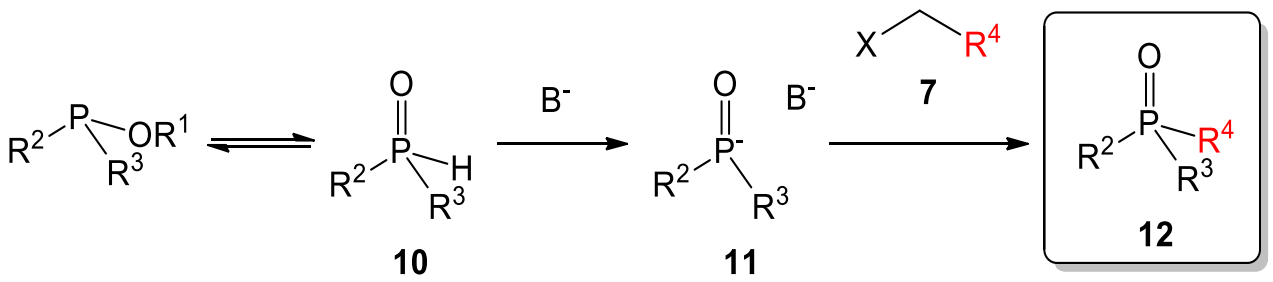

*Figure 3.5: Michaelis–Becker reaction (**10** and **11**: R^2/R^3 = alkyl, **12:** Phosphinates: R^2/R^3 = alkyl derivative; Phosphonates: R^2/R^3 = alkoxy derivative).*

3.3.3 Kabachnik-Fields reaction

Alternatively, phosphonates can be obtained by means of a Mannich-type condensation reaction (Figure 3.6). However, preceding work done by Abramov and Pudovik is worth mentioning first. Abramov[8] was able to synthesize α-hydroxy phosphonates (**18**) through the addition of dialkyl phosphite (**15**) to a carbonyl moiety (**13**). Two years later, Pudovik[9] synthesized α-amino phosphates (**16**) by reacting the substrate containing a P-H bond with the carbon of an imine moiety. The Kabachnik-Fields reaction, a phospha-Mannich type variation, was independently discovered by Kabachnik and Medved[10] and Fields.[11] The one-pot, three component reaction involves aldehydes or ketones[12] as the carbonyl compound (**13**), an amine (**14**) and a dialkyl phosphite (**15**) as the activated substrate. The exact mechanism for the Kabachnik-Fields reaction is still under dispute. Two possible pathways have been proposed[13]; the "imine route" and the "α–hydroxy phosphonate route",

which has been named according to the intermediates which are formed. The preferred pathway seems to depend on the nature of the substrates.[14,15] During the reaction, the soft nucleophile **15** and the hard nucleophile **14** compete for the electrophilic carbonyl compound **13**. The first pathway (imine route) involves the Schiff base reaction between **13** and **14** followed by the addition of the crucial activated substrate **15** to the imine **17** via a Pudovik-type reaction to yield an α-amino phosphonate species (**16**). This route is usually favoured by a hard carbonyl compound and dependent on the basicity of the amine.[16] This is contradictory to the hydroxy phosphonate route which involves the addition of the activated species **15** to the carbonyl compound **13**. This results in the formation of hydroxy phosphonate **18** which subsequently undergoes direct nucleophilic substitution with **14** to afford the α-amino phosphonate species **16**. In this case, a softer carbonyl compound is preferred.[16]

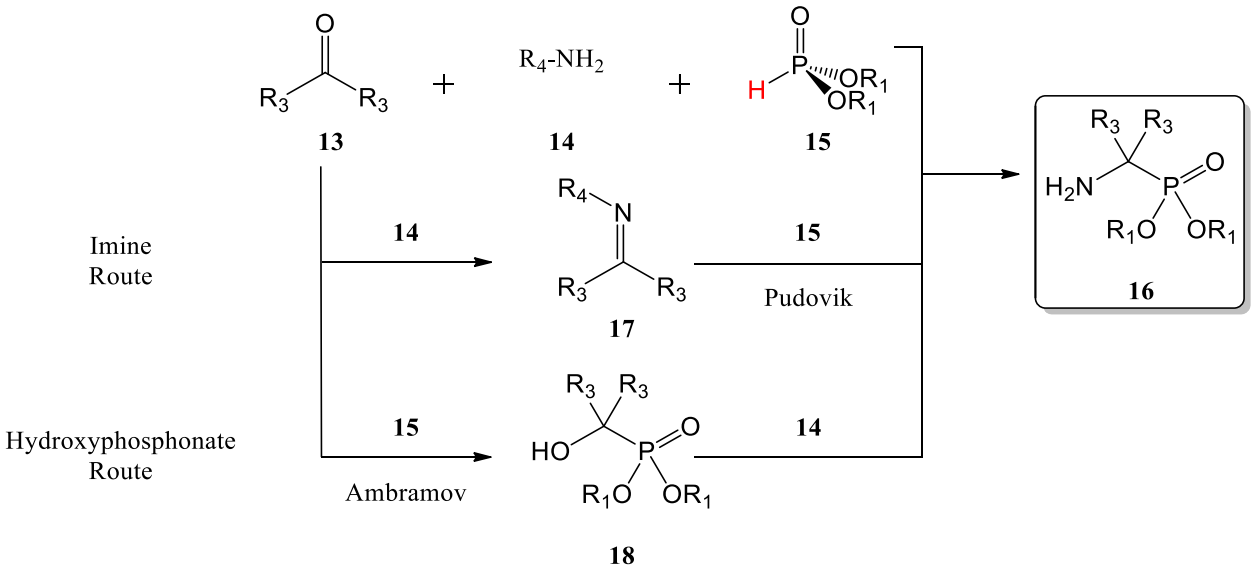

Figure 3.6: Kabachnik-Fields Reaction.

3.3.4 Irani-Moedritzer reaction

A particular case of the Kabachnik-Fields reaction, known as the Irani-Moedritzer reaction, (Figure 3.7), specifically utilizes phosphorous acid (**20**) and formaldehyde (**21**) in combination with the desired amines (**19**) to yield α-amino phosphonic acids (**22**). The synthetic procedure which K. Moedritzer and R. R. Irani[17] employed, provides a method to yield phosphonic acids directly avoiding the additional hydrolysis step required during the Kabachnik-Fields reaction. The Irani-Moedritzer reaction only succeeds in an acidic medium with formaldehyde as the carbonyl compound. The low pH increases the reaction rate, improves yields and limits the oxidation of phosphites to phosphates. [17]

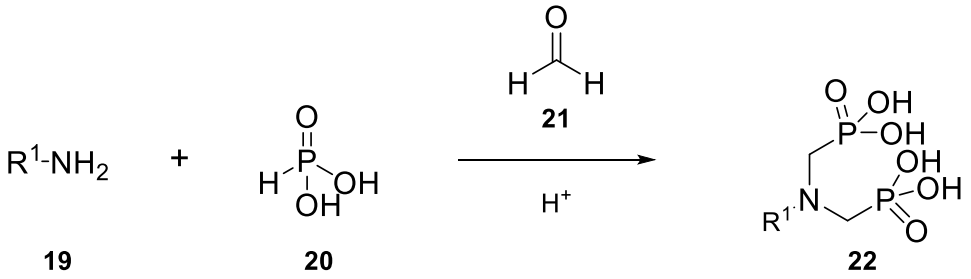

Figure 3.7: Irani-Moedritzer reaction.

3.4 Results and discussion

The Irani-Moedritzer reaction was considered as a viable method to modify the cyclam-cored PAMAM dendritic scaffold (**D2**, reported in Chapter 2) to its corresponding phosphonic acid derivative. Turrin and co-workers[18] showed that the Irani-Moedritzer procedure could successfully modify amino terminated poly(ethylene glycol) (PEG) ranging from 750 – 5000 g.mol^{-1} in one step to the corresponding bis(phosphonomethyl)amino analogues (Figure 3.8a). More recently, Lui and co-workers[19] investigated the dispersion properties of a series of bis(phosphonic acid)amino-terminated polymers which they were able to synthesize via the Irani-Moedritzer reaction (Figure 3.8b).

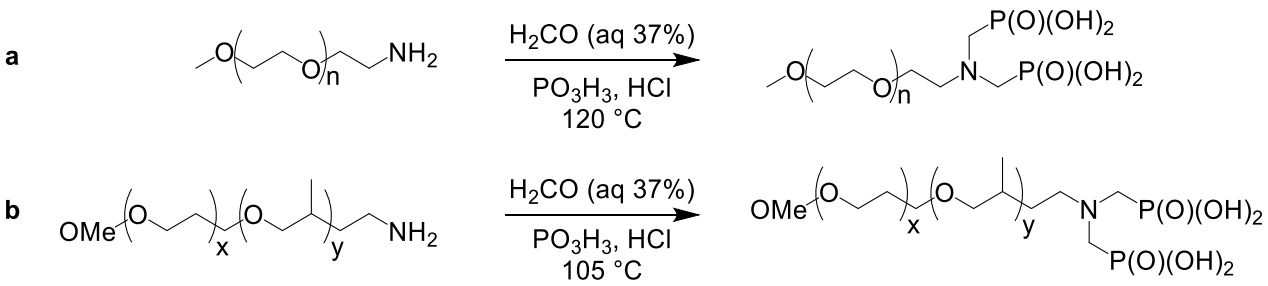

Figure 3.8:(a) bis(phosphonomethyl)amino-terminated poly(ethylene glycol)[18]*,*

(b) bis(phosphonic acid)amino-terminated polymers.[19]

The research by Zeevaart *et al.*[20] details the synthesis of a water-soluble polymer functionalized with methylene phosphonate groups (PEI-MP) which indicates that the Irani-Moedritzer procedure allows for the transformation of secondary and primary amines.

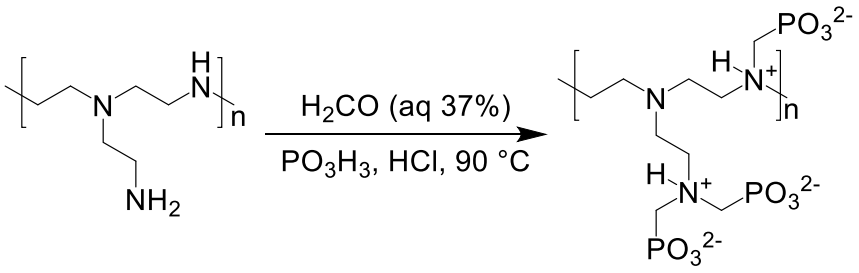

Figure 3.9: Water-soluble polymer functionalized with methylene phosphonate groups (PEI-MP). [20]

Drawing inspiration from their method, we set out to functionalize the cyclam-cored PAMAM dendrimer **D2** to produce a phosphonic acid modified dendrimer **L1**. This was attempted using a direct approach via the Irani-Moedritzer method.

3.4.1 Synthesis and characterization of phosphonic acid modified Cyclam cored PAMAM (L1) and the subsequent multinuclear Ga (III) complex (C1)

The strategy employed to functionalize the dendritic scaffold **D2** to a multifunctional ligand **L1** was done according to a modified procedure first described by Irani-Moedritzer[17] (Reaction Scheme 3.1). The reaction was attempted under various experimental conditions, varying temperature, time and reagent ratios in order to establish the optimum conditions. It is known that in acidic media (pH < 4) the reactive phosphonic acid species suppress the side reactions that can occur, such as N-methylation of free amino groups.[21] The mol ratios of reagents were determined based on the prediction that both primary amine and secondary amine sites could possibly react, as it has been shown that secondary amines are normally more reactive than primary amines in the Irani-Moedritzer reaction.[17] However, with the correct molar ratios, Li *et al.*[22] describe the modification of only the peripheral primary amines to produce the ethylenediamine cored, octamethylenephosphonic acid terminated PAMAM dendrimers. Sherry[23] studied the effect of temperature, the molar ratios of the reactants, total volume of the reaction mixture, acidity, addition time of paraformaldehyde, and total reaction time as well as the order of addition during the synthesis of 1, 4, 7, 10-tetraazacyclododecane-1, 4, 7, 10-tetrakis(methylene phosphonic acid) (DOTP). The findings concluded that no more than 50 % excess paraformaldehyde and 100 % phosphorous acid were needed. The optimal time for addition of paraformaldehyde was 1 hour and the optimal reflux time following the complete addition of paraformaldehyde was also 1 hour.

Accordingly, in our case 15 mol equivalents of phosphorous acid were added to a stirring solution of dendrimer **D2**, before adding 18 mol equivalents of formaldehyde under acidic conditions. The reaction was stirred at 90 – 110 °C under a nitrogen atmosphere for a total of 4 hours. The crude product was isolated after removal of the solvent. The yellow oil obtained was found to be water-soluble and only partially soluble in polar organic solvents. Several purification methods were attempted such as recrystallization, acid-base extraction, lyophilization (freeze drying), and isolation of the salt adduct; however, isolation was hindered by

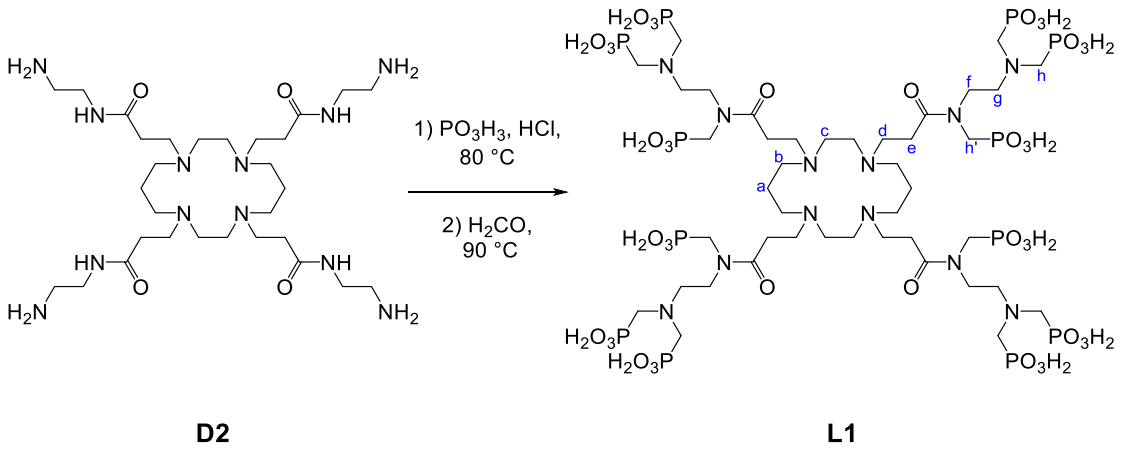

*Reaction Scheme 3.1: Synthesis of **L1**.*

the lack of solubility that **L1** exhibited in organic solvents. Alternatively, compounds with sufficiently high molecular weights could also be purified via dialysis, size exclusion chromatography (SEC) and high-performance liquid chromatography (HPLC).[24] The best purification strategy was found when a saturated solution of the crude product in water, was decanted into cold ethanol while vigorously stirring the solution. A white precipitate immediately crashed out of solution. The white precipitate was isolated via filtration under nitrogen. The precipitate was hygroscopic in nature and without a nitrogen atmosphere the precipitate quickly becomes an undesirable sticky substance.

The FT-IR spectrum of **L1** showed the expected $\nu_{P=O}$ absorbance at 1168 cm^{-1} and the $\nu_{P\text{-}O\text{-}H}$ stretch, which appears as two peaks at 918 and 1034 cm^{-1}. The $\nu_{P\text{-}O\text{-}H}$ stretch was also observed at 3354 cm^{-1}. The bands observed at 1720 cm^{-1} can be assigned to the amide $\nu_{C=O}$ stretch with some evidence of $\nu_{N\text{-}H}$ stretch between 3400 – 3200 cm^{-1}. The ^{1}H NMR spectrum of **L1** displayed the acidic protons (P-OH) as two singlets in the expected region between 6 – 8 ppm and a distinct doublet at 3.37 ppm corresponding to the resonances for the methylene protons on the carbon connecting the phosphorous and nitrogen (***h*** in Reaction Scheme 3.1). The N-C**H**$_2$-P resonance exhibited $^{2}J_{P,H}$ = 14 Hz coupling which is common for these compounds.[25] Although these

results indicate the formation of the N-C-P bond, the resonances originating from the dendrimer showed extensive overlap of broad undefined peaks in the range of 1 – 4 ppm. The protons of the macrocyclic moiety represented by ***a*** in Reaction Scheme 3.1 appear as a broad peak at 1.29 ppm. Two other regions around 3.58 and 3.18 ppm seem to be a combination of protons ***d***/***f*** and ***e***/***g***, respectively. Several smaller peaks are observed, but could not be identified which may indicate a product mixture or an impure product. The ^{13}C NMR spectrum of **L1** indicated several peaks in the region of 173 ppm where a single peak representing the amide carbon is expected. This may indicate that not all internal NH groups are phosphorylated. Also, multiple peaks appear between 55 – 30 ppm which could not be assigned unambiguously. The peak at 49.45 ppm was assigned to the methylene carbon (***h*** in Reaction Scheme 3.1) connecting the phosphorous and nitrogen. Further characterization via ^{31}P NMR is expected to show two singlets, one for internal and one for peripheral phosphorous environments in the region of 8 ppm. However, there were several peaks in the range of 0.5 - 20.00 ppm. Three peaks at 8.84, 7.27 and 3.36 ppm were assigned to the two different phosphorous environments and the starting material, respectively.

Further characterization of **L1** included elemental analysis. The results obtained from the elemental analysis indicated that the experimental values (N, 11.33; C, 25.45; H, 7.09 %) did not correlate with the calculated values (N, 9.42; C, 28.26; H, 5.65 %). However, the hygroscopic nature of these dendritic ligands has a propensity to trap solvent molecules and with the addition of several water molecules both the calculated values for carbon and hydrogen started to correlate with the experimental results. The calculated nitrogen value could not be lowered by the addition of any solvent or reagent used during the experiment. The calculated % value of nitrogen could only be lowered if some of the internal NH groups were not phosphorylated. Thus, from elemental analysis it seems there is a mixture of products (i.e. mixture of complete and partially phosphorylated dendrimer) as well as some encapsulated solvent molecules.

Additionally, **L1** was analysed by electrospray ionization mass spectrometry (ESI-MS). This technique provides soft ionization which allows for the preferential detection of multiply charged species rather than fragmentations, although such fragmentations are not entirely absent. The number of basic sites on the molecule usually refers to the number of possible charged species that can form. Therefore, the peak assigned to the singly charged parent ion is often absent for macro-molecules, instead various multiply-charged molecular ions or some adducts thereof are observed. As a result, the analysis of ESI-MS can be complex for

large molecules, especially in the range 200 m/z – 1000 m/z and although to a lesser extent, it is common to encounter several complex fragmentation patterns. In the positive mode ESI MS spectrum of **L1**, the peaks observed at m/z ratio of 489.29, 511.25 (base peak) and 533.21 corresponds to the triply charged molecular ion that lost four PO_3H_2 fragments $[C_{42}H_{94}N_{12}O_{28}P_8]^{3+}$ and their sodium adducts $[C_{42}H_{94}N_{12}O_{28}P_8 + Na]^{3+}$ and $[C_{42}H_{94}N_{12}O_{28}P_8 + 2Na]^{3+}$, respectively. The base peak appeared at m/z ratio of 355.02 and was assigned to the potassium adduct of one pendent arm with the additional loss of a PO_3H_2 fragment $[C_8H_{18}N_2O_7P_2 + K - H]^-$.

The isolation, purification and characterization of the dendritic ligand proved to be challenging due to the hygroscopic nature and solubility properties of the crude product. The characterization indicated that **L1** had been synthesized, but suggest that several impurities were still present after various purification steps. The material isolated was most likely a mixture of products as the reagents were removed during the work-up procedure. Being unable to obtain a pure ligand, the crude material was directly employed in a complexation reaction with gallium chloride with the aim of isolating the multinuclear complex **C1** from the reaction mixture.

Gallium (III) is regarded as a small, highly charged (i.e. hard) metal ion and exhibit properties closely related to iron (III). In literature, there are copious examples of gallium-macrocyclic complexes especially those based on 1,4,7,10-tetraazacyclododecane (Cyclen) and 1,4,7-triazacyclononane (TACN). These show high thermodynamic stability and kinetic inertness. The latter, TACN derivatives, are more suitable chelators as the size of the coordination cavity corresponds better to the size of Ga (III) resulting in a near perfect octahedral coordination sphere.[26] TACN derivatives show a slower rate of complex formation compared to open-chain ligands due to a higher activation barrier, but open-chain ligands on the other hand show a lower degree of kinetic stability.[27]

According to our knowledge, no literature has been reported on the complex **C1**, which has four PAMAM branches each containing three phosphonic acid chelators. Thus, **L1** with a total of 12 phosphonic moieties was reacted with 18 mol equivalents of gallium trichloride in an attempt to isolate the multinuclear complex. The crude (**L1**) was suspended in warm ethanol before adding the metal salt. The reaction mixture was stirred at reflux for 24 hours before decanting the warm solution into a cold diethyl ether solution. The resulting white precipitate was isolated via filtration, rinsed with cold diethyl ether and dried to yield **C1** (Reaction Scheme 3.2).

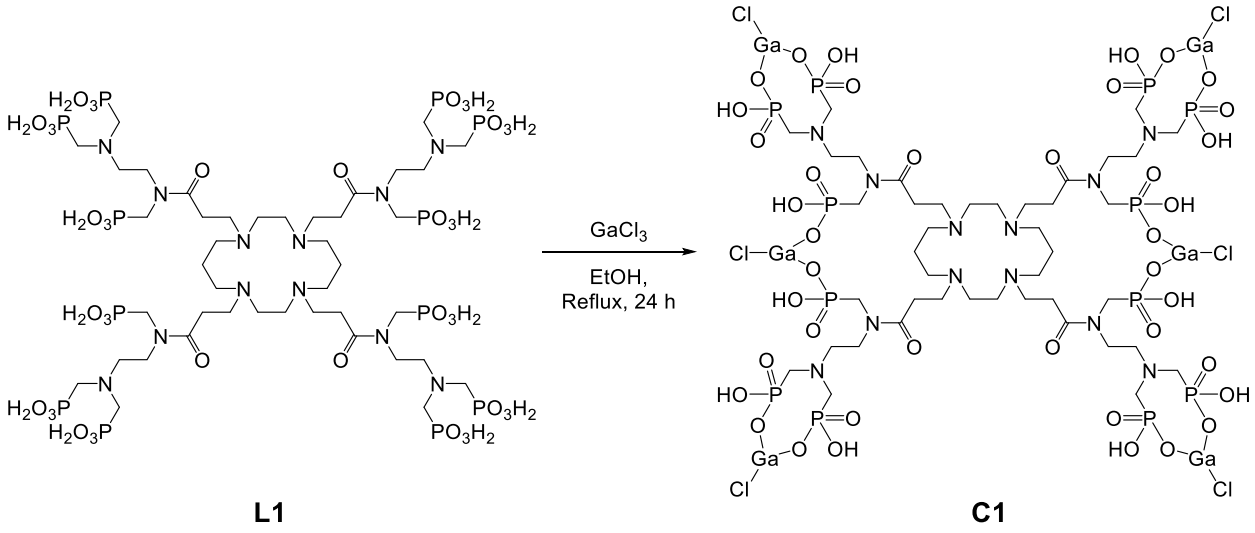

*Reaction Scheme 3.2: Synthesis of **C1**.*

After complexation, the FT-IR spectrum of **C1** showed a shift in the $\nu_{P=O}$ stretch to higher wavenumbers from 1168 cm^{-1} (**L1**) to 1201 cm^{-1} (**C1**). Another indication of complexation can be seen when monitoring the $\nu_{P\text{-}O\text{-}H}$ stretch, which appears as two absorptions at 918 and 1034 cm^{-1} for **L1** but coalesced into one peak at 1007 cm^{-1} for **C1**. The two bands seen for **L1** are due to the $\nu_{P\text{-}O\text{-}H}$(symmetric) and $\nu_{P\text{-}O\text{-}H}$(asymmetric) stretches, which after complexation through one of the P-O bonds, appear as a single band in the spectrum of **C1**. The $\nu_{P\text{-}O\text{-}H}$ stretch also displayed a shift to higher wavenumbers from 3236 cm^{-1} (**L1**) to 3554cm^{-1} (**C1**). The amide $\nu_{C=O}$ stretch shifted slightly lower to 1719 cm^{-1} after complexation.[28] Further characterization by ^{1}H NMR displayed the acidic protons (P-O**H**) resonating as singlets in the range of 6 – 8 ppm as expected and the methylene protons on the carbon connecting the phosphorous and nitrogen (N-C**H**$_2$-P) appeared downfield relative to **L1** at 3.6 ppm with $^{2}J_{P,H}$ = 12 Hz coupling. The spectra showed several peaks in the range of 1 - 4 ppm; however, no definitive assignment was possible due to broad peaks overlapping extensively. The ^{31}P NMR spectrum showed a broad peak at 4.41 ppm, which could be assigned to the phosphorous acid reagent. The region of interest between 10 -7 ppm shows 5 peaks which seems like two broad triplets overlapping. These are assigned to the two different phosphorous environments. There also appears a broad peak at 17.92 ppm, which could possibly be evidence that some arms are uncoordinated.

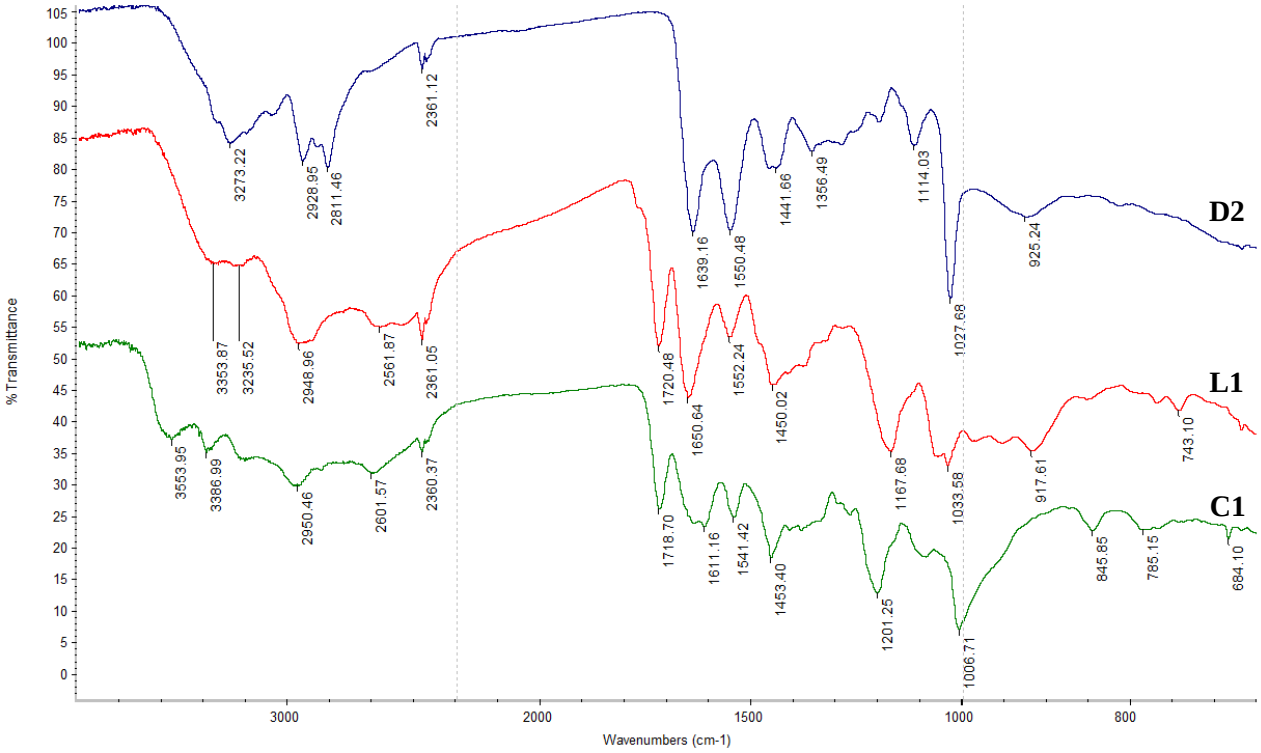

*Figure 3.10: FT-IR of Dendrimer (**D2** – Blue), Phosphonic acid derivative (**L1** – Red), Gallium complex (**C1** – Green).*

Further characterization of **C1** included elemental analysis and electrospray ionization mass spectrometry (ESI-MS). The results obtained from the elemental analysis indicated that the experimental values (N, 7.18; C, 21.00; H, 5.38 %) corresponded well with the calculated values (N, 6.99; C, 20.98; H, 3.69 %). The difference in the hydrogen could not be accounted for, even with the inclusion of various solvent molecules which the hygroscopic product was expected to encapsulate within the dendrimer matrix.

Electrospray ionization mass spectrometry (ESI-MS) was again used to analyse **C1**. In the positive mode ESI MS spectrum of **C1** the peaks observed at m/z ratio of 511.25 (base peak) and 533.21 originates from **L1** and was discussed above. The peak observed at m/z ratio of 357.04 corresponds to the fragment depicted in Figure 3.11.

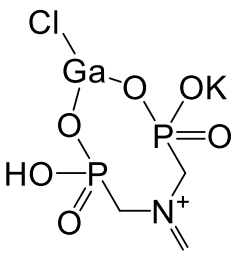

Chemical Formula: $C_3H_7ClGaKNO_6P_2^+$
Exact Mass: 357.83

*Figure 3.11: Positive mode ESI MS fragment of **C1.***

3.4.2 Synthesis and characterization of phosphonic acid model ligands and complexes

A set of model ligands (**ML1** and **ML2**) and complexes (**MC1** and **MC2**) was synthesized to compare the mono- and bi- nuclear variations of the multinuclear dendritic ligand **L1** and complex **C1.** These model ligands and complexes also provided some insight to the behavior of the molecule under the standard reaction conditions employed for **L1** and **C1**.

3.4.2.1 Synthesis and characterization of model ligand 2 (ML2)

The first two reaction steps towards **ML2** (Reaction Scheme 3.3) were based on the synthetic method followed to obtain **D2**. The microwave-assisted Michael addition produced mono- and disubstituted products and had to be purified via silica gel chromatography (DCM: MeOH 9:1) to yield dimethyl 3,3'-(propylazanediyl)dipropanoate **ML2a** as a clear oil (3.049 g, 74 % yield). G. Bosica *et al.*[29] also observed the formation of a mixture of products and concluded that the reactivity of the Michael donors depends on its electronic nature i.e. the length of the alkane chain bonded to the nitrogen and also the nature of the amine (primary/ secondary). This essentially indicated that the propyl amine has less electron density than the PAMAM branch, because only the formation of bis substituted was seen during the synthesis of **D2**, as described in Chapter 2. Amidation of **ML2a** yielded 3,3'-(propylazanediyl)bis(N-(2-aminoethyl)propanamide) **ML2b** in high yield (3.012 g, 79 % yield) as a clear oil. The final step was the modification of **ML2b** via the Irani-Moedritzer reaction in an attempt to isolate **ML2**. The latter was chosen as a representation of two of the PAMAM branches as a di-nuclear analogue. The reaction conditions were the same as described for **L1** and **ML2** was isolated as a yellow viscous solid (0.421 g, 77 % yield).

The reaction was followed via FT-IR (Figure 3.12) and ^{1}H NMR. **ML2a** displayed an absorption at 1732 cm^{-1} corresponding to $\nu_{C=O}$ stretch of the ester moieties which shifted to lower wavenumbers in **ML2b** to 1636 cm^{-1} now corresponding to the $\nu_{C=O}$ stretch of the amide moiety. Upon phosphorylation, the spectrum of **ML2** displayed broad peaks corresponding to the $\nu_{P=O}$ stretch and ν_{P-O-H} stretch at 1142 and 911 cm^{-1}, respectively. The $\nu_{C=O}$ stretch shifted to higher wavenumbers from 1636 to 1710 cm^{-1}. The large shift to higher wavenumbers was also observed for **L1**, and was thought to be due to the electron withdrawing moiety added to the amide nitrogen.

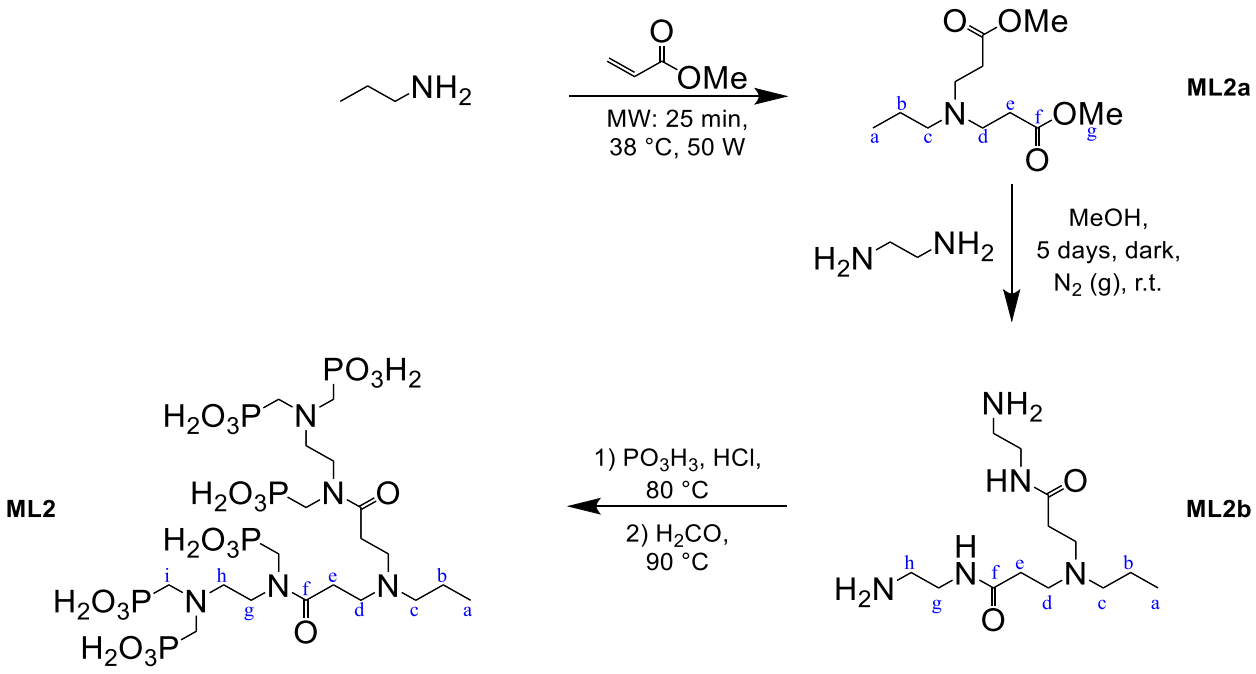

*Reaction Scheme 3.3: Synthesis of **ML2.***

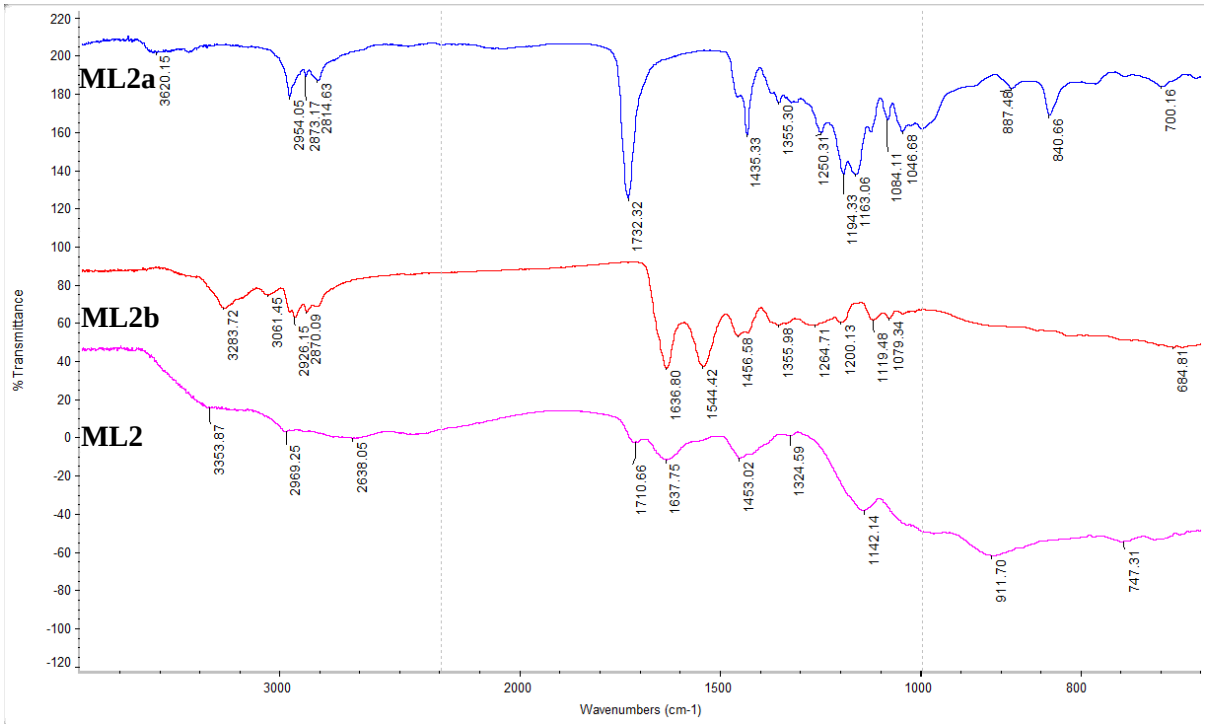

*Figure 3.12: FT-IR of **ML2a** – Blue; **ML2b** – Red; **ML2** – Purple.*

In the ^{1}H NMR spectrum of **ML2a** the methoxy protons (***g*** in Reaction Scheme 3.3) resonated as a singlet at 3.63 ppm integrating to a total of 6 protons. This peak disappeared upon amidation as evident from the spectrum obtained for **ML2b**. For **ML2b** the methylene protons (***g*** in Reaction Scheme 3.3) adjacent to the amide nitrogen resonated as a triplet at 3.24 ppm with $^{3}J_{H,H}$ = 6.3 Hz coupling and integrating for a total of 4

protons. The spectrum of **ML2** showed evidence of the acidic protons (P-OH) between 6 – 8 ppm and several overlapping peaks in the region of 2.5 – 4.0 ppm. The doublet appearing at 3.57 ppm was assigned to the methylene protons on the carbon connecting the phosphorous and nitrogen (N-C**H**$_2$-P). The ^{13}C NMR of **ML2a** showed the methoxy carbon (***g*** in Reaction Scheme 3.3) resonating at 49.29 ppm and the carbonyl carbon (***f*** in Reaction Scheme 3.3) at 172.96 ppm. The subsequent amidation had no significant effect on the carbonyl chemical shift as it appeared at 172.86 ppm for **ML2b**. However, the absence of the methoxy carbon and the appearance of two new peaks at 41.45 and 42.01 ppm corresponding to the carbons ***g*** and ***h*** in Reaction Scheme 3.3 indicated that the amidation was successful. It should be noted that the spectra of **ML2b** had several small peaks in the range of 22.00 – 54.00 ppm.

The results indicate that the phosphorylation was successful, however, separation of the product from the reaction mixture was not achieved. The cause of this reaction mixture was thought to be from several sources. During the amidation reaction some remaining ethylenediamine (EDA) could also undergo phosphorylation and both the products of EDA and **ML2b** could yield incomplete amine sites. During the phosphorylation reaction, it was suspected that under the harsh reaction conditions, the amide moiety hydrolyzed, contributing to the mixture of possible products (Figure 3.13).

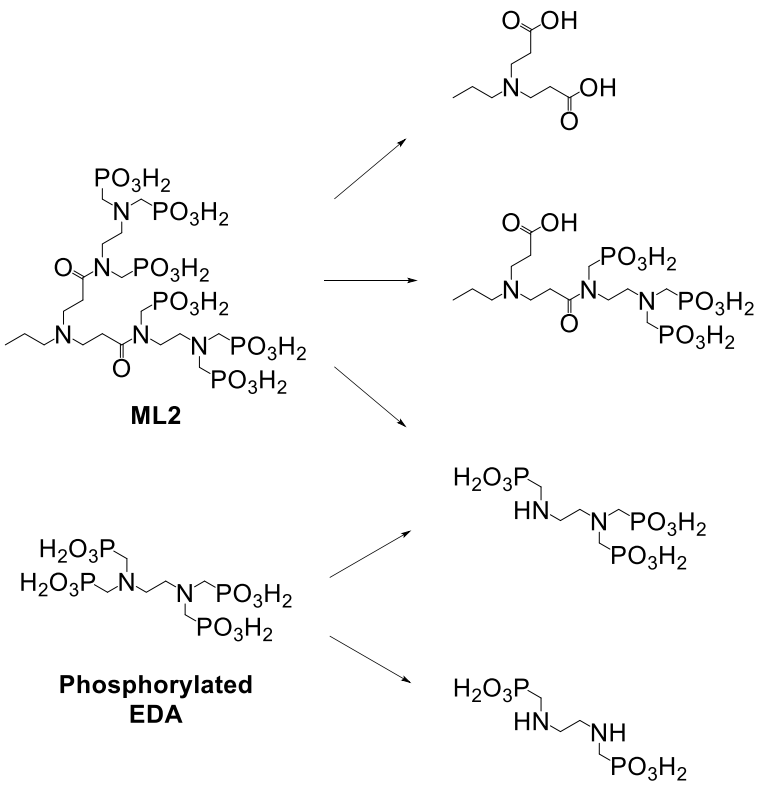

Figure 3.13: Possible hydrolysis products.

A quick test was done by boiling **D2** in acidic water and it was found that within 2 hours hydrolysis occurred[30] as evident from $\nu_{C=O}$ absorption of the carboxylic acid carbonyl at around 1700 cm^{-1} monitored via FT-IR spectroscopy. The goal was to separate the fractions formed during the synthesis of **ML2**, but unfortunately the separation, as with **L1**, was not successful after several attempts.

3.4.2.2 Synthesis and characterization of model ligand 1 (ML1) and model complex 1 (MC1)

The monodentate derivative (**ML1)** was chosen to represent the tertiary amine fractions of **L1** and was prepared following a method reported by Gholivand and co-workers.[31] Propyl amine was transformed to ((propylazanediyl)bis(methylene))diphosphonic acid (**ML1**) via a Irani-Moedritzer reaction to yield a clear oil which was further purified by crystallization from methanol. The precipitate was isolated as a white solid under nitrogen in moderate to high yields (80 %). Thereafter, gallium trichloride was added to a stirring suspension of **ML1** in dry methanol. Upon addition, the milky white solution immediately became clear pink, gradually changing to purple after 1 hour. The reaction mixture was stirred for an additional 12 hours during which the solution became milky white. After work-up, **MC1** was isolated as a white air-stable powder (75 % yield). The complete reaction scheme is represented in Reaction Scheme 3.4.

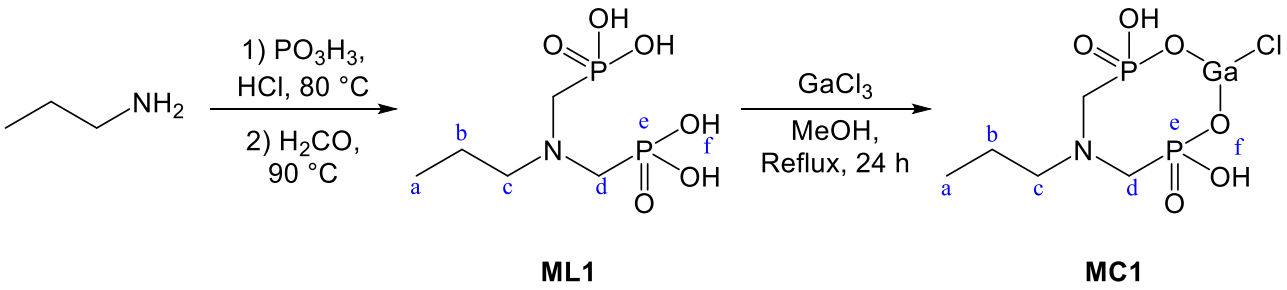

*Reaction Scheme 3.4: Synthesis of **MC1**.*

In the FT-IR spectra (Table 3.11) of the **ML1**, the absorption observed at 1133 cm^{-1} represents the $\nu_{P=O}$ stretch. Further characterization by ^{1}H NMR of **ML1** (Figure 3.14a), showed the methylene protons (***d*** in Reaction Scheme 3.4) resonating at 3.45 ppm as a doublet due to $^{2}J_{H-P}$ = 12.8 Hz coupling. The resonance corresponding to the protons represented by ***c*** in Reaction Scheme 3.4 deviates from its expected triplet, and can be observed as a multiplet at 3.32 ppm due to $^{4}J_{H,P}$ coupling. The ^{13}C NMR spectrum of **ML1** (Figure 3.14b) depicts the methylene carbon (***d***) resonating at 51.67 ppm as a doublet of doublets due to $^{1}J_{C-P}$ = 137.8 Hz and $^{2}J_{H-P}$ = 4.4 Hz coupling. The resonance corresponding to ***c*** can be seen as a triplet at 59.02 ppm due to

$^{3}J_{C\text{-}P}$ = 3.8 Hz coupling. The ^{31}P NMR (Figure 3.14c) displayed a singlet at 8.85 ppm, which differs from that of the starting material at 5.42 ppm. The elemental analysis results of **ML1** indicated that the compound consisted of N, 5.67; C, 24.30 and H, 6.12 %. These results correspond to the calculated value for $C_5H_{15}NO_6P_2$ which are N, 7.29; C, 22.63 and H, 6.64 % with the addition of a single water molecule. However, the difference for nitrogen increases which may possibly be due to the nitrogen standard used during calibration. There are no compounds/reagents used during the reaction or work-up procedure that can account for the difference in nitrogen. The ESI MS(-) spectra of **ML1** showed a base peak at 246 m/z which corresponds to the molecular ion without a hydrogen $[M - H]^-$.

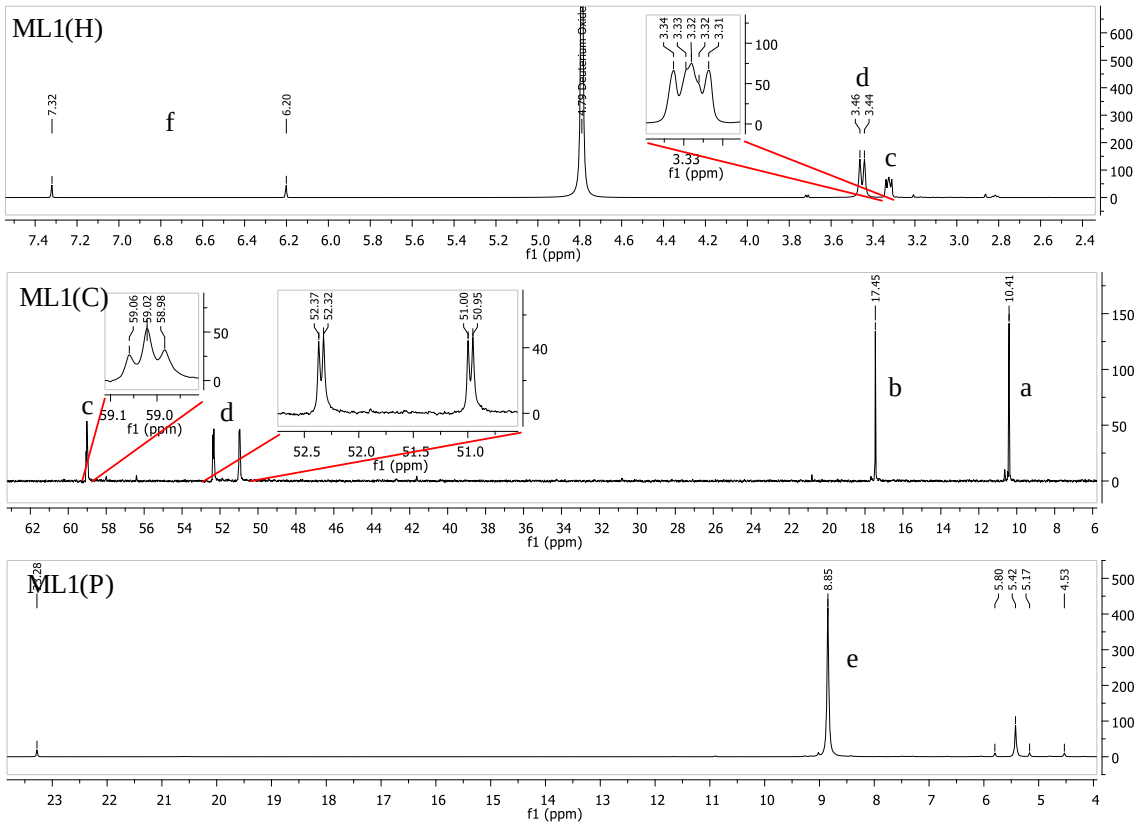

*Figure 3.14: NMR spectra of **ML1**: **a)** ^{1}H NMR; b) ^{13}C NMR; c) ^{31}P NMR.*

Upon complexation, the FT-IR of **MC1** depicted the $\nu_{P=O}$ stretch at 1120 cm^{-1}. The NMR spectrum of **MC1** showed relatively undefined peaks compared to **ML1**. The ^{1}H NMR spectra showed the methylene protons (***d*** in Reaction Scheme 3.4) shifted downfield to 3.79 ppm and the ^{31}P NMR show a multiplet in the range of 8.23 – 8.10 ppm. These results could not unambiguously confirm the successful synthesis of **MC1**, but suggests that there was a mixture of products, most likely a mixture of **ML1** and **MC1**. Thus, **MC1** was

subjected to elemental analysis and the experimental values obtained (N, 5.73; C, 18.82; H, 5.27 %) corresponded to the calculated value for $C_5H_{13}NO_6P_2GaCl$ (N, 4.00; C, 17.14; H, 3.74 %) with the inclusion of 2 molecules of **ML1** and 6 molecules water. The ESI MS(-) spectra of **MC1** showed a base peak at 246 m/z which corresponds to the molecular ion of **ML1** without a hydrogen $[M - H]^-$.

3.4.3 Synthesis and characterization of DAB-PPI ligand (L2)

Commercially available G1 PPI dendrimer was also modified with phosphonic acid to produce the dendritic derivative phosphonic acid modified G1 PPI dendrimer, **L2**. Once completed, the yellow reaction mixture was transferred to cold ethanol upon which a white precipitate formed. The precipitate was isolated under nitrogen and freeze dried to obtain **L2** as a sticky yellow solid (76 % yield).

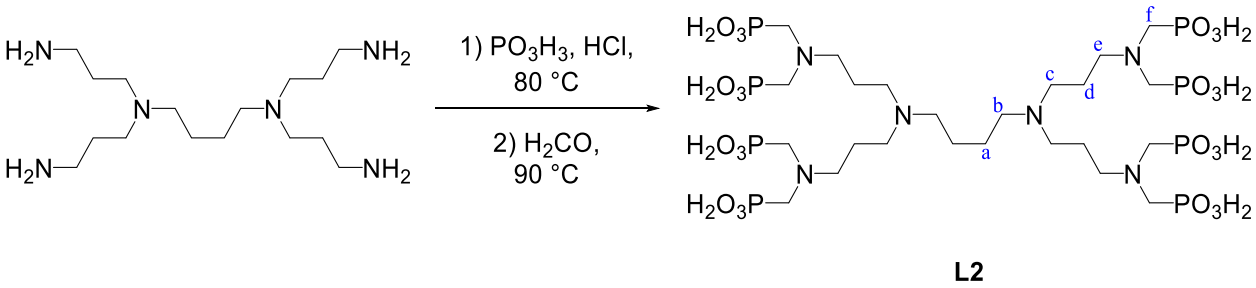

*Reaction Scheme 3.5: Synthesis of **L2**.*

In the FT-IR spectra (Table 3.1) of **L2**, the absorption observed at 1150 cm^{-1} represents the $\nu_{P=O}$ stretch and the $\nu_{P\text{-}O\text{-}H}$ stretch are observed at 902 and 1041 cm^{-1}. The $\nu_{P\text{-}O\text{-}H}$ absorption band appears at 3313 cm^{-1} and the $\nu_{P(O)\text{-}OH}$ absorption can be observed at 1633 cm^{-1}. Further characterization via ^1H NMR, provided proof of the methylene protons (***f***) resonating as a doublet at 3.59 ppm with characteristic $^2J_{H\text{-}P}$ = 13 Hz coupling as well as the phenolic hydrogens (***g***) resonating in the range of 6.3 – 7.4 ppm. The resonances of the rest of the molecule were broad undefined peaks, which can be expected for these dendritic ligands as each dendrimer arm may reside in a slightly different environment. Another explanation could be that there is a mixture of products obtained. The mixture most likely comprises of mono- bi, and tri substituted analogues as all the starting reagents are washed away during purification. The ^{13}C NMR spectra showed the carbons ***a*** and ***d*** (Reaction Scheme 3.5) in the expected region of 15 – 30 ppm, however they seem to appear in duplicate which

supports the assumption that it was a mixture of products. ^{31}P NMR spectra display several peaks in the range of 7.5 – 8.0 ppm, which again suggests that the reaction yielded a mixture of products.

In summary, for the phosphonic acid chelators, the FT-IR analysis always yielded broad undefined spectra, due to the hygroscopic nature of the products, thus only preliminary results were obtained. The FT-IR spectra of the ligands (Table 3.1) present absorption bands corresponding to $\nu_{P=O}$, $\nu_{\underline{P\text{-}O\text{-}H}}$, and $\nu_{\underline{P\text{-}O\text{-}H}}$ of the phosphonic acid moiety in the range 1200 – 1100 cm^{-1}, 900 and 1050 cm^{-1}, and 3400 – 3200 cm^{-1}, respectively.

Table 3.1: FT-IR of Phosphonic acid chelators.

Compound	$\nu_{C=O}$ (cm^{-1})	ν_{N-H} (cm^{-1})	$\nu_{P=O}$ (cm^{-1})	$\nu_{\underline{P\text{-}O\text{-}H}}$ (cm^{-1})		$\nu_{\underline{P\text{-}O\text{-}H}}$ (cm^{-1})	$\nu_{P(O)\text{-}OH}$ (cm^{-1})
ML1			1133	935		3384	1602
MC1			1120	946		3363	1618
ML2	1711		1142	912	985	3354	1638
L1	1720	3236	1168	918	1034	3354	1651
C1	1719	3387	1201		1007	3554	1639
L2			1150	902	1041	3313	1633

[a]Recorded as neat spectra on a ZnSe crystal, employing an ATR accessory.

The ^{1}H NMR spectrum obtained for **ML2**, **L1**, **C1** and **L2** could only provide tentative analysis of the compounds. In all spectra, there were resonances observed in the range of 3.5-3.7 ppm and 6 -8 ppm which correspond to the methylene (C$\underline{\mathbf{H}_2}$-P) and acidic hydrogens (P-OH), respectively. The two separate hydrogens are represented as a doublet, exhibiting the common $^{2}J_{H\text{-}P}$ = 12 – 15 Hz coupling. The ^{13}C NMR spectra display broad overlapping peaks in the region 50 – 55 ppm for $^{1}J_{C\text{-}P}$ coupling. For **ML2**, **L1**, and **C1** there appeared several peaks in the carbonyl region (170 – 180 ppm) that provide more proof that some hydrolysis occurs during the reactions, yielding a mixture of products with several different carbonyl containing moieties (Figure 3.13). It was possible to isolate the Ga (III) complex derivative of **L1**, which showed satisfactory elemental analysis and mass spectrometry result.

3.4.4 Synthesis of salicylaldimine modified Cyclam core PAMAM dendrimers

The challenges encountered during the synthesis and isolation of the phosphonic acid derivatives were the impetus for the following section. As an alternative to the phosphonic acid ligands, the Schiff base condensation reaction with salicylaldehyde was employed to obtain the peripherally modified salicylaldimine dendrimer (**L3**). The first synthesis of a Schiff base was reported by Hugo Schiff in 1864[32] and ever since there has been a great interest in these compounds. The simple condensation of aldehydes or ketones with primary amines leads to a compound with a carbon nitrogen double bond, commonly referred to as an imine. The reaction produces water and usually requires dehydrating agents or the use of a Dean Stark apparatus to remove the water and drive the reaction towards completion. The Schiff bases can decompose during purification via silica gel chromatography as the imine is susceptible to hydrolysis, thus the best purification of these ligands is achieved via recrystallization. Schiff bases can coordinate to several metals and stabilize these in various oxidation states. In addition, they offer the possibility of incorporating chirality and have known biological applications.[33, 34]

The synthesis of Schiff base derivative **L3** (0.903 g, 44 % yield) was achieved by the condensation reaction between salicylaldehyde and **D2**. The dendritic Schiff base ligand was used as a multinuclear scaffold for the preparation of gallium and copper metal complexes. Following a literature procedure[35], **C4a** was synthesized by adding $GaCl_3$ in a 2:1 mol ratio (M: L) in an attempt to isolate the dinuclear species **C4a** (0.141 g, 71 % yield). The quadrupole nuclear species **C4b** (0.169 g, 89 % yield) was prepared according to a literature procedure[36] where $Ga(acac)_3$ was used in a 1: 5 ratio (M: L). Finally, a copper derivative **C5** (0.179 g, 92 % yield) was prepared following a modified literature procedure[37] in the hope of isolating the trinuclear complex where a copper metal is situated in the cyclam core. Where possible, the ligand and its corresponding complexes (Scheme 3.6) were characterized by FT-IR, ^{1}H NMR, ^{13}C NMR, elemental analysis and ESI-MS.

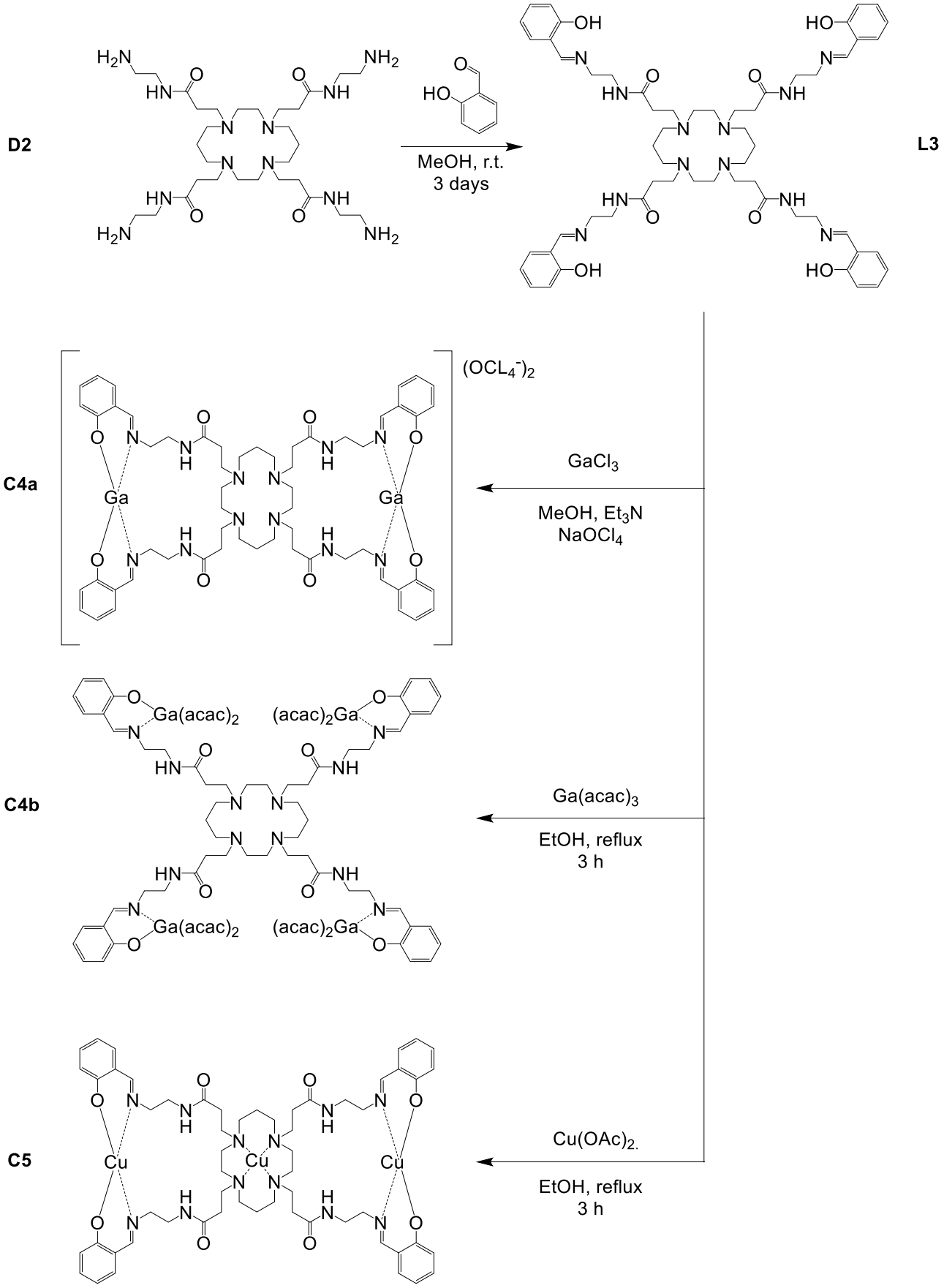

*Scheme 3.6: Synthesis of **L3**, **C4a**, **C4b** and **C5**.*

3.4.4.1 Infrared Spectroscopy and UV-Vis

The FT-IR spectra (Figure 3.15) of the ligand **L3** and the corresponding metal complexes **C4a**, **C4b** and **C5** are summarized in Table 3.2. The absorption band at 1629 cm^{-1} corresponds to $\nu_{C=N}$ of the ligand and during all the subsequent complexation reactions a shift to lower wavenumbers for the imine absorption was observed. This can be justified by the stabilization of the nitrogen lone pair by the N-Metal bond, which causes a decrease in the bond order of C=N. Further absorptions worth monitoring is the band relating to ν_{C-O}, which can be seen as a sharp medium band appearing at 1279 cm^{-1} in the ligand. The band showed a decrease in intensity and a shift to higher wavenumbers for all the complexation reactions. Generally, the O-Metal bond formation causes ν_{C-O} to shift to higher wavenumbers. These observations, coupled with the disappearance of the phenolic O-H stretch present at 3297.02 cm^{-1} for the ligand, suggests that successful complexation between the N,O donor ligands and metal has occurred.[38]

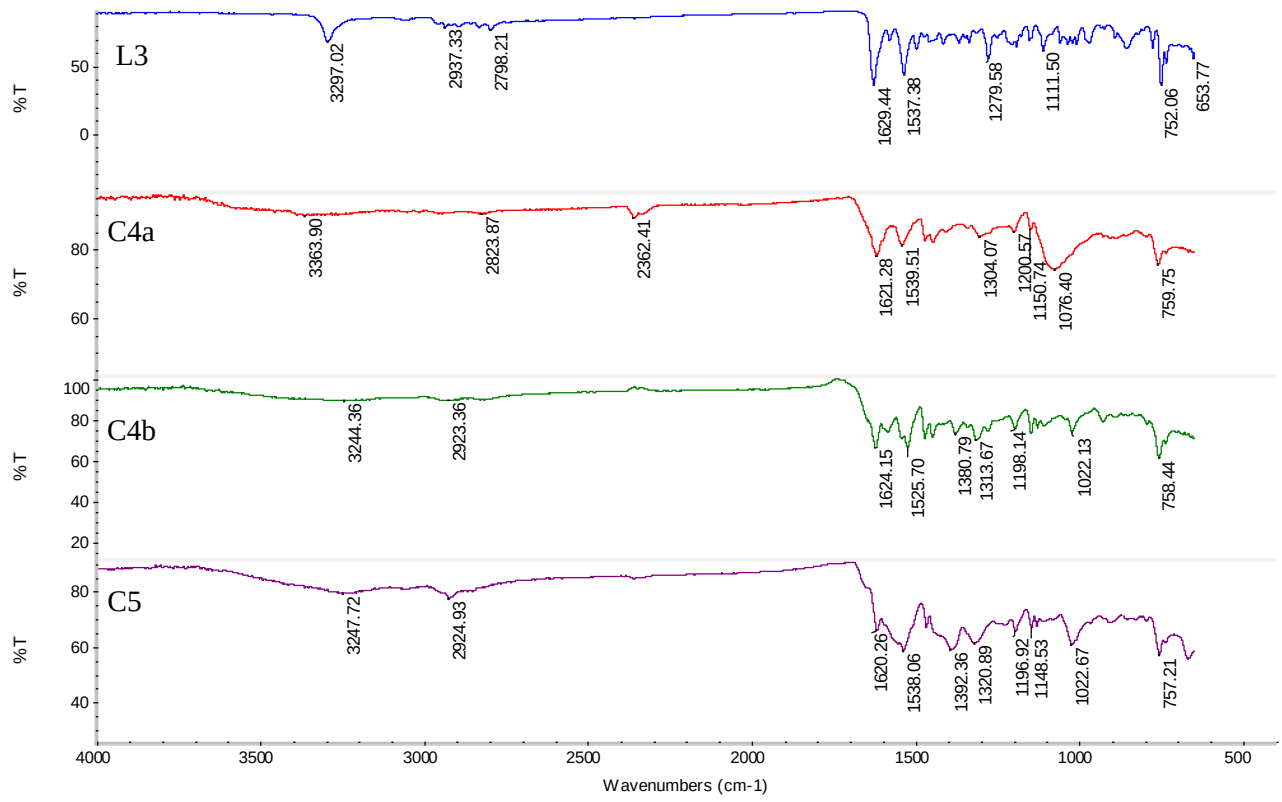

*Figure 3.15: FT-IR of (a) **L3**; (b) **C4a**; (c) **C4b**; (d) **C5**.*

The UV-Vis spectrum of the ligand **L3** as well as the complexes **C4a**, **C4b** and **C5** is shown in Figure 3.16. The ligand **L3** shows a total of 4 absorption bands and the bands at 225 and 260 nm are associated with the π-π* transition of the aromatic rings. The band at 335 nm can be attributed to the n-π* transitions of the imine group.[39] The dinuclear gallium complex **C4a** displays a total of 5 absorption bands. Both the aromatic

π-π* transition bands present in the ligand can be seen for **C4a**; however, the low wavenumber band at 225 nm was unresolved with a shoulder at 280 nm. The shoulder at 280 nm coupled with the shift of the imine n-π* transition to 324 nm suggests that the imine as well as the aromatic environments are altered during complexation, which would support the successful complexation of gallium through the salicylaldimine moiety.[40] The gallium complex **C4b** displays a total of 3 bands, both the aromatic π-π* transition bands remained virtually unchanged relative to the ligand **L3**. The imine n-π* transition has shifted slightly to 323 nm and the unknown band at 377 nm present in the spectrum of **L3** has disappeared. The trinuclear copper complex **C5** displays a total of 5 bands. The aromatic π-π* transition bands display two peaks at 224 and 235 nm correlating to the corresponding absorption at 216 nm for **L3**. The shoulder at 299 nm and the shift in imine n-π* transition to 270 nm indicate complexation of Cu (II) and the salicyldimine moiety of **L3**. No d-d transitions are possible for **C4a** and **C4b**, because Ga (III) has no available d orbitals. It is expected to observe d-d transitions for **C5** due to the d^9 configuration of Cu (II); however, none was observed due to the low intensity.

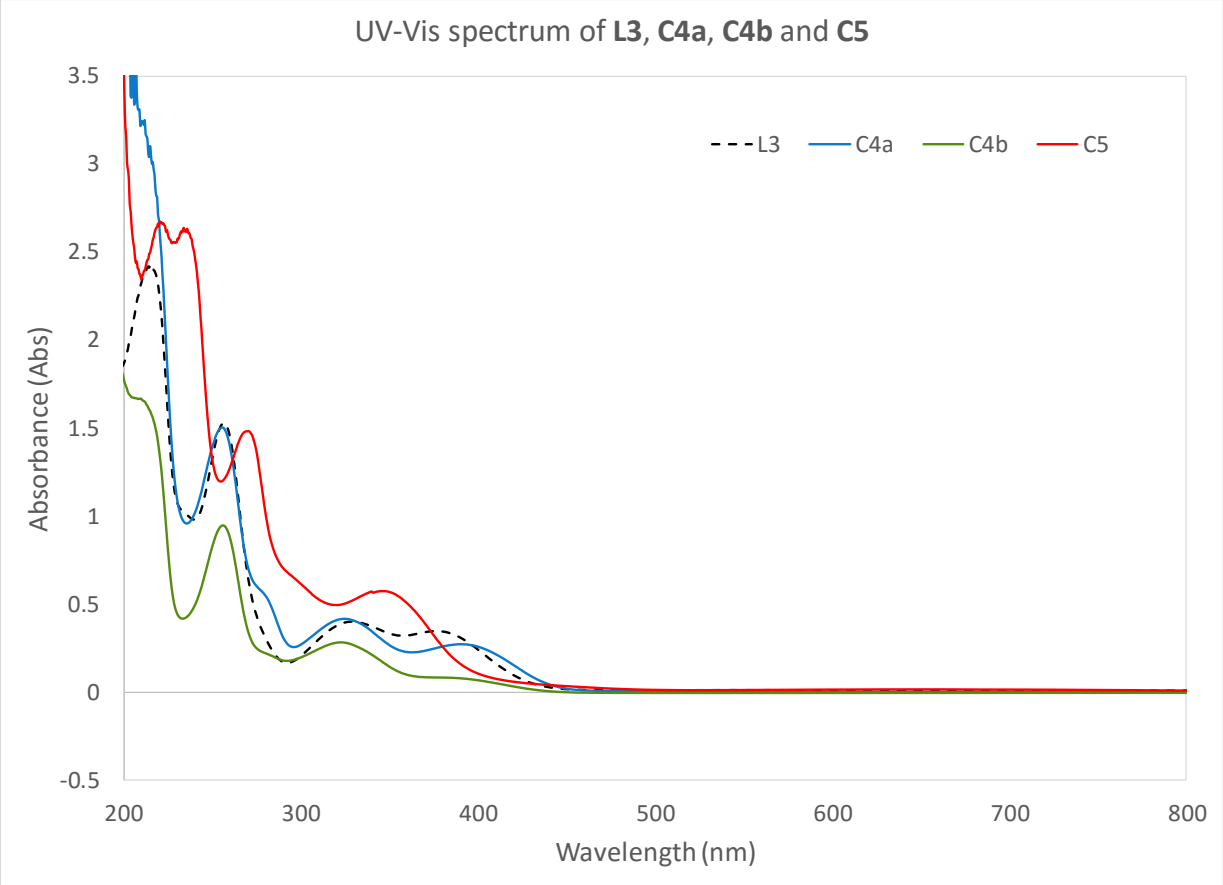

*Figure 3.16: UV-Vis of **L3** and **C4a**, **C4b** and **C5**.*

*Table 3.2: FT-IR and UV-Vis of **L3**, **C4a**, **C4b** and **C5***

Compound	FT-IR (cm^{-1})		UV-Vis (nm)		
	C=N	C-O	π-π*		n-π*
L3	1629	1280	216	256	328
C4a	1621	1304		255	324
C4b	1624	1314	210	256	323
C5	1620	1321	224 and 235	270	350

[a]Recorded as neat spectra on a ZnSe crystal, employing an ATR accessory.

3.4.4.2 Nuclear Magnetic Resonance

The ligand **L3** was further characterized by ^{1}H NMR and ^{13}C NMR. In the ^{1}H NMR spectrum the resonance at 8.30 ppm corresponds to the imine and integrates to 4 protons. A broad singlet can also be observed at 13.23 ppm indicative of the phenolic protons. The aliphatic proton ***h***, represented in Figure 3.17, resonances were observed at 2.75 ppm for **D2**, which subsequently shifted downfield to 3.70 ppm in **L3**. The formation of an imine bond stabilizes the electron pair on the nitrogen by delocalization over the aromatic ring. Thus, the de-shielded protons ***h*** is seen downfield. The ^{13}C NMR spectrum shows the imine carbon, aromatic carbons and the carbonyl carbon at 161.14, 166.59 and 172.86 ppm respectively. The same observation with regards to carbon ***h*** can be seen by the downfield shift from 41.66 ppm to 58.79 ppm from **D2** to **L3**.

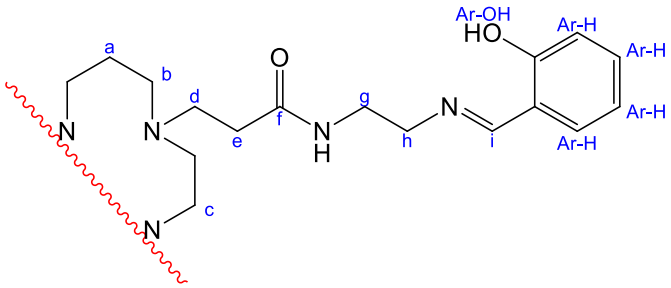

*Figure 3.17: Numbering corresponding to **D2** and **L3**.*

The complex **C4a** and **C4b** was not soluble in $CDCl_3$, thus no direct comparison could be made relative to **L3**. The NMR analysis attempted in D_2O was inconclusive. Complex **C5** was unsuitable for NMR analysis due to the paramagnetic nature of Cu.

3.4.4.3 ESI-MS and EA

ESI-MS is also useful to analyse metal chelation/ complex formation. The prominent fragments observed in ESI-MS spectra of **C4b** are highlighted in Figure 3.18. The base peak at 358 m/z can be assigned to the quadrupole pseudo molecular ion potassium ($[M +3H + K]^{4+}$) adduct of the parent ion (1488 m/z).

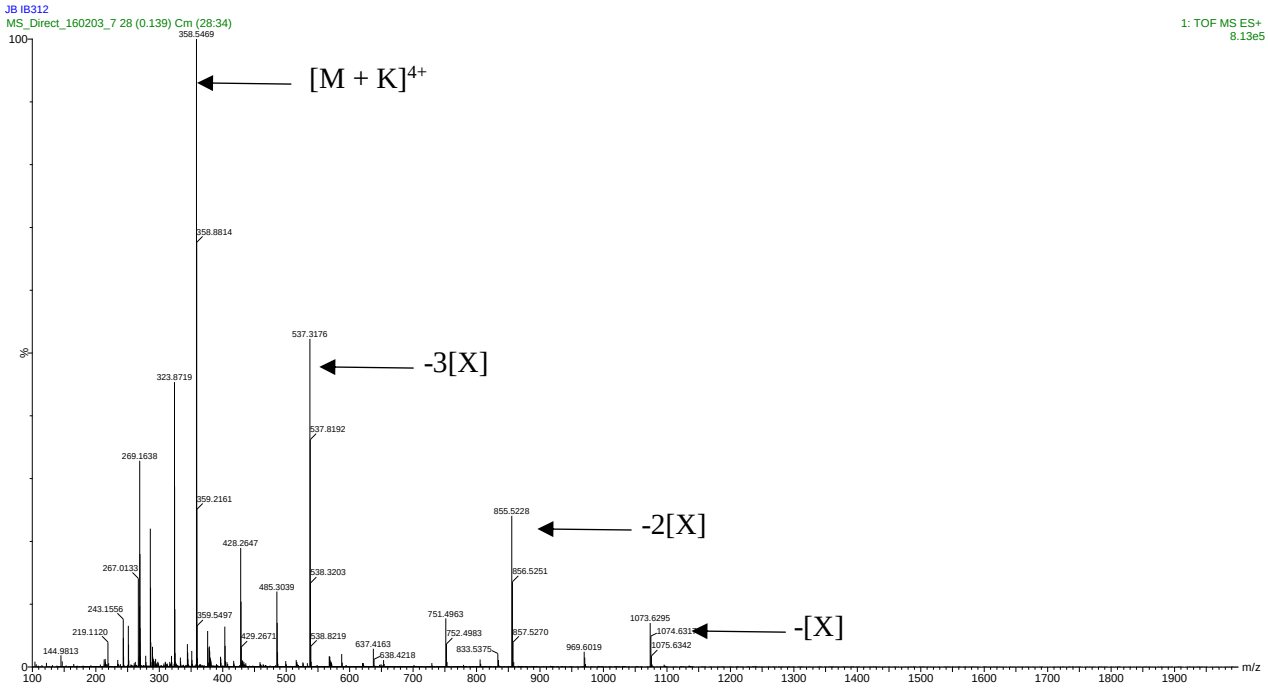

Figure 3.18: ESI MS of C4b.

A plausible fragmentation pathway (Figure 3.19) shows the parent ion (**I**) undergoing sequential loss of a complete dendrimer branch unit (X) represented by the peaks at 1073, 855, 837 m/z peaks correlating to **II**, **III**, **IV**, respectively. These values correlate well with the calculated values 1165, 842, 519 m/z, respectively. A possible explanation for the differences can be attributed to all the possible protonation sites present in the dendritic molecule. Additionally, the peak at 323 m/z correlates exactly with the calculated value of a missing branch. Further characterization of **C4b** by elemental analysis corresponded well with the calculated values although the results suggest the inclusion of water molecules within the dendrimer architecture.

The positive mode ESI-MS spectrum of **C5** display the molecular ion $[M]^+$ at 1258.40 m/z, which correlates to the ligand and three Cu (II) centers. The sequential loss of copper ions from the molecule could be observed by the m/z ratios at 1258.40, 1196.47 and 1134.56. The base peak observed at 399 m/z can be assigned to the triply-charged pseudo molecular ion with the loss of a copper center $[M - Cu]^{3+}$. The doubly-charged pseudo molecular ion $[M - Cu]^{2+}$ is also observed at 598 m/z. Additionally, the peak at 219 m/z correlates with the cyclam sodium adduct. The elemental analysis of **C5** correlates to the calculated value; however, there was once again an indication of water molecules present.

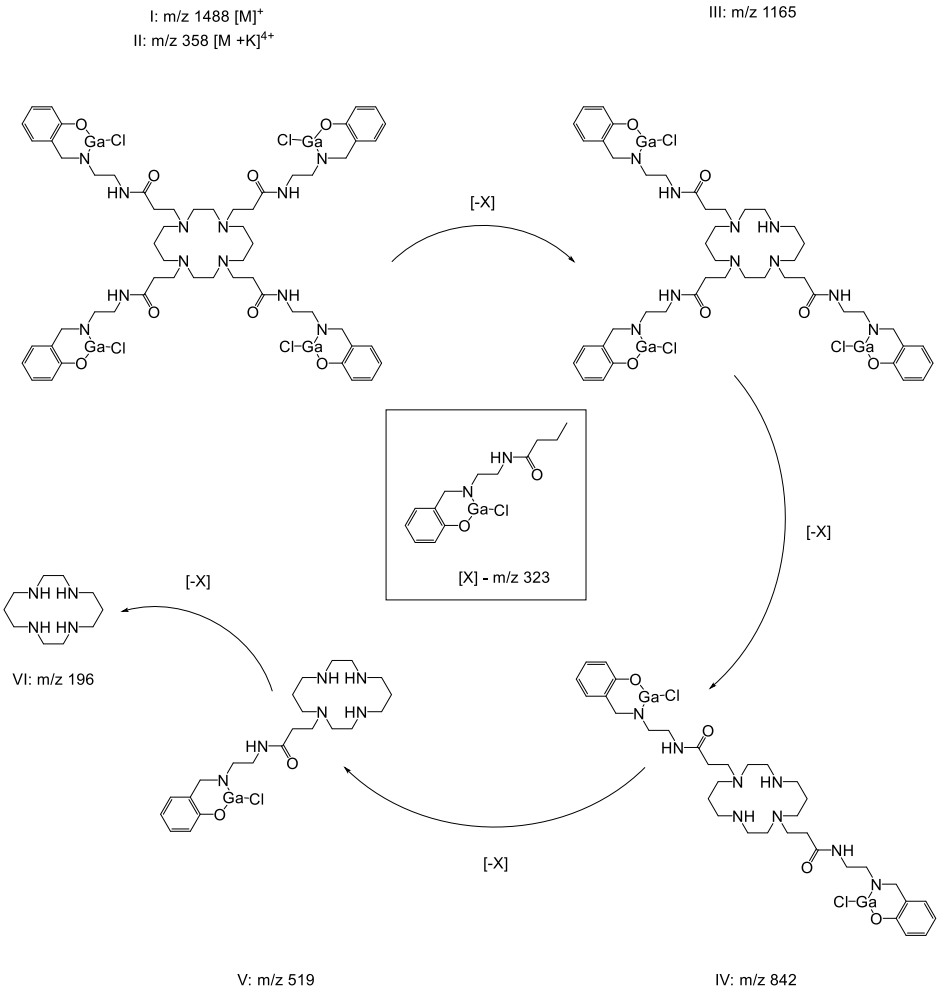

Figure 3.19: Plausible fragmentation pathway for C4b.

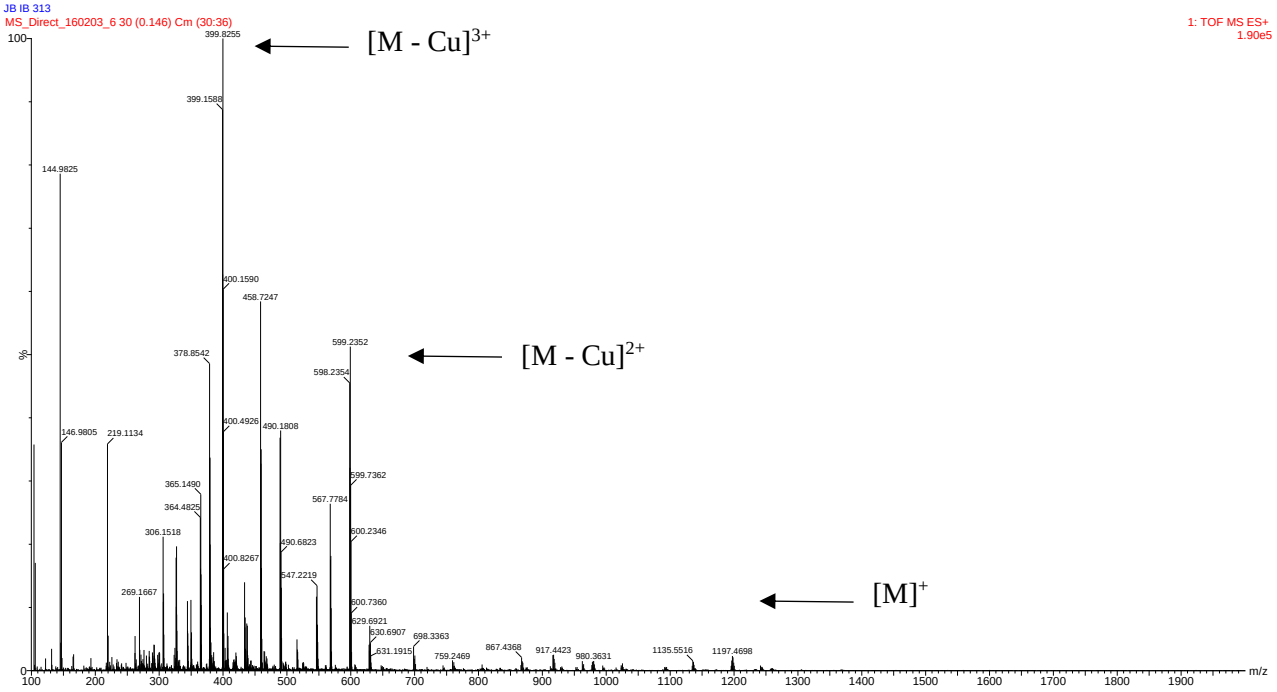

*Figure 3.20: ESI MS of **C5**.*

3.5 Conclusion

The first section of the chapter deals with the synthesis and characterization of phosphonic acid derivatives via the Irani-Moedritzer reaction and the corresponding gallium complexes. The synthesis of phosphonic acid modified cyclam-cored PAMAM dendrimers (**L1**) was attempted. Several different routes to isolate the product were attempted and were unsuccessful. Thus, the gallium complex of **L1** was synthesized in an attempt to isolate **C1**. During the synthesis of the model ligand (**ML2**), which represented the dendritic wedge of **L1**, it was suspected that the amide was susceptible to hydrolysis under the reaction conditions employed. The model ligand (**ML1**), which represented the peripheral chelator of **L1**, was successfully isolated employing the Irani-Moedritzer reaction as was the corresponding gallium complex, **MC1**. The synthesis of the dendritic analogue, **L2**, indicated that the phosphorylation of the amine functionalities had occurred, however, a mixture of mono-, di- and tri- substituted products were present in the reaction mixture.

The spectroscopic characterization of these phosphonic acid analogues was complicated due to the hygroscopic nature of the products. The FT-IR analysis always yielded broad undefined spectra and NMR results indicated a mixture of products present, thus only preliminary results were obtained. The use of dendrimers as scaffolds for these multi nuclear imaging modalities should be approached differently. An option would be to synthesize dendrons and modify these before coupling it to a core to form the dendrimer. This would simplify the purification of the dendrons and give more reassurance of the products synthesized.

Lastly, the Schiff base ligand (**L3**) was chosen as an alternative ligand based on their simplistic synthesis and range of coordination chemistry. The corresponding multinuclear complexes (**C4a**, **C4b** and **C5**) using the appropriate gallium and copper salts were all successfully synthesized and characterized.

3.6 Experimental Section

Solvents were obtained from Merck or Kimix and dried by distilling over the appropriate drying agents. Toluene was dried by distillation over sodium/benzophenone. Methanol was dried by distillation over magnesium turnings and iodine while dichloromethane was dried over phosphorus pentoxide. All reagents were purchased from either Sigma Aldrich or Merck and was used without any further purification.

All Infrared spectra were recorded on a Thermo Nicolet Avatar 330 FT-IR spectrometer with a Smart Performer (Zn/Se) ATR attachment. ^{1}H and ^{13}C nuclear magnetic resonance spectra were recorded using a 300 MHz Varian VNMRS, 400 MHz Varian Unity Inova or 600 MHz Varian Unity Inova NMR instrument using deuterated solvents. Chemical shifts (δ) were recorded using the residual solvent peak or external reference (TMS). All chemical shifts are reported in parts per million and all spectra were obtained at 25 °C. Samples for EA analysis were done on a Perkin-Elmer 2400 Series II CHNS/O Elemental Analyzer at the University of Kwa-Zulu Natal. Mass spectra were recorded on a Waters Synapt G2 spectrometer.

3.6.1 Synthesis of phosphonic acid modified cyclam-cored PAMAM (L1)

Solid phosphorous acid (1.0860 g, 13.244 mmol) was dissolved in 37 % hydrochloric acid (3.3 ml, 37 mmol) and refluxed at 80 °C under nitrogen before adding 37 % formaldehyde solution (1.1296 g, 15.968 mmol) dropwise. Thereafter the solution temperature was raised to 90 °C before adding **D2** (0.587 g, 0.880 mmol) dissolved in distilled water (6 ml) dropwise. After complete addition, the reaction mixture was allowed to reflux for an additional hour. The solvent of the yellow reaction mixture was removed via rotary evaporator to afford a yellow oil. The yellow residue was dissolved in a minimum amount of water and transferred to hot methanol upon which a white precipitate formed. The white precipitate (1.074 g) was filtered under nitrogen and rinsed with Et_2O before drying under vacuo. IR (cm^{-1}) υ(C=O) = 1720 cm^{-1}, υ(P=O) = 1168 cm^{-1}, ν_{sym}(P-O-H) = 918 cm^{-1}, ν_{asym}(P-O-H) = 1034 cm^{-1}, ν(P-O-H) = 3354 cm^{-1}, ν(P(O)-OH) = 1651 cm^{-1}. ^{1}H NMR (300 MHz, D_2O) δ 7.95 (s, P-O**H**), 5.77 (s, P-O**H**), 4.00 – 1.00 (m. extensive overlapping), 3.58 (m, N-C**H**$_2$-CH_2-C(O)-NH, -C(O)-NH-C**H**$_2$-CH_2-N), 3.37 (d, $^{2}J_{P,H}$ = 14 Hz, N-C**H**$_2$-P), 3.18 (m, N-CH_2-C**H**$_2$-C(O)-NH, -C(O)-NH-CH_2-C**H**$_2$-N), 1.29 (m, N-CH_2-C**H**$_2$-CH_2-N). ^{13}C {^{1}H} NMR (101 MHz, D_2O) δ 174.6 (s, **C**=O), 173.9 (s, **C**=O), 173.3 (s, **C**=O), 55 – 30 (multiple peaks), 49.4 (s, N-**C**H_2-P). ^{31}P {^{1}H} NMR (162 MHz, D_2O) δ 19.9 (s), 9.33 (s), 8.8 (s, N-CH_2-**P**), 8.5 (s), 8.0 (s), 7.6 (s), 7.4 (d, *J* = 31.7 Hz), 7.2 (s, N-CH_2-**P**), 6.9 (s), 3.6 (s,

PO_3H_3), 0.6 (s). Elemental analysis Calculated: N, 9.42; C, 28.26; H, 5.65% Experimental: N, 11.327; C, 25.445; H, 7.094%. ESI(+) MS: $[C_{42}H_{94}N_{12}O_{28}P_8]^{3+}$ = 489.29 m/z, $[C_{42}H_{94}N_{12}O_{28}P_8 + Na]^{3+}$ = 511.25 m/z (base peak), $[C_{42}H_{94}N_{12}O_{28}P_8 + 2Na]^{3+}$ = 533.21 m/z. ESI(-) MS: $[C_8H_{20}N_2O_{10}P_3 + K - H]^-$ = 434.99 m/z, $[C_8H_{18}N_2O_7P_2 + K - H]^-$ = 355.02 m/z.

3.6.2 Synthesis of Gallium (III) phosphonic acid modified cyclam-cored PAMAM (C1)

L1 (0.3036 g, 0.1704 mmol) was suspended in warm ethanol (20 ml). A suspension of $GaCl_3$ (0.5388 g, 3.060 mmol) in ethanol (5 ml) was added, before stirring the solution at reflux for 24 hours. The warm reaction mixture was slowly added to a beaker charged with 100 ml cold diethyl ether upon which a white precipitate crashed out of solution. The precipitate was isolated via filtration under nitrogen, before drying under reduced pressure overnight. **C1** (0.234 g, 57 % yield) IR (cm^{-1}) υ(C=O) = 1719 cm^{-1}, υ(P=O) = 1201 cm^{-1}, ν(P-O-H) = 1007 cm^{-1}, ν(P-O-H) = 3554 cm^{-1}, ν(P(O)-OH) = 1639 cm^{-1}. ^{1}H NMR (600 MHz, D_2O) δ 7.40 (s, P-O**H**), 6.33 (s, P-O**H**), 4.00 – 1.00 (m. extensive overlapping), 3.62 (d, $^2J_{P,H}$ = 12.3 Hz, N-C**H**$_2$-P), 1.30 (m, N-CH_2-C**H**$_2$-CH_2-N). ^{31}P NMR {^{1}H} (121 MHz, D_2O) δ 17.9 (s), 10.0 – 7.0 (m, N-CH_2-**P**), 4.4 (s, **P**O_3H_3). Elemental analysis: Found: C: 21.003 %, N: 7.179 %, H: 5.379 %; Calculated: C: 20.98 %; N: 6.99 %; H: 3.69 %. ESI(+) MS: $[C_3H_7NO_6P_2GaCl + K]^+$ = 357.04 m/z.

3.6.3 Synthesis of Model Ligand 2

3.6.3.1 Synthesis of dimethyl 3,3'-(propylazanediyl)dipropanoate (ML2a)

Propyl amine (1.048 g, 17.73 mmol) was dissolved in MeOH (3 ml) before adding methyl acrylate (16 ml, 177 mmol). The reaction mixture was placed in the microwave reactor for 90 minutes at 40 °C with 50 W radiation. The reaction mixture was cooled to room temperature, before repeating the microwave reaction as mentioned above. The solvent was removed to afford a yellow oil. The oil was purified via silica gel chromatography using the eluent DCM: MEOH (9:1) to afford a light yellow oil (3.049 g, 74 % yield). IR (cm^{-1}) υ(C=O) = 1732 cm^{-1}. υ(C-N) = 1435 cm^{-1}. ^{1}H NMR (600 MHz, $CDCl_3$) δ 3.63 (s, 6H, -C(O)OC**H**$_3$), 2.73 (t, $^3J_{H-H}$ = 7.2 Hz, 4H, -N-(C**H**$_2$-CH_2-C(O)OMe)$_2$), 2.41 (t, $^3J_{H-H}$ = 7.2 Hz, 4H, -N-(CH_2-C**H**$_2$-C(O)OMe)$_2$), 2.35 – 2.33 (m, 2H, CH_3-CH_2-C**H**$_2$-N), 1.44 – 1.37 (m, 2H, CH_3-C**H**$_2$-CH_2-N), 0.81 (t, $^3J_{H-H}$ = 7.4 Hz, 3H, -C**H**$_3$). ^{13}C NMR {^{1}H} (151 MHz, $CDCl_3$) δ 172.9 (s, **C**=O), 55.7 (s, CH_3-CH_2-C**H**$_2$-N), 51.5 (s-N-(**C**H_2-CH_2-

C(O)OMe)$_2$), 49.2 (s, -C(O)O**C**H$_3$), 32.4 (s, -N-(CH$_2$-**C**H$_2$-C(O)OMe)$_2$), 20.1 (s, CH$_3$-**C**H$_2$-CH$_2$-N), 11.6 (s, **C**H$_3$-CH$_2$-CH$_2$-N).

3.6.3.2 Synthesis of 3,3'-(propylazanediyl)bis(N-(2-aminoethyl)propanamide) (ML2b)

Ethylenediamine (88 ml, 131 mmol) dissolved in EtOH (100 ml) was added to a stirring solution of dimethyl 3,3'-(propylazanediyl)dipropanoate (3.049 g, 13.18 mmol) dissolved in EtOH (20 ml). The reaction mixture was stirred in the dark at room temperature for 5 days. The solvent and excess ethylenediamine was removed via rotary evaporizer to obtain ML2b as a yellow oil (3.012 g, 79 % yield). IR (cm^{-1}) υ(C=O) = 1636 cm^{-1}. υ(C-N) = 1456 cm^{-1}, υ(N-H$_{stretch}$) = 3283 cm^{-1} and υ(N-H$_{bend}$) = 1544 cm^{-1}. ^{1}H NMR (400 MHz, D$_2$O) δ 3.24 (t, *J* = 6.3 Hz, 4H, -N-(CH$_2$-CH$_2$-C(O)-NH-C**H$_2$**-CH$_2$-NH$_2$)$_2$)), 2.80 (t, *J* = 7.4 Hz, 4H, -N-(CH$_2$-CH$_2$-C(O)-NH-CH$_2$-C**H$_2$**-NH$_2$)$_2$)), 2.72 (t, *J* = 6.3 Hz, 4H, -N-(C**H$_2$**-CH$_2$-C(O)-NH-CH$_2$-CH$_2$-NH$_2$)$_2$)), 2.69 (s, 3H, **EDA**), 2.44 (m, 4H, -N-(CH$_2$-C**H$_2$**-C(O)-N-CH$_2$-CH$_2$-NH$_2$)$_2$), 2.43 – 2.41 (m, 2H, CH$_3$-CH$_2$-C**H$_2$**-N), 1.52 – 1.42 (m, 2H, CH$_3$-C**H$_2$**-CH$_2$-N), 0.87 (t, $^3J_{H\text{-}H}$ = 7.4 Hz, 3H, -C**H$_3$**). ^{13}C NMR {^{1}H} (151 MHz, CDCl$_3$) δ 172.8 (s, **C**=O), 55.5 (s, CH$_3$-CH$_2$-C**H$_2$**-N), 50.0 (s N-(**C**H$_2$-CH$_2$-C(O)NH)$_2$), 46.4 (s), 45.6 (s), 44.8 (s), 44.0 (s), 43.5 (s), 42.8 – 41.8 (m, C(O)NH-CH$_2$-**C**H$_2$-NH$_2$), 41.6 (s), 41.4 (s, C(O)NH-CH$_2$-**C**H$_2$-NH$_2$), 40.2 (s), 39.3 (s), 35.7 (s), 33.9 (m, -N-(CH$_2$-**C**H$_2$-C(O)NH)$_2$), 33.6 (s), 32.5 (s), 23.0 (s), 19.8 (s, CH$_3$-**C**H$_2$-CH$_2$-N), 11.9 (s, **C**H$_3$-CH$_2$-CH$_2$-N).

3.6.3.3 Synthesis of ML2

3,3'-(propylazanediyl)bis(N-(2-aminoethyl)propanamide) **ML2b** (0.185 g, 0.641 mmol) was dissolved in ethanol (1 ml), before adding phosphorous acid (0.642 g, 7.83 mmol) and 37 % HCl (0.90 ml) to the light yellow solution. The reaction mixture was stirred at room temperature for 1 hour before adding 35 % formaldehyde (1.0 ml). The reaction mixture was left to stir overnight before raising the temperature to 100 °C for 8 hours. Thereafter the solvent was removed via the rotary evaporizer (60 °C) to obtain a golden oil. The oil was dissolved in warm ethanol before adding the solution to cold diethyl ether. A white precipitate immediately crashed out of solution. The precipitate was isolated via filtration under a nitrogen blanket; however due to its hygroscopic nature, the precipitate quickly became a sticky yellow viscous solid. (0.421 g, 77 % yield) IR (cm^{-1}) υ(C=O) = 1711 cm^{-1}, υ(P=O) = 1142 cm^{-1}, ν_{sym}(P-O-H) = 912 cm^{-1}, ν_{asym}(P-O-H) = 985 cm^{-1}, ν(P-O-H) = 3354 cm^{-1}, ν(P(O)-OH) = 1638 cm^{-1}. ^{1}H NMR (400 MHz, D$_2$O) δ 7.64 (s, P-O**H**), 6.04 (s, P-O**H**) 3.95 (d, *J* = 21.4 Hz), 3.91 – 3.49 (m,N-**C**H$_2$-P), 3.49 – 3.15 (m), 3.26 (d, *J* = 4.2 Hz), 3.26 (d, *J* = 4.2

Hz), 3.09 (s, possibly **C**=O), 2.80 (d, *J* = 4.6 Hz), 1.78 (m, CH_3-C**H**$_2$-CH_2-N) 1.17 (t, *J* = 7.1 Hz, C**H**$_3$-CH_2-CH_2-N), 0.97 (t, *J* = 7.4 Hz, C**H**$_3$-CH_2-CH_2-N).

3.6.4 Synthesis of ((propylazanediyl)bis(methylene))diphosphonic acid (ML1)

Phosphorous acid dissolved in distilled water (10 ml) was added to a stirring solution of 37 % hydrochloric acid (5 ml, 60 mmol) while maintaining the temperature below 40 °C. Propyl amine (0.7234 g, 12.24 mmol) was dissolved in distilled water (10 ml), before adding the yellow solution dropwise over an hour to the HCl/PO_3H_3 solution. Upon complete addition, the solution temperature was raised to 85 °C before adding 35 % paraformaldehyde solution (4.5 ml, 60 mmol) dropwise. The reaction mixture was refluxed (105 °C) an additional hour. The solvent was removed to afford a clear oil. The oil was dissolved in methanol and layered with diethyl ether before placing the solution in the freezer overnight. The resulting white precipitate was separated via filtration and dried under high vacuo for 24 h before isolating **ML1** (2.412 g, 80 % yield). IR (cm^{-1}) υ(P=O) = 1133 cm^{-1}, *ν*(P-O-H) = 935 cm^{-1}, *ν*(P-O-H) = 3384 cm^{-1}, *ν*(P(O)-OH) = 1602 cm^{-1}. ^{1}H NMR (600 MHz, D_2O) δ 7.32 (s, P-O**H**), 6.20 (s, P-O**H**), 3.45 (d, $^2J_{H,P}$ = 12.8 Hz, 4H, -N-(C**H**$_2$-PO_3H_2)$_2$), 3.34 – 3.31 (m, 2H, CH_3-CH_2-C**H**$_2$-N), 1.69 – 1.63 (m, 2H, CH_3-C**H**$_2$-CH_2-), 0.84 (t, $^3J_{H-H}$ = 7.4 Hz, 3H, C**H**$_3$-CH_2). ^{13}C NMR {^{1}H} (101 MHz, D_2O) δ 59.0 (t, $^3J_{C-P}$ = 3.8 Hz, -**C**H_2-N-(CH_2-PO_3H_2)$_2$), 51.6 (d, $^1J_{C,P}$ = 137.8 Hz, -N-**C**H_2-PO_3H_2), 17.4 (s, CH_3-**C**H_2-CH_2-N), 10.4 (s, **C**H_3-CH_2-CH_2-N). ^{31}P NMR (162 MHz, d_2o) δ 23.2 (s), 8.8 (s, -N-(CH_2-**P**O_3H_2)$_2$)), 5.4 (s, **P**O_3H_3), 5.1 (t, $^1J_{P-H}$ = 102.8 Hz, -N-(CH_2-**P**O_3H_2)$_2$)). Elemental analysis Calculated: N, 7.29; C, 22.63; H, 6.64 % Experimental: N, 5.67; C, 24.30 and H, 6.12 %. ESI(-) MS: $[M - H]^-$ = 246 m/z.

3.6.5 Synthesis of gallium ((propylazanediyl)bis(methylene))bis(hydrogen phosphonate) chloride (MC1)

Solid $GaCl_3$ (3.0911 g, 17.565 mmol) was dissolved in 5 ml dry methanol. **ML1** (0.955 g, 3.86 mmol) was suspended in 15 ml dry methanol before adding of 3.51 M $GaCl_3$ solution (0.95 ml, 3.3 mmol) to the suspension. Upon addition, the milky white solution immediately became clear pink, gradually changing to purple after 1 hour. The reaction mixture was allowed to stir an additional 12 hours, during which the solution became milky white. The solvent was removed via rotary vaporizer. The residue was dissolved in a minimum amount of toluene and layered with diethyl ether. After 1 day, the white precipitate (1.0255 g, 75 % yield) was isolated via filtration. m.p. > 250 °C, IR (cm^{-1}) υ(P=O) = 1120 cm^{-1}, *ν*(P-O-H) = 946 cm^{-1}, *ν*(P-O-H) = 3363

cm^{-1}, ν(P(O)-OH) = 1618 cm^{-1}. ^{1}H NMR (400 MHz, D_2O) δ 7.66 (s, P-O**H**), 6.06 (s, P-O**H**), 3.79 (d, J = 7.31 Hz) 3.75 – 3.10 (m),3.01 (s), 1.86 – 1.72 (m, CH_3-C**H$_2$**-CH_2-N), 1.01 – 0.96 (m, C**H$_3$**-CH_2-CH_2-N). ^{13}C NMR (101 MHz, D_2O) δ 54.4 (s), 10.5 (dd, *J* = 3.6, 2.3 Hz). ^{31}P NMR (162 MHz, d_2o) δ 21.3 (s), 9.8 (s), 8.2 – 8.1 (m, -N-(CH_2-**P**O_3H_2)$_2$)), 4.3 - 3.8 (m, **P**O_3H_3). Elemental analysis Calculated: N, 4.00; C, 17.14; H, 3.74 % Experimental: N, 5.73; C, 18.82; H, 5.27 %. ESI(-) MS: $[M - 2H + MeOH]^{2-}$ = 190 m/z.

3.6.6 Synthesis of L2

G1 DAB-PPI (0.682 g, 2.15 mmol) dissolved in distilled water (5 ml) before adding phosphorous acid (2.827 g, 34.47 mmol) and 37 % HCl (4.3 ml, 51 mmol) to the solution whilst ensuring the temperature stayed below 40 °C. Thereafter 37 % formaldehyde (3.4 ml, 43 mmol) was added dropwise before the reaction temperature was raised to 100 °C. After the reaction mixture was stirred for 4 hours the warm solution was immediately added to cold EtOH (200 ml) upon which a precipitate formed. The precipitate (1.748 g) was washed with diethyl ether, taken up in water and freeze dried before analysis. IR (cm^{-1}) ν(P=O) = 1150 cm^{-1}, ν_{sym}(P-O-H) = 902 cm^{-1}, ν_{asym}(P-O-H) = 1041 cm^{-1}, ν(P-O-H) = 3313 cm^{-1}, ν(P(O)-OH) = 1633 cm^{-1}. ^{1}H NMR (600 MHz, D_2O) δ 7.42 (s, P-O**H**), 3.62 (s, P-O**H**), 3.78 (d, *J* = 12.9 Hz, -N-C**H$_2$**-PO_3H_2), 3.59 (d, *J* = 12.6 Hz, -N-C**H$_2$**-PO_3H_2), 3.35 – 3.31 (m), 3.06 – 3.03 (m), 2.98 – 2.90 (m), 2.31 (m, N-C**H$_2$**-CH_2-CH_2-C**H$_2$**-N), 1.86 (m, N-CH_2-C**H$_2$**-C**H$_2$**-CH_2-N). ^{13}C NMR {^{1}H} (75 MHz, D_2O) δ 58.0 (s), 53.5 – 49.5 (m), 37.0 (s), 22.2 (s), 21.1 (s), 19.0 (s), 17.4 (s). ^{31}P NMR {^{1}H} (162 MHz, D_2O) δ 21.9 (s), 9.5 – 9.3 (m), 8.0 – 7.4 (m, -N-CH_2-**P**O_3H_2), 4.1 (s, **P**O_3H_3), 0.6 (s).

3.6.7 Synthesis of L3

G1.0 Cyclam core PAMAM (1.250 g, 1.900 mmol) was dissolved in ethanol (20 ml) before adding salicylaldehyde (1.62 ml, 15,2 mmol) and stirring the solution at room temperature for 3 days. A yellow precipitate was observed after 1 day. After 3 days the reaction flask was placed in the freezer for an hour before isolating the yellow precipitate via filtration. The precipitate was rinsed with cold methanol (3 portions of 20 ml). The solvent of the filtrate was reduced and the concentrated solution placed in the freezer overnight. The resulting yellow precipitate was filtered. The combined precipitate (0.903 g, 44 % yield) was dried under reduced pressure overnight. IR (cm^{-1}) ν(N-H) = 3297 cm^{-1}, ν(C=O) = 1629 cm^{-1}. ^{1}H NMR (600 MHz, $CDCl_3$) δ 13.2 (s, O**H**), 8.30 (s, 4H, **H**C=N), 7.39 – 7.26 (dt, $^{3}J_{H-H}$ = 7.7 Hz, $^{4}J_{H-H}$ 1.7 Hz= , 4H, Ar-**H**), 7.21 (dd, $^{3}J_{H-H}$ = 7.7Hz, $^{4}J_{H-H}$ = 1.6 Hz, 4H, Ar-**H**), 6.89 (d, $^{3}J_{H-H}$ = 8.2 Hz, 4H, Ar-**H**), 6.86 (t, $^{3}J_{H-H}$ = 7.5 Hz, 4H, Ar-**H**), 3.70

(t, *J* = 5.6 Hz, 8H, -C(O)-NH-CH_2-C**H**$_2$-N=), 3.52 (dd, *J* = 11.5, 5.8 Hz, H, -C(O)-NH-C**H**$_2$-CH_2-N=), 2.52 (t, 8H, -N-C**H**$_2$-CH_2-C(O)NH-), 2.34 (s, 8H, -N-C**H**$_2$-C**H**$_2$-N-), 2.24 (tt, 16H, -N-C**H**$_2$-CH_2-C**H**$_2$-N- and -N-CH_2-C**H**$_2$-C(O)NH-), 1.35 (s, 4H, -N-CH_2-C**H**$_2$-CH_2-N-). ^{13}C NMR {^{1}H} (151 MHz, $CDCl_3$) δ 172.8 (s, -**C**(O)NH-), 166.5 (s, Ar-OH), 161.1 (s, -**C**H=N-), 132.6 (s, Ar), 31.6 (s, Ar), 118.9 (s, Ar), 118.7 (s, Ar), 117.1 (s, Ar), 58.7 (s, -C(O)-NH-CH_2-**C**H_2-N=), 51.1 (s, -N-**C**H_2-CH_2-C(O)NH-), 50.6 (s, -N-C**H**$_2$-CH_2-C**H**$_2$-N-), 49.3 (s, -N-**C**H_2-**C**H_2-N-), 40.1 (s, -C(O)-NH-**C**H_2-CH_2-N=), 33.1 (s, -N-CH_2-**C**H_2-C(O)NH-), 22.6 (s, -N-CH_2-**C**H_2-CH_2-N-).

3.6.8 Synthesis of C4a

$GaCl_3$ (0.571 g, 0.328 mmol) was dissolved in dry methanol (5 ml) and added to a stirring solution of **L3** (0.176 g, 0.164 mmol) and Et_3N in dry methanol (30 ml). The reaction mixture was stirred for 1 hour before adding excess sodium perchlorate. After 24 hours, the yellow precipitate was isolated via filtration and dried under reduced pressure. (**C4a**, 0.141 g, 71.21 % yield). IR (cm^{-1}) ν(C=N) = 1621 cm^{-1}, ν(C-O) = 1304 cm^{-1}. UV-Vis (nm) π-π* = 255 nm, n-π* = 324 nm.

3.6.9 Synthesis of C4b

$Ga(acac)_3$ (0.6881 g, 1.773 mmol) was dissolved in dry ethanol (5 ml) and added dropwise to a stirring solution of **L3** (0.1904 g, 0.1774 mmol) in dry ethanol (20 ml). The reaction mixture was stirred under inert conditions at reflux temperature for 3 hours. Thereafter, the solvent was removed and the obtained yellow precipitate was purified by dissolving it in a minimum amount of ethanol and layering the solution with diethyl ether before cooling the solution to 8 ° C for 24 hours. The resulting yellow precipitate was isolated via filtration and rinsed with dry diethyl ether before drying under reduced pressure. (**C4b**, 0.169 g, 88.95 % yield) IR (cm^{-1}) ν(C=N) = 1624 cm^{-1}, ν(C-O) = 1314 cm^{-1}. UV-Vis (nm) π-π* = 210 and 256 nm, n-π* = 323 nm. ESI MS: $[M + K]^{4+}$ = 358 m/z.

3.6.10 Synthesis of C5

Copper acetate (0.1716 g, 0.8601 mmol) was dissolved in dry ethanol (20 ml) and added dropwise to a stirring solution of **L3** (0.1737 g, 0.1618 mmol) in dry ethanol (20 ml). The green reaction mixture was stirred under inert conditions at reflux temperature for 3 hours. Thereafter, the solvent was removed and the obtained green precipitate was recrystallized by cooling a concentrated solution 8 ° C for 24 hours. The resulting green precipitate was isolated via filtration and rinsed with dry diethyl ether before drying under reduced pressure.

(**C5**, 0.179 g, 92.27 % yield) IR (cm^{-1}) ν(C=N) = 1620 cm^{-1}, ν(C-O) = 1321 cm^{-1}. UV-Vis (nm) π-π^* = 224, 235 and 270 nm, n-π^* = 350 nm. ESI MS: $[M]^+$ = 1197 m/z, $[M - Cu]^{2+}$ = 598 m/z, $[M - Cu]^{3+}$ = 399 m/z.

3.7 References

(1) Naydenova, E. D.; Todorov, P. T.; Troev, K. D. *Amino Acids* **2010**, *38* (1), 23–30.

(2) Jordanov, N.; Mareva, S.; Borisov, G.; Jordanov, B. *Talanta* **1968**, *15* (2), 221–227.

(3) Zon, J.; Garczarek, P.; Bialek, M. In *Metal Phosphonate Chemistry: from Synthesis to Applications*; Royale Scociety of Chemistry, 2012; pp 170–191.

(4) Ordóñez, M.; Rojas-Cabrera, H.; Cativiela, C. *Tetrahedron* **2009**, *65* (1), 17–49.

(5) Michaelis, A.; Kaehne, R. *Berichte der Dtsch. Chem. Gesellschaft* **1898**, *31* (1), 1048–1055.

(6) Arbuzov, A. E. *J.Russ. Phys. Chem. Soc.* **1906**, *38*, 687.

(7) Bhattacharya, A.; Thyagarajan, G. *Chem. Rev.* **1981**, *81*, 415–430.

(8) Abramov, B. *Dokl. Akad. Nauk SSSR* **1950**, *73*, 487.

(9) Pudovik. *Bull. Acad. Sci. USSR. Div. Chem. Sci (Eng Transl).* **1978**, *27*, 2319.

(10) Kabachnik, M. I.; Medved, T. Y. *Dokl. Akad. Nauk SSSR* **1952**, *83*, 689–692.

(11) Fields, E. K. *J. Am. Chem. Soc.* **1952**, *74*, 1528–1531.

(12) Zefirov, N. S.; Matveeva, E. D. *Arkivoc* **2008**, No. 1, 1–17.

(13) Cherkasov, R. A.; Galkin, V. I. *Russ. Chem. Rev.* **1998**, *67* (10), 857–882.

(14) Gancarz, R. *Tetrahedron* **1995**, *51* (38), 10627–10632.

(15) Dimukhametov, M. N.; Bayandina, E. V.; Davydova, E. Y.; Gubaidullin, A. T.; Litvinov, I.; Alfonsov, V. *Mendeleev Commun.* **2003**, *13* (3), 150–151.

(16) Keglevich, G.; Bálint, E. *Molecules* **2012**, *17* (11), 12821–12835.

(17) Moedritzer, K.; Irani, R. *J. Org. Chem.* **1966**, *477*, 1603–1607.

(18) Turrin, C.; Hameau, A.; Caminade, A. *Synthesis (Stuttg).* **2012**, *44*, 1628–1630.

(19) Ran, Q.; Ma, J.; Wang, T.; Zhao, H.; Song, F.; Fan, S.; Yang, Y.; Lyu, Z.; Liu, J. *Colloid. Polym. Sci.* **2016**, *294*, 189–198.

(20) Jarvis, N. V.; Zeevaart, J. R.; Wagener, J. M.; Louw, W. K. A.; Dormehl, I. C.; Milner, R. J.; Killian, E. *Radiochim. Acta* **2002**, *90* (4), 237–246.

(21) Lazar, I.; Hrncir, D. C.; Kim, W.; Kiefer, G. E.; Sherry, A. D. *Inorg. Chem.* **1992**, *31* (17), 4422–4424.

(22) Li, F.; Zhang, B.; Wang, H.; Wu, Y. Ethylenediamine core, octamethylenephosphonic acid terminated, PAMAM dendrimer and its use as antiscalant. US 2014/0319064 A1, 2014.

(23) Sherry, A. D.; Malloy, C. R.; Jeffrey, F. M.; Acheris, W. P.; Gefuldes, C. F. G. C. *J. Magn. Reson.* **1988**, *76*, 528–533.

(24) Ferdani, R.; Stigers, D. J.; Fiamengo, A. L.; Wei, L.; Li, B. T. Y.; Golen, J. A.; Rheingold, A. L.; Weisman, G. R.; Wong, H.; Anderson, C. J. *Dalton Transactions* **2012**, *41*, 1938–1950.

(25) Naydenova, E.; Topashka-Ancheva, M.; Todorov, P.; Yordanova, T.; Troev, K. *Bioorg. Med. Chem.* **2006**, *14* (7), 2190–2196.

(26) Holub, J.; Meckel, M.; Kubíček, V.; Rösch, F.; Hermann, P. *Contrast Media Mol. Imaging* **2015**, *10* (2), 122–134.

(27) Šimeček, J.; Zemek, O.; Hermann, P.; Notni, J.; Wester, H.-J. *Mol. Pharm.* **2014**, *11*, 3893–3903.

(28) Socrates, G. *Infrared Characteristic Group Frequencies*, Second edd.; John Wiley & Sons, 1995.

(29) Bosica, G.; Debono, A. J. *Tetrahedron* **2014**, *70* (37), 6607–6612.

(30) Oleksyszyn, J.; Gruszecka, E. *Tetrahedron Lett.* **1981**, *22* (56), 3537–3540.

(31) Gholivand, K.; Ghaziani, F.; Yaghoubi, R.; Hosseini, Z.; Shariatinia, Z. *J. Enzyme Inhib. Med. Chem.* **2010**, *25* (6), 827–835.

(32) Schiff, H. *Ann Suppl* **1864**, *3*, 343.

(33) Mishra, N.; Kavitan, P.; Kumar, D. *Int. J. Adv. Res. Technol.* **2013**, *2* (8), 52–66.

(34) Zoubi, W. Al. *Int. J. Org. Chem.* **2013**, *3*, 73–95.

(35) Shakya, R.; Peng, F.; Liu, J.; Heeg, M. J.; Verani, C. N. *Inorg. Chem.* **2006**, *45* (16), 6263–6268.

(36) Tsang, B. W.; Mathias, C. J.; Fanwick, P. E.; Green, M. A. *J. Med. Chem.* **1994**, *37*, 4400–4406.

(37) Malgas-Enus, R.; Mapolie, S. F. *Polyhedron* **2012**, *47* (1), 87–93.

(38) Aranha, P. E.; Santos, M. P.; Romera, S.; Dockal, E. R. *Polyhedron* **2006**, 26 (7) 1373-1382.

(39) Xavier, A.; Xavier, A.; Gobu, P.; Srividhya, N. *Int. J. Multidiscip. Res. Dev.* **2015**, *2* (5), 134–138.

(40) Khalil, M. M. H.; Ismail, E. H.; Mohamed, G. G.; Zayed, E. M.; Badr, A. *Open J. Inorg. Chem.* **2012**, *2*, 13–21.

4 DNA BINDING STUDIES

4.1 Introduction

In this chapter, the focus shifts towards drug-DNA interaction, with a particular focus on dendrimers, ligands and complexes synthesized and discussed in preceding chapters. The aim was to establish whether the compounds interacted with DNA and if so, how and to what extent? The introduction looks at the DNA structure in relation to all the possible binding modes. These binding modes are categorized as covalent or non-covalent. Lastly, the preliminary assessment of the selected compounds by means of UV-Vis spectroscopy titration experiments is discussed.

4.2 DNA Structure

DNA has been known to be the cellular target for many cytotoxic anticancer agents. Targeting DNA allows for the regulation of cell functions by controlling transcription pathways or by interfering with replication. A quick look at the structure of DNA (Figure 4.1) indicates several possible modes of bonding. A single strand consists of DNA bases (Adenine, Cytosine, Guanine, Thymine) in four possible combinations which are connected to a backbone of deoxyribose sugars. These sugars are covalently linked through one or more phosphate groups at the 3' and/or 5' hydroxy group forming a phosphodiester linkage. The DNA bases interact through Watson-Crick hydrogen bonds, which gives the famous double helix structure.[1] The DNA bases present sites where alkyl groups can be added, where drug molecules can bind covalently and even crosslink consecutive base pairs. The cavity in-between base pairs stabilize molecules via π-π stacking, the major and minor grooves stabilize drug molecules through van der Waals and/or hydrogen bonding while the phosphate backbone offers the opportunity for electrostatic interactions.

4.3 Mode of DNA binding

For the effective design of drug molecules, it is important to know the mode of DNA binding of the molecule under investigation. If the mode of binding can be associated with specific aspects present in the

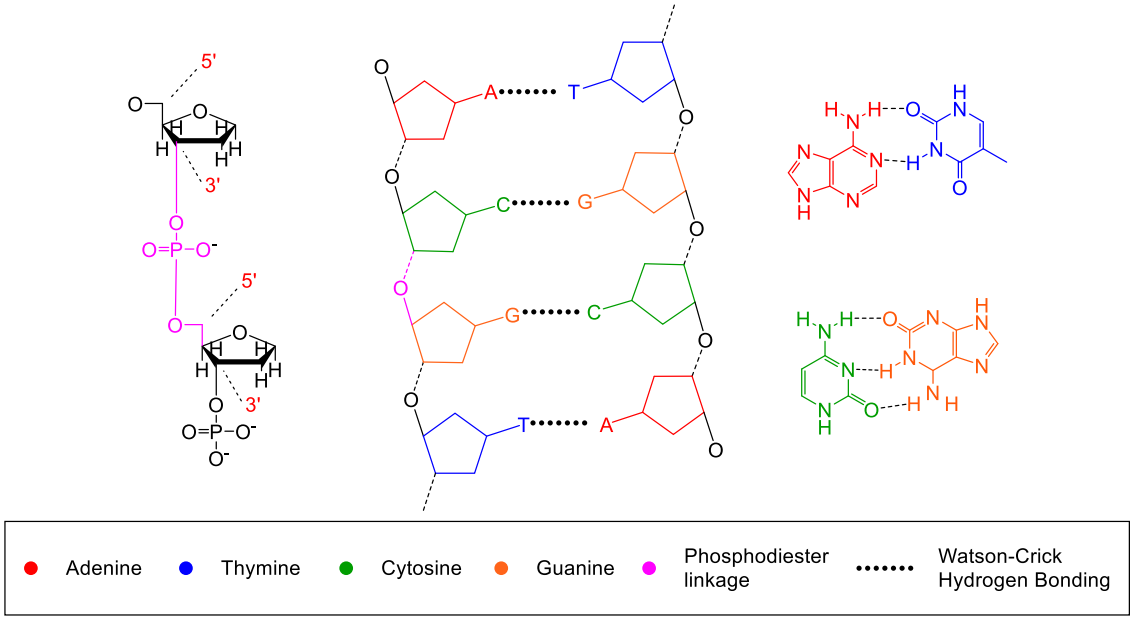

Figure 4.1: General Structural features of DNA.

molecule, one could tailor the molecule to exhibit the desired mode of binding. However, when incorporating these alterations, the overall solubility of the molecule should always be kept in mind. The molecule should ideally be soluble under physiological conditions. To this end an array of potential anticancer molecules needs to be studied to shed some light on any structure-activity relationship.[2]

4.3.1 Covalent Binding

Covalent bonding constitutes an important binding mode to transform DNA irreversibly, via alkylation or an inter-/intrastrand crosslink, therefore restricting proper cell growth. Since the discovery of cisplatin **1** by Rosenburg *et al.*[3] in the late 1960s, a paradigm shift in the design of anticancer drugs was observed. The square planar cisplatin complex binds covalently by forming interstrand crosslinks. Once liberated from its chloride ions, the platinum ion is known to form covalent interstrand crosslinks with N_7 atoms of consecutive guanine bases[4], which permanently alter the structure of DNA. Although cisplatin is effective, it reacts with all DNA non-selectively inducing severe side effects resulting in high cytotoxicity. In order to circumvent these disadvantages, the next generation platinum drugs, Carboplatin **2** and Oxaliplatin **3**,

exploited the use of less labile dicarboxylate leaving groups leading to improved stability as well as enhanced solubility. Some of the second generation platinum based drugs are shown in Figure 4.2.

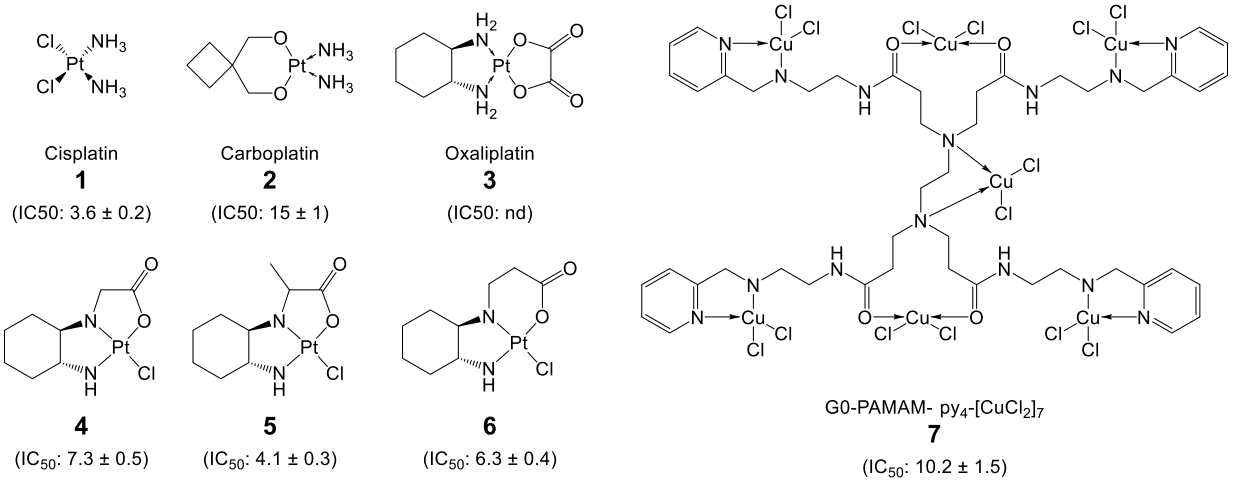

*Figure 4.2: Common covalent anticancer drugs (All IC_{50} values in μM): (**1**) cisplatin, (**2**) Carboplatin, (**3**) Oxaliplatin, (**4 - 6**) N,N,O-tridentate platinum complexes*[5] *and (**7**) G0-PAMAM– py_4–$[CuCl_2]_7$.*[6]

More recently a series of N,N,O-tridentate platinum complexes **4 - 6** (Figure 4.2) with both chloride and chelated carboxylate moieties as leaving groups was synthesized by Gou *et al.*[5] They evaluated these complexes against several human tumor cell lines such as A549 (non-small cell lung cancer), HCT-116 (colorectal cancer), MCF-7 (breast cancer) and HepG-2 (hepatocellular carcinoma). They found compound **5** (Figure 4.2) to be almost two-fold more active than Oxaliplatin against HCT-116 and its activity against MCF-7 was comparable to cisplatin.[5] From the literature, it is known that bulky adducts aids with distortion of the DNA backbone, which in turn affects transcription and replication of the DNA.[7,8] To this end, the use of dendrimers as ligands has been investigated. Copper complexes incorporated into dendrimers were evaluated against MOLT-4 (leukemia cells), MCF-7 (breast cancer cells) and Chang Liver cells by Chu *et al.*[6] Among other, the group studied G0-PAMAM– py_4–$[CuCl_2]_7$ **7** (Figure 4.2) which exhibited an IC_{50} value of 10.2 ± 1.5 μM against MCF-7.

4.3.2 Non-Covalent Binding

Molecules interacting non-covalently with DNA do so via reversible hydrophobic-, ionic-, hydrogen bonding, and/or Van der Waals interactions and cause conformational changes in the DNA, such as torsional tension for example. It interferes with protein-DNA interactions and can potentially lead to DNA strand breaks.[9] The use of metal complexes as anticancer agents has been under investigation with only a few examples in clinical trials and even less are in actual use. By incorporating metal centers into drug-like molecules the structural, reactivity and optical properties of the molecule change considerably. The inherent properties (geometry, redox state, etc.) of the metal atom influence the magnetic, thermodynamic and kinetic behavior of the molecule.[10] These physico-chemical changes can be monitored in order to deduce the manner in which the molecule interacts with DNA. Non-covalent interactions with DNA are categorized in three classes: intercalation, groove binding and electrostatic binding.

4.3.2.1 Intercalation

Molecules that interact with DNA via intercalation usually consist of planar heterocyclic moieties that can stack between adjacent DNA base pairs where the interactions are facilitated by π-π stacking. Intercalators interact with DNA independent of the nature of the DNA sequence and this occurs via van der Waals forces, hydrogen bonding, and/or hydrophobic affinity.[11] Two modes of intercalation are known viz. classical and threading intercalation.

An example of classical intercalators was studied by Uma *et al*.[12] They synthesized a copper (II) complex $[Cu(Itpy)_2](ClO_4)_2$ (Itpy = imidazole terpyridine) and determined the binding mode using calf thymus DNA (CT DNA). Analysis via spectroscopic titrations showed a decrease in intensity (hypochromism) of the intraligand transition at 336 nm upon addition of DNA, which is indicative of intercalation. If intercalation was the mode of binding, the DNA base pairs would have to separate in order to accommodate the ligand which would cause an overall increase in length of DNA which inevitably leads to an increase in viscosity of the DNA solution.[13] The viscosity measurements indicated a steady increase

in the relative viscosity of the solution. Thermal denaturing experiments determine the temperature at which half the DNA double helix denatures to single strands and is regarded as the melting temperature (T_m).[13] In the case of the copper complex monitored above an increase of $\Delta T_m = 5.0 \pm 0.5$ °C was observed which indicated that the imidazole terpyridine ligand stabilized the DNA double helix.

Sunita and co-workers[14] studied the DNA-binding properties of mixed Cu (II) 2,6-bis(benzimidazol-2-yl) pyridine complexes (**9**, **10**) via absorption spectroscopy, fluorescence spectroscopy, viscosity measurements and thermal denaturation methods. Spectroscopic titrations indicated the complexes bind to DNA through intercalation. Absorption spectra of the complexes in the presence of CT DNA are shown in (Figure 4.3a) and these indicate hypochromism as well as bathochromism of the metal to ligand charge transfer (MLCT) band upon addition of CT DNA. This is due to the strong π-π stacking interaction between the aromatic chromophore and the base pairs of DNA. Emission spectra, shown in (Figure 4.3b), indicate an increase in intensity upon addition of CT DNA, which indicates that the complexes bind to the hydrophobic pockets inside the DNA. Additionally, emission spectra of CT DNA pretreated with ethidium bromide (a proven intercalators[15]) show a decrease in intensity upon addition of the complexes as they compete with ethidium bromide for DNA binding (Figure 4.3c). Furthermore, thermal denaturing experiments indicated a 5 - 8 °C increase of T_m and viscosity measurements show a steady increase in relative viscosity as a result of increasing the concentration of **9** and **10**.

Threading intercalation is based on the same principle, but the molecules usually contain chains on opposite sides of the planar ring system which, once intercalated, allows the chains to interact with grooves in its close proximity. This mode of binding may hold several advantages concerning its biological activity, such as simultaneous blockade of both DNA grooves which may help effectively regulate gene expression, improved linker-DNA interactions, as well as lower dissociation rates from cellular DNA.[16] Shahabadi *et al.*[17] studied a copper complex (**11**) (Figure 4.4) containing 4,7-diphenyl-1,10-phenanthroline (DIP) as the

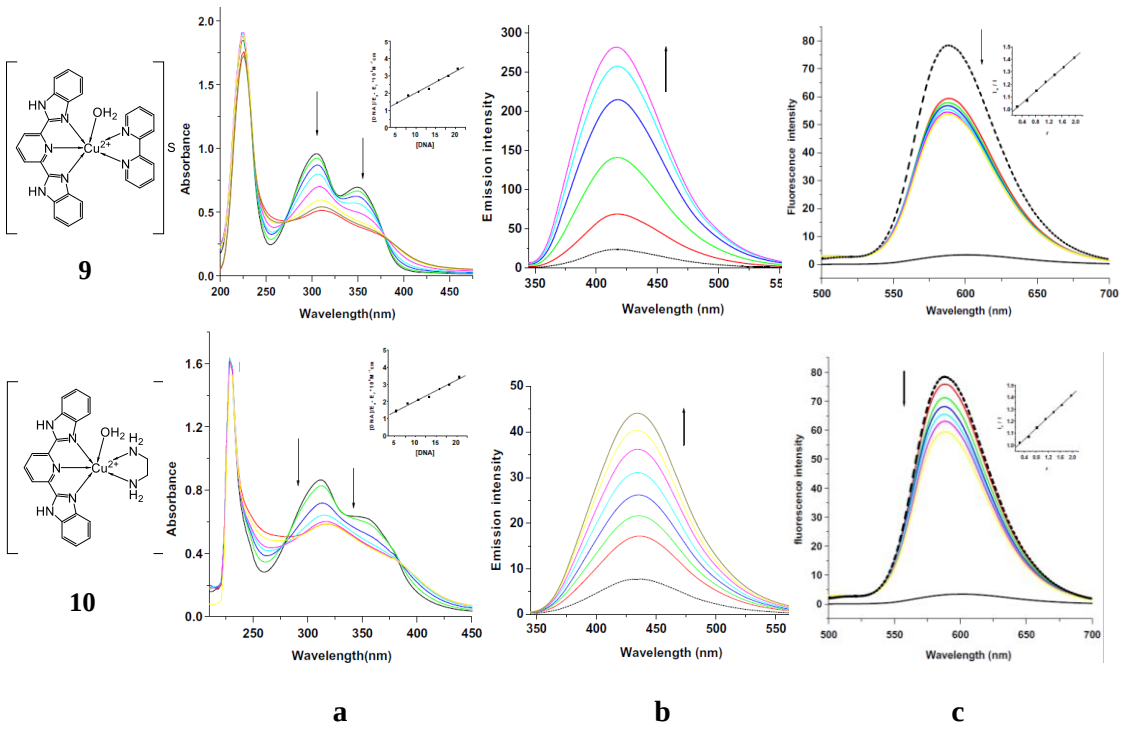

*Figure 4.3: Mixed Cu(II) 2,6-bis(benzimidazol-2-yl) pyridine complexes (**9**, **10**)[14] (a) UV-Vis spectroscopy titration experiments (b) Fluorescence spectroscopy titration experiments (c) Fluorescence spectroscopy competitive titration experiments.*

N,N-chelate in combination with (1E,6E)-1,7-Bis(4-hydroxy-3-methoxyphenyl)hepta-1,6-diene-3,5-dione (Curcumin). DIP was chosen to impart intercalation as a possible binding mode, whereas Curcumin is a known groove binder.[18] The intrinsic binding constant of **11** was found to be K_b = 2.50 ±0.2 × 10^5 M^{-1}, which was markedly higher than comparative Cu(Cur)(H_2O)Cl **12** (K_b = 5.21 × 10^4 M^{-1}) and [$Cu(Cur)_2$] **13** (K_b = 1.73 × 10^4 M^{-1}). The enhanced DNA binding is likely due to a synergistic effect of groove binding and intercalation.

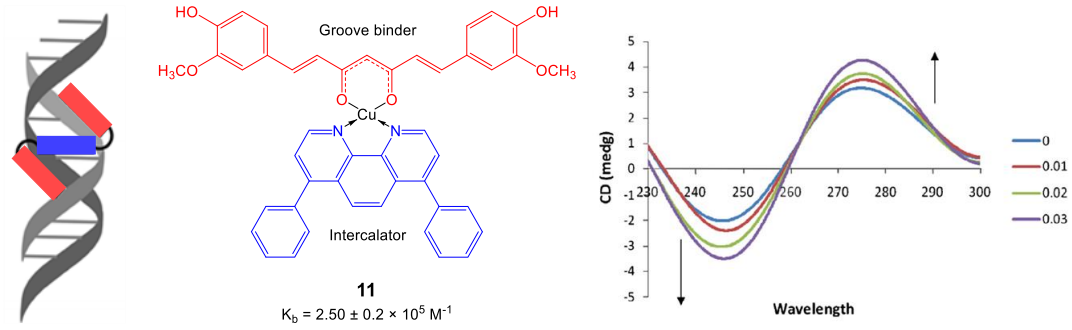

*Figure 4.4: Threading intercalation:[19] Circular dichroism of [Cu(Cur)(DIP)]Cl_2 (**11**) indicating intercalation as the predominant mode of binding.* [17]

4.3.2.2 Groove binding

In the previous example, Curcumin was identified as a groove binder. Typically groove binders are crescent shaped molecules with several aromatic rings connected by bonds with torsional freedom. The overall helical structure of DNA has sections where the strands are close to each other, known as minor grooves (AT rich sequences), and sections where they are further apart, known as major grooves (GC rich sequences). *Groove binding* relies on steric geometrical factors of the complete molecule to interact with these grooves via van der Waals and/or hydrogen bonding and mainly inhibit protein interaction or induce slight structural rearrangement of the DNA helix.[11]

Rajesh and co-workers[20] studied the interaction of **12** and **13** with CT DNA via UV–Visible, fluorescence, circular dichroism (CD), cyclic voltammetry and gel electrophoresis methods. CD is a technique that investigates how the structure of DNA changes upon interaction with a compound. DNA in its most common B-form display 2 bands in CD, a positive band (around 275 nm) and a negative band (around 248 nm) due to the base stacking and the polynucleotide helicity, respectively.

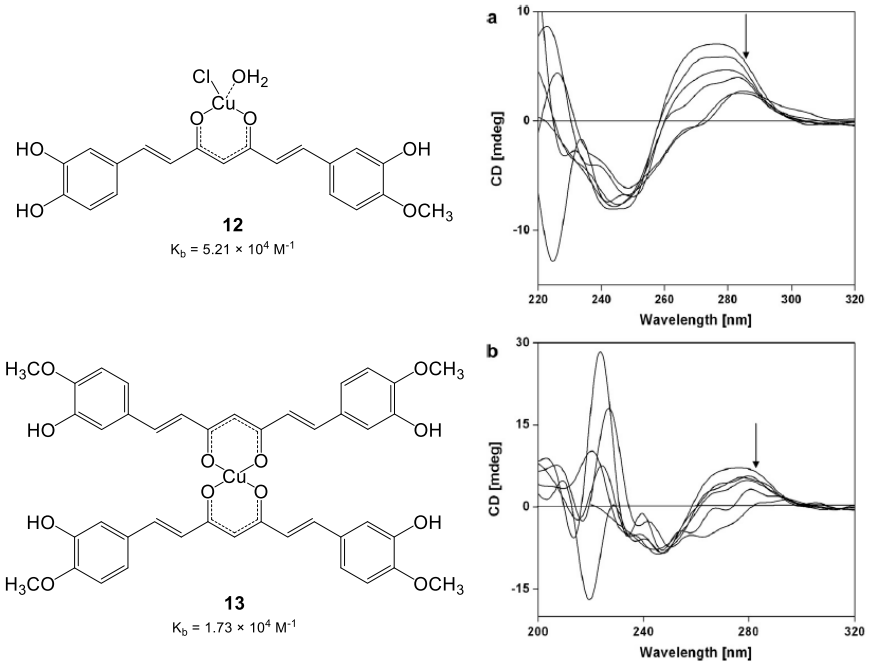

*Figure 4.5: Circular Dichroism: Cu(Cur)(H_2O)Cl (**12**) and [Cu(Cur)$_2$] (**13**).* [20]

Their circular dichroism studies (Figure 4.5) showed strong perturbation of both the positive (base stacking) and negative (polynucleotide helicity) CD bands. The general decrease in the positive band and the new band forming in the negative band indicate the DNA is unwound upon addition of the complexes which destabilize the B-form DNA via groove binding.[20] Rajesh *et al.*[21] then synthesized macrocyclic tetraaza diacetyl curcumin Cu(II) complex (**14**) which also interacts with DNA via groove binding with a comparable binding constant, $K_b = 1.4 \times 10^5\ M^{-1}$.

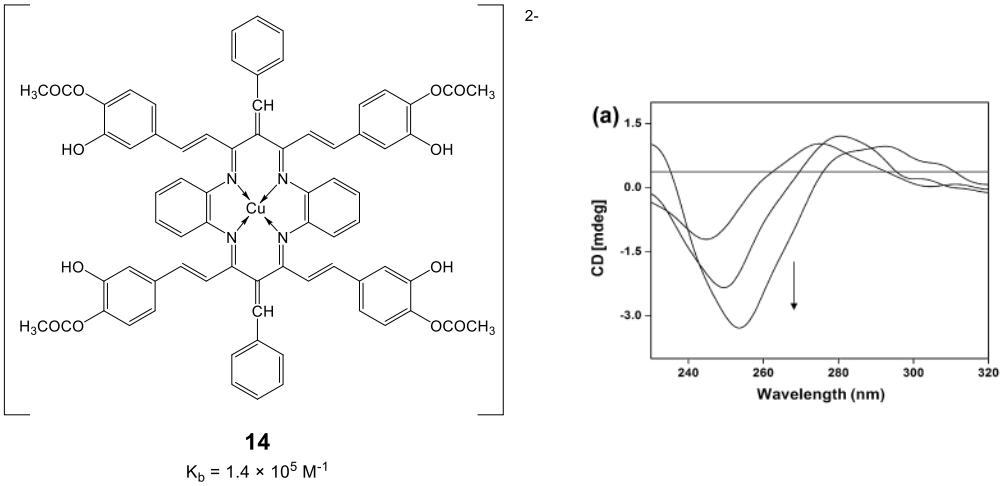

*Figure 4.6: Macrocyclic tetraaza diacetyl curcumin Cu(II) complex (**14**).* [21]

4.3.2.3 Electrostatic binding

Electrostatic binding is common for charged molecules. Some ligands form large aggregates (to reduce repulsion between ligands) with the anionic phosphonate backbone held in place by non-specific, outside edge stacking interactions. Arjmand *et al.*[8] studied the DNA interaction of three novel dizinc (II) complexes and during UV-Vis absorption titrations observed a hyperchromic shift of the intraligand absorption band and a slight blue shift upon addition of CT DNA. The hyperchromism occurred as a result of DNA structural damage which they attribute to electrostatic interaction between their complexes and DNA. They suspected partial intercalation as a possible contributor to the electrostatic interaction observed.

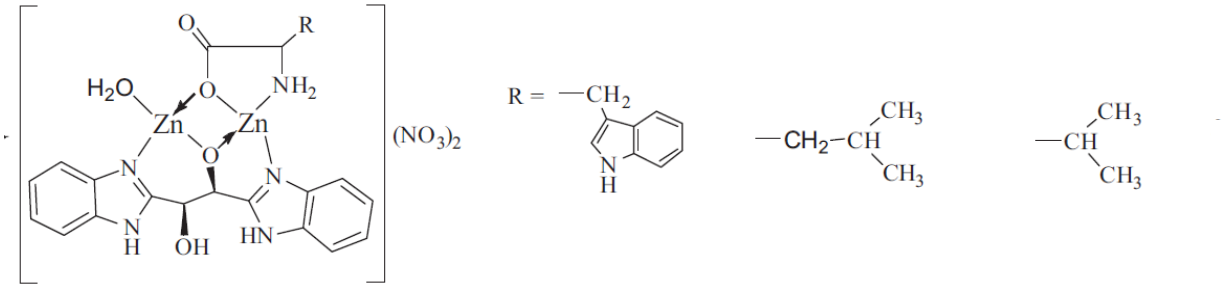

Figure 4.7: Dizinc(II) complexes 1–3, derived from 1,2-bis(1H-benzimidazol-2-yl)ethane-1,2-diol [8]

4.4 Results and Discussion

4.4.1 DNA binding studies

Various analytical techniques are used to study drug-DNA interactions. These interactions can be monitored via Infra-red (IR), Raman, Circular dichromism (CD), UV-Vis, fluorescence and nuclear magnetic resonance (NMR) spectroscopies as well as through Atomic force microscopy (AFM), electrophoresis, mass spectrometry, viscosity measurements, thermal denaturation studies, and cyclic, square wave and differential voltammetry. Several review articles are available to enhance the understanding of the application of these methods for drug-DNA binding studies.[11,20,22,23] However, only UV-Vis spectroscopy will be discussed further with regards to the preliminary DNA binding studies reported on in this chapter.

Electronic absorption spectroscopy is a common technique used to study drug-DNA interactions. UV-Vis titration experiments are commonly performed for preliminary confirmation of drug-DNA interaction. By simply monitoring the change in absorbance upon addition of either DNA or compound, a correlation can be made to the type of interaction occurring. A hyperchromic shift indicates a conformational change in the DNA that leads to destabilization of the secondary structure, whereas any stabilization causes a hypochromic shift. Essentially, the shift in the position of an absorbance maximum is monitored and a comparison is made between the absorbance of free compound and that of the compound-DNA complex.

Compounds that interact via intercalation generally lead to a reduction in absorbance (hypochromism) accompanied by a shift to higher wavelength (bathochromism/ red shift).[24] The π* orbitals of the aromatic chromophore can overlap with the π orbitals of DNA base pairs stabilizing the π-π* stacking interactions thus lowering the π-π* transition energies.[25] Electrostatic interaction, usually between a charged compound and the phosphorous backbone, leads to hyperchromism. Groove binders can induce both hypo- and hyperchromism based on the effect that it exerts on the DNA structure.

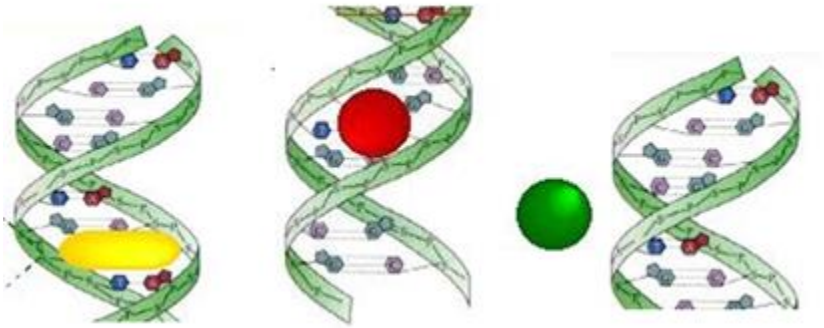

Figure 4.8: Non-covalent DNA binding modes. From left to right; intercalation, groove binding and electrostatic binding. [26]

4.4.1.1 Electronic absorption titration

As previously mentioned, a common method to study the DNA binding is to monitor the absorbance during UV-Vis titrations. Ideally a wavelength where only the DNA or only the complex absorbs, should be monitored.[27,28] However, in the current study the absorption bands of the compounds under investigation overlapped with those of DNA. Thus, an alternative method was employed where DNA was added to both the reference and the sample cuvettes. This method allows the direct correlation of any change in the compound spectrum to the interaction between the compound and DNA.[29]

The DNA binding capability of **D2**, **C1**, **MC1, L3**, **C4a**, **C4b** and **C5** was evaluated through UV-Vis absorption titrations. During the UV-Vis titrations the compound concentration was kept constant while varying the DNA concentration in solution. The change in absorbance correlates to drug-DNA interaction and can be employed to elucidate information about binding behaviour. The synthesis and characterization

of these compounds were discussed in Chapter 3, section 3.2. The compounds evaluated can be divided into phosphonic acid complexes (**MC1** and **C1**) and salicylaldimine complexes (**L3**, **C4**, **C5**). The data presented in this chapter provides some insight with regards to the effect of the ligand (**C1** vs **C4**) and the metal (**C4** vs **C5**) on the compounds binding interaction with DNA.

The preliminary UV-Vis titration studies for the phosphonic acid complexes (**MC1** and **C1**) were hampered by the solubility of the compounds. The spectra recorded in DMSO showed negative absorption. It was thought that DMSO coordinates to the compound in solution, leading to a negative absorbance. Thus, a small test was performed where the compounds were dissolved in H_2O before adding DMSO (5 × 10 µL) portions and allowing 10-minute incubation periods at 25 °C before collecting the corresponding UV-Vis spectra. All these absorptions remained unaltered after the DMSO interaction test which suggests solvent interaction was not the cause of the negative absorbance observed.

The preliminary UV-Vis titrations (**MC1** and **C1**) conducted in H_2O showed a single absorption band in the range of 200 – 260 nm. These absorption bands can be attributed to amide n-π* transition. The experiment was inconclusive as the absorbance intensity varied randomly as the concentration of the DNA was added. In the case of **MC1**, an absorbance at 620 nm indicated that there were some particles in suspension. The lack of solubility and hygroscopic nature of **MC1** and **C1** prohibit the accurate determination of the weight, which influence the concentration of stock solutions. Thus, the phosphonic acid complexes could not be studied by UV-Vis spectroscopy.

The UV-Vis binding studies of **D2** in H_2O displayed an absorbance at 294 nm which can most likely be attributed to the π-π* transition of the amide moiety. The band displays a slight hyperchromic shift upon addition of DNA and the formation of a new absorption band at 222 nm is also observed. Although this indicates some interaction, most likely via groove interaction, it is not significant when compared to the **L3** or **C4a**, **C4b** and **C5**. This is expected, otherwise it would not be worth modifying the dendrimers.

The UV-Vis binding studies (Figure 4.9) for **L3** showed 4 absorption bands. The π-π* transition for **L3** are observed at 212 and 255 nm. These differ from **D2** and can be ascribed to the aromatic chromophore present in **L3**. Additionally, the imine n- π* transition is observed at 325 nm and the band in the region of 350 – 400 nm are likely due to some intra ligand transition.

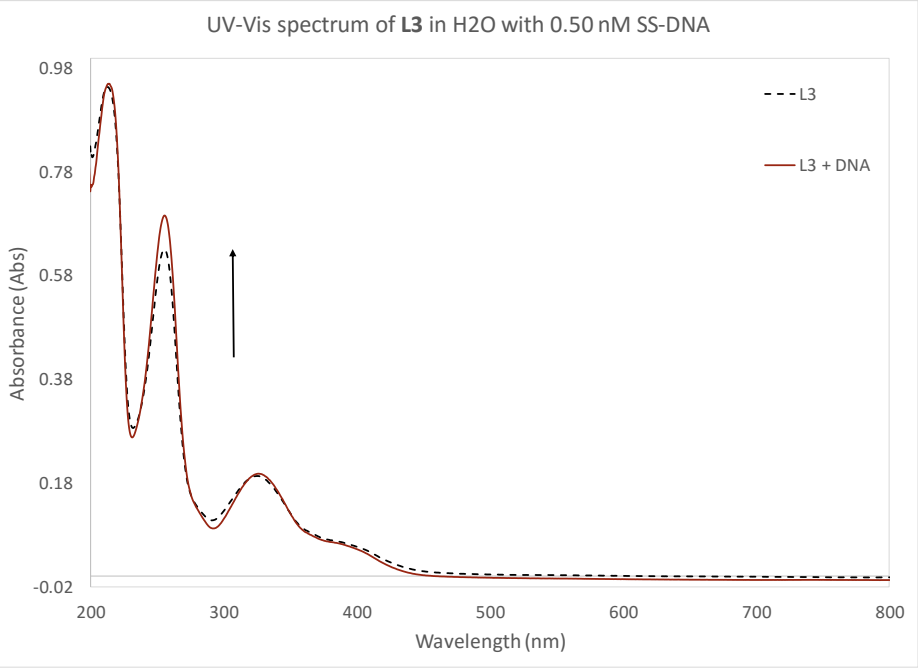

*Figure 4.9: UV-Vis titrations of **L3** interacting with increasing concentration SS-DNA.*

The UV-Vis spectra of **L3** show a hyperchromic effect of 9 % upon addition of DNA for λ_{max} = 255 nm. The ligand (**L3**), without any metal, is expected to interact with DNA. However, the hyperchromic shift observed for **L3** contradicts the expected hypochromism commonly observed for Schiff-base ligands. The UV-Vis spectra of **C4b** (Figure 4.10) showed 5 absorption bands. The results are similar to that observed for **L3**, yet the hyperchromic effect was more pronounced with λ_{max} = 255 nm showing hyperchromism of 28 %. These compounds most likely interact with DNA in an electrostatic or groove binding mode. Although, given the nature of these compounds, they are more likely to interact through groove binding that damage the DNA double helix, hence the hyperchromism.

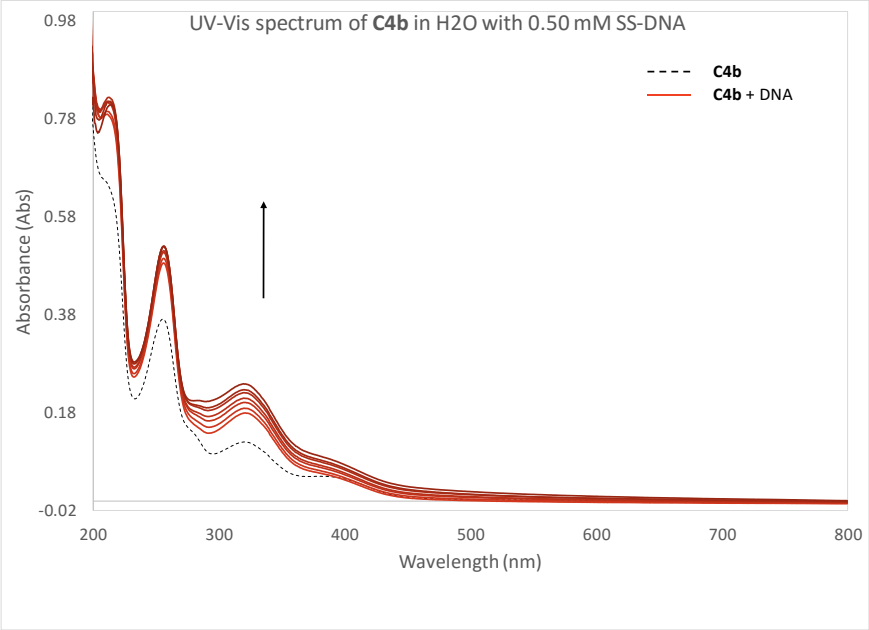

*Figure 4.10: UV-Vis titrations of **C4b** interacting with increasing concentration SS-DNA.*

On the contrary, **C5** displays the expected hypochromic shift for all its corresponding absorptions, where Λ_{max} = 267 nm show 24 % hypochromism, and is likely due to the π-π* stacking interaction between the aromatic chromophore present in the ligand and the DNA base pairs.

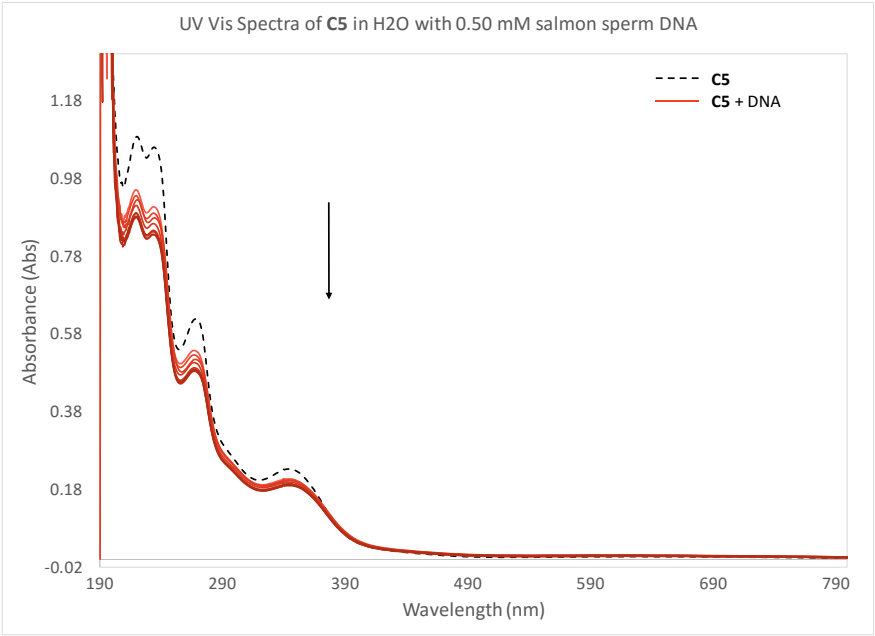

*Figure 4.11: UV-Vis titrations of **C5** interacting with increasing concentration SS-DNA.*

Comparing **C4a** (Ga) and **C5** (Cu), which is based on the same ligand, it is clear how crucial the metal centre is for the activity of the compound under investigation. By altering the metal the mode of binding is completely different.

The preliminary DNA binding studies for **C4a** are presented in Figure 4.12 and 4.13. Figure 4.12 displays the spectra obtained when adding increments of DNA to the compound solution, whereas Figure 4.13 displays the spectra obtained for constant compound and DNA concentration monitored hourly for 24 hours. The UV-Vis titrations studies for **C4a** showed 5 absorption bands. The absorption bands corresponding to the aromatic π-π* transition show a constant hypochromic shift. The shoulder at 280 nm disappeared and was accompanied by the formation of a new absorption band at 300 nm, which for the duration of the experiment displayed a hyperchromic shift. The imine n-π* transition as well as the band ranging from 380 – 400 nm initially indicated a hyperchromic shift before decreasing in absorption for the rest of the experiment. These observations, varying hyperchromism and hypochromism, preliminarily indicate the possibility that multiple modes of binding are present when **C4a** interacts with DNA.

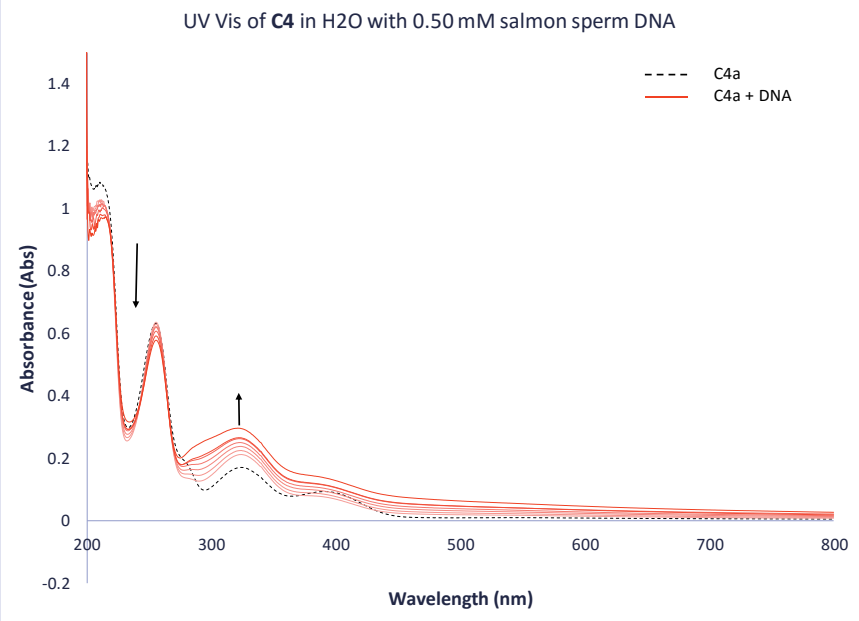

*Figure 4.12: UV-Vis titrations of **C4a** interacting with increasing concentration SS-DNA.*

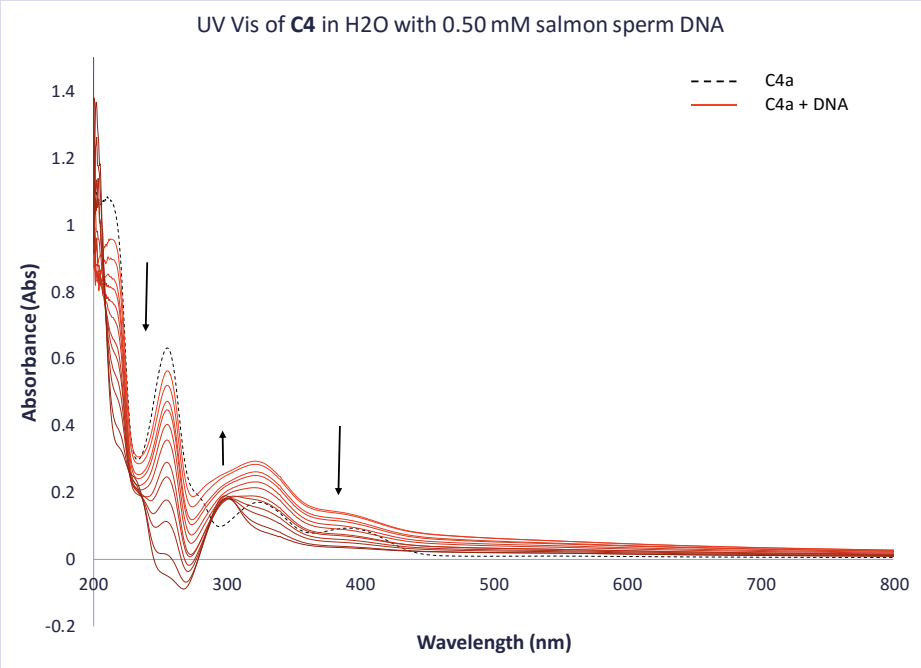

*Figure 4.13: UV-Vis titrations of **C4a** interacting with increasing concentration SS-DNA.*

The shoulders appearing in the range of 280 – 300 nm can be due to the single strand of DNA liberated from the double helix-DNA strands. In other words, as the compound interacts with the DNA, double helix is divided to single strands which only increase in the vial containing the compound, thus only appearing after a while when the concentration is detectable.

The manner in which the ligand binds to the metal center is also important. **C4a** and **C4b** consist of the same ligand (**L3**) and the same metal center (Ga), but differs only in the precursor used to obtain the respective complexes. There was clearly a different mode of binding at play with these metals and, although further studies have to be conducted to determine exactly what occurs, the metal surrounded by 2 dendritic branches most likely interact via groove binding and the metal surrounded by a single dendritic branch interacts via multiple modes of binding.

4.5 Conclusion

In this chapter, the preliminary UV-Vis binding studies of the cyclam-cored PAMAM dendrimer (**D2**), phosphonic acid derivatives (**MC1** and **C1**), salicylaldimine ligand (**L3**) and complexes (**C4a**, **C4b** and **C5**)

was reported. **D2** showed a slight hyperchromic shift that suggests the dendritic scaffold interacts via groove binding. The phosphonic derivatives were hampered by lack of solubility and could not be assessed by UV-Vis binding studies. Surprisingly **L3** and **C4b** showed hyperchromism with the latter being more apparent, which indicates either electrostatic or groove binding interaction is at play. The nature of these compounds is more likely to interact through groove binding that can damage the DNA double helix. **C5** shows a hypochromic effect and is likely due to the π-π* stacking interaction between the aromatic chromophore present in the ligand and the DNA base pairs. **C4a** showed varying hyperchromism and hypochromism which suggests that it interacts with DNA via multiple binding modes.

4.6 Experimental Section

A Tris-HCl buffer solution (pH 7.2) was prepared following a standard protocol. 200 µM stock solutions of each compound were prepared in H_2O by stirring overnight. The stock solutions were diluted to 20 µM sample solution using Tris-HCl buffer solution (pH = 7.25). The corresponding reference sample (10 % H_2O/Tris-HCl buffer) was prepared. The 160 µL DNA (1mg/ml) sample was dissolved in 9.9 ml Tris-HCl buffer at pH = 7.25. The concentration of SS-DNA was determined via UV-Vis spectrometry at A_{258} and was found to be 0.50 mM. The molar absorptivity value was taken as 6600 M^{-1} cm^{-1}. A solution of the DNA in Tris-HCl buffer gave a ratio of UV-absorbance at 260 and 280 nm (A_{260}/A_{280}) of 1.8, indicating the DNA was sufficiently free of protein. All the stock solutions were stored at > 4 °C and used within four days.

The UV-Vis titration spectra were recorded from 190 nm to 800 nm with fixed compound concentration while varying the SS-DNA concentration. Aliquots (5 – 20 µL) of salmon sperm DNA (0.46 – 0.50 mM) were added to both the sample cell and the reference cell in order to eliminate the absorbance of SS-DNA itself. The samples were manually stirred before allowing 5-minute incubation time at 25 °C between each addition of DNA. At incubation temperature 37 °C, the DNA denatures. The process was repeated until the same spectrum was obtained for three additions of DNA, indicating that DNA saturation was achieved.

4.7 References

(1) Cox, M. M.; Doudna, J. A.; O'Donnell, M. In *Molecular Biology. Principles and Practice*; 2012; pp 175–214.

(2) Sheng, J.; Gan, J.; Huang, Z. *Med Res Rev.* **2013**, *33* (5), 1119–1173.

(3) Rosenberg, B.; Vancamp, L.; Krigas, T. *Nature* **1965**, *205*, 698–699.

(4) Wing, R. M.; Pjura, P.; Drew, H. R.; Dickerson, R. E. *EMBO J.* **1984**, *3* (5), 1201–1206.

(5) Zhao, J.; Gou, S.; Liu, F.; Sun, Y.; Gao, C. *Inorg. Chem.* **2013**, 52 (14), 8163–8170.

(6) Zhao, X.; Loo, S. C. J.; Lee, P. P. F.; Tan, T. T. Y.; Chu, C. K. *J. Inorg. Biochem.* **2010**, *104* (2), 105–110.

(7) Gomez-Pinto, I.; Cubero, E.; Kalko, S. G.; Monaco, V.; van der Marel, G.; van Boom, Jacques H. Orozco, M.; Gonzalez, C. *J. Biol. Chem.* **2004**, *279* (23), 24552–24560.

(8) Parveen, S.; Arjmand, F. *Spectrochim. Acta Part A Mol. Biomol. Spectrosc.* **2012**, *85* (1), 53–60.

(9) Rehman, S. U.; Sarwar, T.; Husain, M. A.; Ishqi, H. M. *Arch. Biochem. Biophys.* **2015**, *576*, 49–60.

(10) Bruijnincx, P. C.; Sadler, P. J. *Curr. Opin. Chem. Biol.* **2008**, *12* (2), 197–206.

(11) Sirajuddin, M.; Ali, S.; Badshah, A. *J. Photochem. Photobiol. B Biol.* **2013**, *124*, 1–19.

(12) Uma, V.; Kanthimathi, M.; Weyhermuller, T.; Nair, B. U. **2005**, *99*, 2299–2307.

(13) Rehman, S. U.; Sarwar, T.; Husain, M. A.; Ishqi, H. M.; Tabish, M. *Arch. Biochem. Biophys.* **2015**, *576*, 49–60.

(14) Sunita, M.; Anupama, B.; Ushaiah, B.; Kumari, C. G. *Arab. J. Chem.* **2015**, 10 (2), 3367-3374.

(15) Kelly, J. M.; Tossi, A. B.; Mcconnell, D. J.; Ohuigin, C. *Nucleic Acid Res.* **1985**, *13* (17), 6017–6034.

(16) Lamberson, C. Topologically constrained DNA intercalators: synthesis and DNA binding studies., PhD Thesis University of Illinois, 1991.

(17) Shahabadi, N.; Falsafi, M.; Moghadam, N. H. *J. Photochem. Photobiol. B Biol.* **2013**, *122*, 45–51.

(18) Zsila, F.; Bikádi, Z.; Simonyi, M. *Org. Biomol. Chem* **2004**, *2*, 2902–2910.

(19) Rescifina, A.; Resci, A.; Zagni, C.; Varrica, M. G.; Pistarà, V.; Corsaro, A. *Eur. J. Med. Chem.* **2014**, *74*, 95–115.

(20) Rajesh, J.; Rajasekaran, M.; Rajagopal, G. *Spectrochim. Acta Part A Mol. Biomol. Spectrosc.* **2012**, *97*, 223–230.

(21) Rajesh, J.; Gubendran, A.; Rajagopal, G. *J. Mol. Struct.* **2012**, *1010*, 169–178.

(22) Yang, Y.; Sass, L. E.; Du, C.; Hsieh, P.; Erie, D. A. *Nucleic Acids Res.* **2005**, *33* (13), 4322–4334.

(23) González-Ruiz, V.; Olives, A. I.; Martín, M. A.; Ribelles, P.; Menéndez, M. T. R. and J. C. In *Biomedical Engineering, Trends, Research and Technologies*; InTech, 2011; pp 65–90.

(24) Rambabu, A.; Kumar, M. P.; Tejaswi, S.; Vamsikrishna, N. *J. Photochem. Photobiol. , B Biol.* **2016**, *165*, 147–156.

(25) Liu, Z.; Wang, B.; Li, B.; Wang, Q.; Yang, Z.; Li, T.; Li, Y. *Eur. J. Med. Chem.* **2010**, *45*, 5353–5361.

(26) Sirajuddin, M.; Ali, S.; Badshah, A. *J. Photochem. Photobiol. B Biol.* **2013**, *124*, 1–19.

(27) Cheng-Yong, Z.; Xiao-Li, X.; Pin, Y. *Biochem. (Moscow, Russ. Fed.)* **2007**, *72*, 37–43.

(28) Tarushi, A.; Christofis, P.; Psomas, G. *Polyhedron* **2007**, *26*, 3963–3972.

(29) Oge, N.; Aslanoglu, M. *Turkish J. Chem.* **2005**, *29*, 477–485.

CONCLUSIONS AND FUTURE WORK

The aim of this research project was to develop novel targeted dendritic radiopharmaceuticals which could potentially be applied in targeted radiotherapy. Careful consideration of the dendrimer scaffold, chelating ligand as well as the radionuclide was taken.

The first objective was to synthesize novel cyclam-cored PAMAM dendrimers of various generations. The cyclic core was chosen to incorporate specific physical properties to the dendrimer scaffold. The divergent synthesis of these dendrimers was discussed in Chapter 2. We successfully synthesized G1 cyclam-cored PAMAM dendrimer (**D1** - **D2**), but could unfortunately not succeed in isolating the G2 derivative (**D3** - **D4**) due to several complications during the amidation reaction. Therefore, alternative TACN-cored PAMAM dendrimers (**D5** - **D6**) was attempted via a similar method, but the difficulties in the amidation reaction persisted. We found that during the amidation reaction several side reactions yielded a mixture of products that remained inseparable due to the similarities of their chemical properties. In a last attempt to obtain higher generation cyclam-cored dendrimers, we attempted to alter the branches. Cyclam dendrimers with propyl branches (**D7** - **D8**) and cyclam dendrimers with benzyl branches (**D9** - **D10**) was attempted in order to circumvent the amidation step. Unfortunately, we could not succeed in reducing the nitrile moieties completely to only their primary amine derivatives.

At that point **D2** was identified as a viable dendritic scaffold for two ranges of dendritic ligands. Initially, a phosphonic acid (**L1**) derivative was synthesized via an Irani-Moedritzer. As a comparison to **L1**, a range of phosphonic acid model ligands were also synthesized (**L2**, **ML1**, **ML2**). We found that during the synthesis of the phosphonic acid derivatives the amide moiety of the PAMAM dendrimer was susceptible to hydrolysis, which contributed to a mixture of products that was near impossible to separate. The nature of the crude products, especially in the case of **L1**, hindered the seemingly unreproducible reaction further. Alternatively, a salicylaldimine (**L3**) derivative was obtained via a Schiff base condensation reaction. The dendritic ligand synthesis was discussed in Chapter 3, which also covered the

complexation reactions with either gallium or copper to obtain "cold" dendritic radiopharmaceutical analogues. **C1** and **MC1** was obtained through complexation of gallium with **L1** and **ML1**, respectively. **L3** was modified with gallium (**C4a** and **C4b**) as well as copper (**C5**) to obtain their respective complexes. Where possible, all ligands and complexes were characterized by FTIR and NMR spectroscopy, elemental analysis, mass spectrometry and UV/Vis spectroscopy.

Finally, the DNA binding studies of some of the dendritic complexes were preliminarily investigated via UV Vis spectroscopy titration reactions. The phosphonic acid derivatives were only partially soluble in the buffer solution and could therefore not be assessed via this technique. The salicylaldimine ligand (**L3**) as well as the gallium (**C4a**, **C4b**) and copper (**C5**) derivatives were viable candidates. The results indicated that all four compounds interacted with salmon sperm DNA. **L3** and **C4b** showed hyperchromism which indicates either electrostatic or groove binding interaction is at play, but given the nature of these compounds, groove binding is more likely. **C5** shows a hypochromic effect, which translates to intercalation as the mode of binding to DNA. **C4a** showed varying hyperchromism and hypochromism which suggests that it interacts with DNA via multiple binding modes. Further investigation of these compounds is necessary to draw a concrete conclusion as to their preferred mode of binding with DNA.

To conclude, the benefit that the cyclic core would add to the topology of the dendrimer is not significant below generation 2 dendrimers and obtaining generation 2 and higher dendrimers of adequate purity was simply not feasible. Thus, if dendrimers were to be chosen as the nanocarrier vector, commercially available dendrimers would certainly be the way to go. Alternatively, the dendrimers could be synthesized via a convergent approach where the dendrons would be synthesized and isolated before linking them to a core Figure 5.1. This would enhance the purity of the dendrimers and grant the opportunity of obtaining higher generation dendrimers; however, this method is quite costly during synthesis.

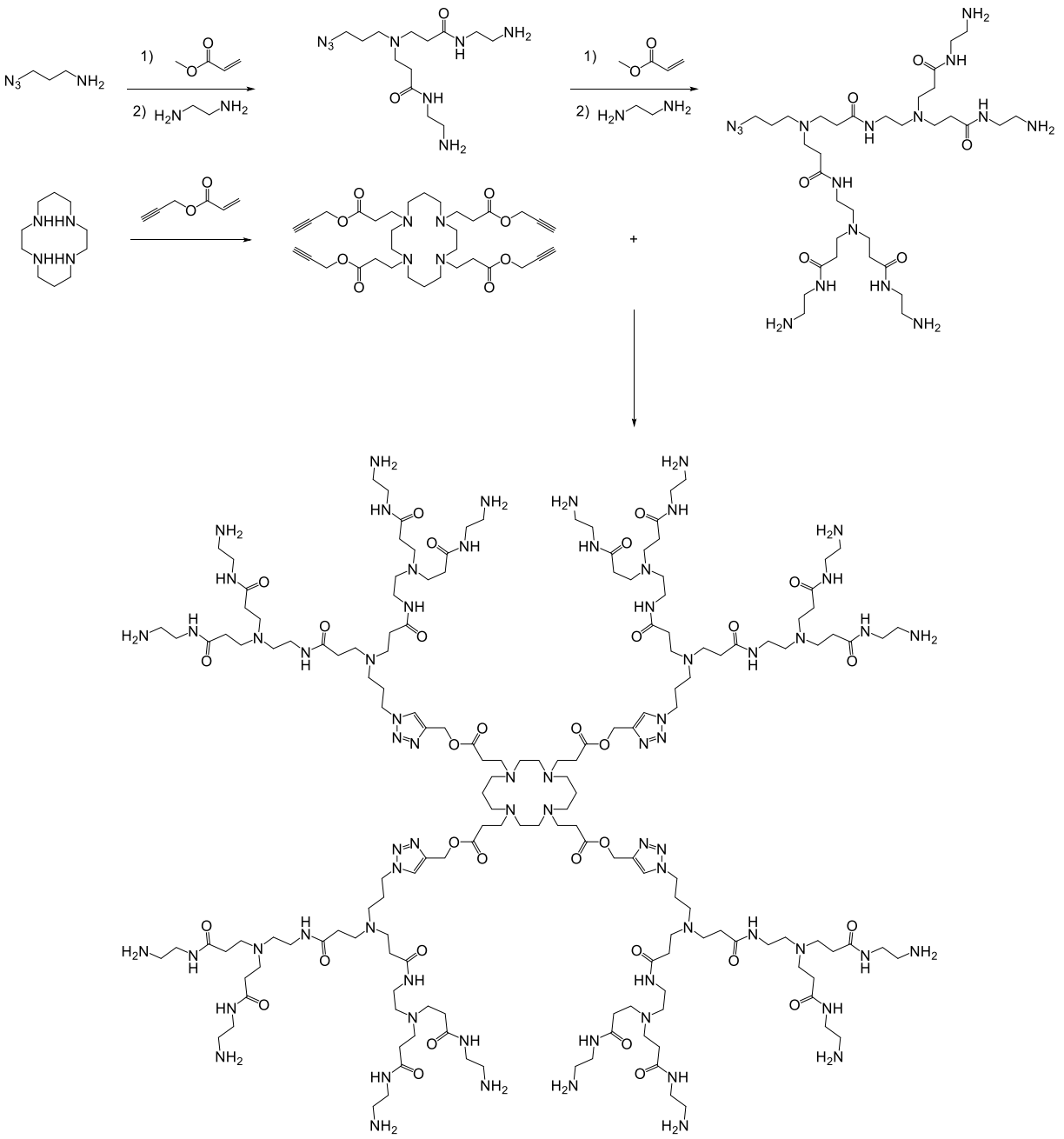

Figure 5.1: Suggested convergent approach – Dendron growth followed by click chemistry to incorporate cyclic core.

Following the Irani-Moedritzer procedure it was possible to synthesize the corresponding ligands; however, the purification and isolation of these ligands were hampered by the lack of solubility and range of products in the reaction mixture. The best solution was to add the appropriate gallium salt and isolate the

complex. The major concern during this approach was the stringent reaction conditions which could lead to amide hydrolysis, contributing to the product mixture.

In the case of the Schiff base derivatives, it would be possible to perform the Schiff base condensation reaction directly with the mixture of products obtained from the full generation PAMAM dendrimers and isolating the corresponding salicylaldimine product. The aldehyde would only react with primary amines and the formed product should have significant different solubility than the byproducts. The Schiff base derivatives also offer the opportunity to incorporate a phosphonic acid moiety across the imine bond.

The phosphorylation of imine bonds to yield the corresponding α – aminophosphonates via a Pudovik reaction is a common methodology employed. The corresponding α – aminophosphophonic acid could be isolated after hydrolysis. Acid catalysed hydrolysis[1] requires high temperature, long reaction times and the use of strong hydracids (HCl, HBr, HI). Reagents that contain functional groups that are susceptible to hydrolysis limits the use of acids as catalysis. As an alternative base catalysed hydrolysis[2,3] could be employed, but generally leads to incomplete hydrolysis i.e. monoesters. The use of halogen-trimethylsilanes as hydrolysis agent provide a means to overcome the limitation.[3]

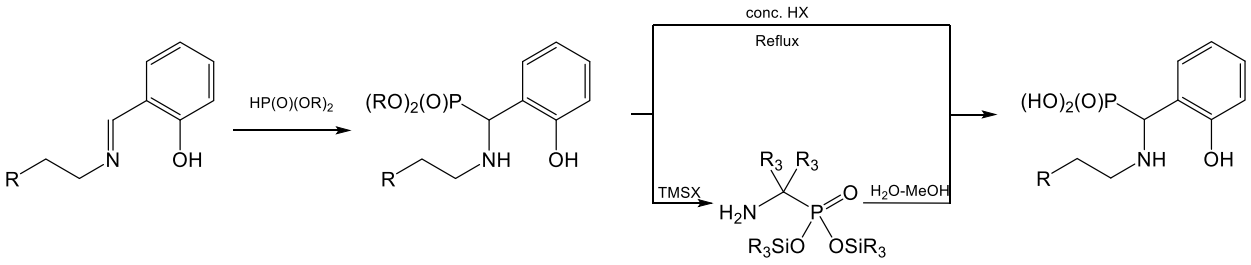

Figure 5.2: Acid- and Base catalysed hydrolysis of phosphonate esters.

Thus, in order to advance this research, meticulous planning of all synthetic aspects should be done. This would allow us to harness the advantages that dendrimers offer and exploit them as scaffolds for targeted radiopharmaceuticals.

References

(1) Rao, K. U. M.; Swapna, S.; Manidhar, D. M.; Reddy, K. M. K.; Reddy, C. S. *Phosphorus. Sulfur. Silicon Relat. Elem.* **2015**, *190* (2), 232–239.

(2) Lewkowski, J.; Tokarz, P.; Lis, T.; Slepokura, K. *Tetrahedron* **2014**, *70* (4), 810–816.

(3) Bou Orm, N.; Dkhissi, Y.; Daniele, S.; Djakovitch, L. *Tetrahedron* **2013**, *69* (1), 115–121.